



UNIVERSIDAD NACIONAL AUTÓNOMA DE MÉXICO
PROGRAMA EN ASTROFÍSICA
INSTITUTO DE ASTRONOMÍA

RAPID RESPONSE SPECTROPHOTOMETRIC
CHARACTERIZATION OF NEAR-EARTH OBJECTS

TESIS

PARA OPTAR POR EL GRADO DE:
DOCTOR EN CIENCIAS (ASTROFÍSICA)

PRESENTA

SAMUEL AMADEUS JOSSHUA RAMÓN NAVARRO MEZA

DIRECTORES DE TESIS

DR. MAURICIO REYES RUIZ, INSTITUTO DE ASTRONOMÍA,
SEDE ENSENADA, UNAM

DR. DAVID E. TRILLING, DEPARTMENT OF ASTRONOMY AND
PLANETARY SCIENCE, NAU

ENSENADA, BAJA CALIFORNIA, SEPTIEMBRE 2020



Universidad Nacional
Autónoma de México

Dirección General de Bibliotecas de la UNAM

Biblioteca Central



UNAM – Dirección General de Bibliotecas
Tesis Digitales
Restricciones de uso

DERECHOS RESERVADOS ©
PROHIBIDA SU REPRODUCCIÓN TOTAL O PARCIAL

Todo el material contenido en esta tesis esta protegido por la Ley Federal del Derecho de Autor (LFDA) de los Estados Unidos Mexicanos (México).

El uso de imágenes, fragmentos de videos, y demás material que sea objeto de protección de los derechos de autor, será exclusivamente para fines educativos e informativos y deberá citar la fuente donde la obtuvo mencionando el autor o autores. Cualquier uso distinto como el lucro, reproducción, edición o modificación, será perseguido y sancionado por el respectivo titular de los Derechos de Autor.

A todo aquel que se tomó el tiempo de enseñarme cualquier cosa

Índice

1. Resumen	3
2. Antecedentes	4
2.1. Asteroides	4
2.2. Objetos cercanos a la Tierra (NEOs)	5
2.3. Sondeos de NEOs	8
3. Introducción	10
3.1. Necesidad de técnicas no estándar	10
3.2. Estudio de 3 métodos diferentes para clasificar NEOs	12
4. Caracterización de NEOs utilizando fotometría de respuesta rápida con RATIR	14
5. Investigando la diversidad taxonómica en familias de asteroides utilizando ATLAS	27
6. Taxonomía de NEOs pequeños con RATIR -borrador-	36
7. Discusión	54
8. Conclusiones	58
Apéndice: Trabajos adicionales	59
A. Tránsitos de exoplanetas con múltiples filtros y observatorios	59
B. CMFA	68
C. El primer objeto interestelar observado y sus implicaciones en la formación planetaria	80
D. Observaciones del efecto YORP	85
E. Convocatoria CONACYT Ciencia de Frontera 2019	85
F. Divulgación	85

1. Resumen

Se presentan mediciones de 238 asteroides cercanos a la Tierra y 1612 asteroides del cinturón principal. El objetivo principal del trabajo es utilizar fotometría para obtener la distribución taxonómica de la muestra, particularmente distinguir entre objetos de tipo rocoso y no rocoso. Para analizar los datos se utilizan tres métodos computacionales diferentes, incluyendo una rutina de *Machine Learning*, y se discute la eficacia de cada uno de ellos. Los resultados encontrados coinciden con los generados por otros estudios utilizando espectroscopía. Esto representa una ventaja estratégica, pues muestra que es posible hacer estudios de clasificación de asteroides con telescopios de menor tamaño o con alta eficiencia con telescopios mayores. Los asteroides cercanos a la tierra fueron observados con el telescopio de 1.5 m del Observatorio Astronómico Nacional, San Pedro Martir. Los objetos del cinturón principal fueron extraídos del archivo de observaciones del proyecto *Asteroid Terrestrial-impact Last Alert System*, que observa con dos telescopios de 50 cm con una separación de aproximadamente 160 km entre ellos.

2. Antecedentes

2.1. Asteroides

Los asteroides son trazadores de las rutas dinámicas y evolutivas del sistema solar, por lo que el estudiarlos ayuda a entender cómo se formó y evolucionó, no sólo en estructura sino también en composición. Es claro que tener un mejor entendimiento de nuestro sistema planetario ayuda a estudiar otros. Esta idea se ha consolidado aún más con el reciente registro de dos objetos interestelares (IAU, 2017; Borisov, 2019).

Junto con los cometas, planetas enanos y satélites pequeños, los asteroides forman parte de los llamados 'cuerpos menores' del sistema solar y se encuentran en diferentes regiones del mismo: el entorno terrestre, las inmediaciones de la órbita de Marte, la órbita de Júpiter, el cinturón principal de asteroides, la región transneptuniana, la Nube de Oort, etc. Los planetas tienen abundantes procesos internos (e.g. geológicos y atmosféricos), sin embargo, sus órbitas son estables y su estado general es mayormente constante. Por otro lado, los cuerpos menores tienden a tener un comportamiento opuesto. Estos pueden perder material (e.g. Hartmann et al., 1987), cambiar su órbita debido a la radiación solar (Opik, 1951; Vokrouhlický et al., 2015) o a la influencia de los planetas (Wetherill, 1976; Bottke et al., 2002), modificar sus superficies (e.g. Miyamoto et al., 2007), colisionar y fragmentarse (Housen, Holsapple, 1990), etc. Las colisiones tienen un papel importante en la evolución de estos cuerpos, por ejemplo formando 'familias', las cuales en ocasiones son producto de un asteroide de mayor tamaño que ha sido fragmentado. Por lo tanto, dada la taxonomía de un asteroide, se espera que la familia generada a partir de este tenga una taxonomía mayormente homogénea y similar a la del cuerpo original, sin embargo es difícil distinguir entre los miembros de la familia y objetos en el cielo de fondo (Mothé-Diniz et al., 2005). Una de las herramientas útiles para hacer esta distinción, o distinguir entre diferentes familias son los colores astronómicos, sean estos definidos como la resta de la magnitud en dos bandas fotométricas diferentes, u otra combinación lineal de ellas

(Parker et al., 2008).

Uno de los parámetros más característicos de los asteroides es su 'magnitud absoluta', comunmente denotada como H o en ocasiones H_V . Esta es la magnitud aparente que un observador mediría si el objeto estuviera a 1 unidad astronómica del observador, a 1 unidad astronómica del Sol, y que a su vez el objeto estuviera completamente iluminado. Esta cantidad es solo una referencia, pues se basa en una configuración imposible, ya que las dos primeras condiciones requieren una geometría triangular, mientras que la tercera requiere que la Tierra esté entre el Sol y el objeto (Glo, 2020).

2.2. Objetos cercanos a la Tierra (NEOs)

Los objetos cercanos a la Tierra (NEOs por sus siglas en inglés), son aquellos que su órbita los mantiene cerca de nuestro planeta y comprenden una amplia cantidad de parámetros físicos y orbitales (Mommert et al., 2015). Técnicamente son aquellos objetos con perihelio q menor a 1.3 Unidades Astronómicas (UA), e incluyen tanto asteroides (Near Earth Asteroids, NEAs) como cometas (Near Earth Comets, NECs), siendo los primeros los más abundantes. Por sus características orbitales, los NEOs se dividen principalmente en tres categorías: Amors con semieje mayor, $a > 1$ UA y $1.017 < q < 1.3$ AU; Apollos con $a > 1$ y $q < 1.017$; Atenas con $a < 1$ UA y afelio $Q > 0.983$ AU. Un NEA tiene una escala de vida promedio de 10^7 años (Morbidelli, Gladman, 1998), la cuál es corta en comparación con la edad del sistema solar. Por lo tanto, la existencia actual de estos objetos implica que hay fuentes para su reabastecimiento. Estudios por medio simulaciones numéricas complementadas con datos observacionales, han demostrado que el cinturón principal de asteroides es la mayor de estas fuentes (Bottke et al., 2002; Granvik et al., 2018). En esa región, la interacción gravitacional por medio de resonancias entre los planetas gigantes provoca que los asteroides alteren su órbita y sean traídos al entorno terrestre, donde pasan la última etapa de su vida, antes de ser engullidos por el Sol.

Los primeros estudios de NEOs fueron hechos con fotometría (Groeneveld, Kuiper, 1954), en ellos se definieron dos grupos taxonómicos principales, los asteroides de tipo 'C' que presentan alto contenido orgánico y los de tipo 'S' que presentan un alto contenido de silicatos (similar a una roca común). Tal y como es mencionado por DeMeo et al. (2009), la capacidad para caracterizar estos objetos ha crecido junto con los avances en la espectroscopía. Esto debido a que esta técnica permite identificar la forma general del espectro, que es distintiva entre cada taxonomía, así como los detalles particulares en el espectro, tal como la firma espectral de los silicatos en 1 y 2 micras. De esta manera se puede clasificar un objeto y compararlo con muestras de meteoritos para entender su composición detallada. No obstante, este proceso solo funciona para NEOs que son lo suficientemente brillantes para obtener un espectro de alta calidad. Es por eso que la mayoría de los NEOs pequeños que se descubren cada mes, no son estudiados en lo absoluto. A partir del estudio de Groeneveld, Kuiper (1954) se han desarrollado diferentes sistemas taxonómicos para asteroides. El más completo a la fecha es el sistema Bus-DeMeo (DeMeo et al., 2009), que utiliza la firma espectral de la región óptica y del cercano infrarojo para determinar las diferentes clasificaciones.

Se ha observado que los asteroides de tipo C y S predominan en diferentes regiones del sistema solar (Gradie, Tedesco, 1982; DeMeo et al., 2015; Binzel et al., 2019). Sin embargo, las abundancias específicas de estas taxonomías varían en cada región, por lo que las proporciones en los NEOs muestran diferencias con aquellas del cinturón principal (Stuart, Binzel, 2004; Binzel et al., 2019). De manera similar, se observa una posible dependencia de la distribución de composición con el tamaño de los NEOs (Mommert et al., 2016; Binzel et al., 2019; Devogèle et al., 2019). Cabe mencionar que los asteroides de tipo C son generalmente considerados primigenios por la poca alteración que han tenido durante la evolución del sistema solar (Jones et al., 1990), y se caracterizan por tener un albedo bajo¹. Por otro lado, los asteroides de tipo S son los más comunes de aquellos

¹El albedo es la cantidad de luz reflejada por un objeto no emisor en función de la

considerados como alterados o evolucionados (Jones et al., 1990; Fornasier et al., 1999) y cuentan con un albedo mayor.

En el primer párrafo de esta sección se mencionó la motivación general para el estudio de asteroides, adicionalmente, los NEOs son de particular interés porque suelen ser fragmentos de asteroides del cinturón principal traídos a nuestro entorno, ofreciendo entonces una manera indirecta de estudiar objetos del cinturón de asteroides y sus procesos evolutivos, así como los procesos a los que son sujetos una vez estando en el entorno terrestre.

Además de la curiosidad científica, está el creciente interés en la seguridad planetaria. Actualmente se conoce el $\approx 90\%$ de los NEOs mayores a 1 km (Mainzer et al., 2011; Trilling et al., 2017) y sus órbitas no representan un peligro para la Tierra. Por otro lado, se estima que solo hemos observado el $\approx 2\%$ de los de menor tamaño (Trilling et al., 2017), y solo conocemos las propiedades físicas de una pequeña parte de ellos. Estadísticamente este es el tipo de asteroides con más posibilidad de impactar la Tierra, aunque los objetos que conocemos actualmente y sus respectivas órbitas no representan un peligro mayor para ella. Sin embargo hay dos factores a considerar. Primeramente es posible que la órbita de un objeto cercano a la Tierra cambie o que lleguen nuevos objetos desde el cinturón principal. En segundo lugar, el evento de Chelyabinsk nos demostró que un objeto de algunos metros puede causar daños significativos a las comunidades en cualquier parte del mundo (Popova et al., 2013; Brown et al., 2013) y nuestro conocimiento de los objetos de ese tamaño es prácticamente nulo. Es por esto que el entender las propiedades de los NEOs es fundamental para planear estrategias preventivas o de mitigación.

Además del gran interés científico y de seguridad, actualmente existen los fundamentos para la minería espacial, con la Luna y los NEOs como blanco. Este mercado ha despertado interés por parte de diferentes gobiernos e individuos, y aún cuando actualmente no hay una misión activa

luz incidente en este.

al respecto, la intención está claramente definida (Graps, 2019; The White House, 2020; Spa, 2020; AMC, 2020; Hein et al., 2020).

2.3. Sondeos de NEOs

La investigación de NEOs fue impulsada por la seguridad planetaria y la necesidad de identificar los asteroides potencialmente peligrosos (PHAs por sus siglas en inglés). En la década de 1990, los esfuerzos se centraron en encontrar los asteroides capaces de ocasionar un daño global (mayores a un 1 km en diámetro). Después de alrededor de 20 años de trabajo, se determinó que los NEOs de mayor tamaño habían sido suficientemente estudiados en términos de protección planetaria (Harris, 2008; Mainzer et al., 2011). Por lo que durante la última década, la intención fue encontrar aquellos que eran más pequeños pero con capacidad de ocasionar un daño severo a nivel local. Inicialmente se consideró que para este fin había que detectar al menos el 90% de los NEOs >140 m, sin embargo, el evento de Chelyabinsk, provocado por un objeto de máximo 20 m, sugiere objetos de tan solo unas decenas de metros pueden causar daños significativos (Brown et al., 2013).

Durante estas tres décadas, ha habido una gran cantidad de sondeos de NEOs, entre los más destacados por el número de descubrimientos realizados, están, *Catalina Sky Survey* (CSS, Larson et al., 1998), *Lincoln Near Earth Asteroid Research* (LINEAR, Stokes et al., 2000), *Panoramic Survey Telescope and Rapid Response System* (Pan-STARRS, Chambers et al., 2016) y *Asteroid Terrestrial-impact Last Alert System* (ATLAS, Tonry et al., 2018). El propósito de este último va más allá del descubrimiento genérico, pues se enfoca en predecir colisiones que representen una amenaza a nivel local o mundial. Este sistema está actualmente conformado por dos telescopios en Hawái y desde su inicio de operaciones ha descubierto 46 PHAs. Para cumplir su objetivo, los telescopios deben hacer un barrido uniforme del cielo constantemente, lo que produce una gran cantidad de datos que pueden ser aprovechados por distintas disciplinas de la astronomía, tal como fuentes de rayos gamma, candidatos a supernova y estrellas variables (Stalder et al., 2017; Prentice et al., 2018; Heinze

et al., 2018). En lo que respecta a asteroides, la astrometría y fotometría de cada observación realizada son colocadas en el Minor Planet Center, lo que permite a cualquier astrónomo hacer uso de ellas. La caracterización de NEOs es una tarea más difícil, lo cuál se explica en la siguiente sección. A la fecha, entre los sondeos enfocados a la determinación de algún parámetro físico destacan: *EXPLORENEOs* (Trilling et al., 2010a), *Mission Accessible Near-Earth Object Survey* (MANOS, Devogèle et al., 2019) y MIT-Hawaii Near-Earth Object Spectroscopic Survey (MITHNEOS, Binzel et al., 2019), los cuáles han brindado información acerca del tamaño, albedo, emisión térmica y composición. Una discusión más amplia acerca de sondeos de NEOs puede encontrarse en Stokes et al. (2002) y Jedicke et al. (2015).

Al día de hoy, conocemos 901 asteroides mayores a 1 km de diámetro (NASA, 2020a) de los ~ 1000 (Mainzer et al., 2011; Trilling et al., 2017) estimados, y 22,051 (NASA, 2020a) de los $\sim 10^6$ estimados con capacidad de ocasionar daños (Trilling et al., 2017). De los menores a un kilómetro, solo 541 cuentan con algún tipo información física (NASA, 2020b), representando $\approx 3\%$ de la muestra observada y ≈ 0.05 de la muestra de interés. En la década entrante comenzarán a funcionar observatorios de nueva generación donde los NEOs forman parte de los principales intereses científicos (e.g. James Web Space Telescope y Vera C. Rubin Observatory: Gardner et al., 2006; AURA, 2020). Esto nos permitirá estudiar los NEOs en mayor detalle y cantidad, particularmente los pequeños (e.g. Rivkin et al., 2017).

3. Introducción

3.1. Necesidad de técnicas no estándar

Los asteroides tienen emisión térmica en el infrarojo que permite su caracterización física (Allen, 1970; Matson, 1971; Mainzer et al., 2015). Sin embargo en la región óptica tienden a reflejar poca luz y no emiten. La superficie reflectiva de un objeto es proporcional a su tamaño, por lo que los objetos pequeños son aún más difíciles de observar. Los NEOs tienden a ser descubiertos cuando están más cerca de la Tierra, ya que su superficie aparente aumenta y por lo tanto su brillo también, pero por lo general su visibilidad disminuye entre el momento que son descubiertos y cuando es posible observarlos tras la aprobación de una propuesta de telescopio, pues es un proceso tardado. Además, muchos NEOs tienen periodos sinódicos largos, por lo que si se pierde la oportunidad de observarlos después de su descubrimiento, pueden pasar años hasta que sea posible estudiarlos de nuevo. Lo anterior ha contribuido fuertemente a que la cantidad de NEOs pequeños caracterizada sea muy baja. Para abordar este problema utilizamos la técnica *rapid-response*², que consiste en observar los objetos días después de su descubrimiento, cuando aún son lo suficientemente brillantes para estudiarlos. Nos es posible usar esta técnica gracias a la robotización del telescopio de 1.5 m del Observatorio Astronómico Nacional en San Pedro Martir (OAN-SPM). La de capacidad RATIR (instrumento instalado en dicho telescopio, Watson et al., 2012) de obtener información en múltiples bandas simultáneamente contribuyó a aumentar la calidad del análisis en algunos casos. Hemos realizado observaciones utilizando RATIR cada semestre desde 2014 a 2019.

En los artículos presentados en este documento, utilizamos la técnica denominada espectrofotometría, que consiste en mediciones fotométricas en longitudes de onda de particular interés. Se ha demostrado que esta técnica puede ser suficiente para clasificar asteroides (ver por ejemplo Mommert et al., 2016, y las referencias ahí citadas), mostrando una ventaja estratégi-

²Utilizada en los artículos 1 y 3

ca sobre la espectroscopía, ya que colecta la luz en vez de dispersarla, por lo que permite analizar objetos más pequeños o con telescopios de menor tamaño.

Sin embargo, es un hecho que la fotometría ofrece menos información que mediciones espectrales. Por esto, es necesario utilizar técnicas para analizar los asteroides en base a las características estadísticas de la población. En años recientes la inteligencia artificial se ha aplicado ampliamente en diferentes áreas de ciencia y tecnología. La base de esta técnica es que un algoritmo tome decisiones cognitivas. Una de las grandes ramas de la inteligencia artificial es *Machine Learning* (e.g. Kubat, 2017), que consiste en alimentar un algoritmo con una base de datos. Después de que el algoritmo se 'entrena' con dichos datos, es capaz de tomar decisiones basadas en lo que aprendió. Entre las aplicaciones de este mecanismo, está el encontrar patrones y clasificar objetos con alta eficiencia.

Una de las técnicas que utilizamos ampliamente es el método Monte Carlo (MC), el cuál es una herramienta muy útil en casos donde es difícil encontrar una solución de manera analítica y es posible hacer uso de la estadística. Las bases del método se le asignan a Stanislaw Ulam y John von Neumann, y tienen su origen en juegos de cartas (Roger, 1987). Su primera implementación formal fue para estudiar la difusión de neutrones, que pronto dio origen a investigación en el área de armamento nuclear. Con el paso del tiempo se han hecho diferentes variaciones e implementaciones para aplicarlo a diferentes áreas, no solo en investigación científica sino en cualquier área donde pueda aplicarse la estadística. De manera general, el método consiste en realizar experimentos aleatorios para aproximar una solución matemática. En nuestro caso lo utilizamos para dos objetivos diferentes, ambos relacionados con el error de las mediciones. En el primer caso, MC sirvió para aproximar la función de probabilidad asociada a nuestras observaciones en el color $r-i$. La aproximación se construye a partir de una distribución taxonómica definida, de manera que al encontrar una aproximación que ajusta nuestra función, se encuentra la posible distribución

taxonómica de nuestra muestra. En el segundo caso MC se utilizó para aproximar el valor real en el color de un asteroide a partir del valor medido y su error correspondiente.

3.2. Estudio de 3 métodos diferentes para clasificar NEOs

Aún cuando la taxonomía de NEOs no ofrece una composición mineralógica detallada, es uno de los primeros pasos para estudiar la distribución de estos importantes objetos, además de que abre rutas de investigación en el área. En cuanto a seguridad planetaria, a manera de ejemplo reduccionista, los NEOs tienden a descubrirse cuando están más cerca de la Tierra. No es imposible que ATLAS o algún otro observador descubra un objeto que colisionará con la Tierra con solo un par de días de antelación, lo cuál sería insuficiente para planear una estrategia de mitigación. Sin embargo, si se estima su taxonomía, se podría calcular el efecto que la atmósfera tendrá sobre él, y por lo tanto planear medidas pertinentes de prevención o evacuación. Cabe mencionar que los estudios de taxonomía suponen que los asteroides tienen una composición homogénea.

Este documento incluye tres artículos en los que se estudia la taxonomía de asteroides por medio de análisis fotométrico y técnicas estadísticas implementadas en algoritmos computacionales. Se presentan diferentes técnicas para clasificación de asteroides que son convenientes dependiendo de la cantidad de información y recursos que se tengan disponibles. En conjunto, los tres artículos brindan información taxonómica de 1850 asteroides, incluyendo 238 NEOs con diámetro equivalente menor a 1 km. ³

El primer artículo utiliza simulaciones con el método Monte Carlo para analizar la distribución del color $r-i$ de una muestra de 82 NEOs observa-

³Artículos de caracterización de NEOs presentan típicamente apenas algunas docenas de ellos.

dos con RATIR, encontrando que la fracción de asteroides ricos en material orgánico es aproximadamente la misma que la de aquellos de tipo rocoso. Al igual que otros artículos similares, nuestro resultado está sesgado a favor de los objetos más brillantes, por lo que se espera que la fracción real de asteroides rocosos sea menor. Nuestro resultado sugiere una mayor cantidad de objetos con contenido orgánico que la encontrada en estudios previos, sin embargo coincide dentro de las barras de error.

En el segundo artículo se clasifican 1612 asteroides del cinturón principal, pertenecientes a 5 familias diferentes. Para esto se utilizan datos de ATLAS en el color $c-o$ y un método de clasificación más simple que en el artículo anterior. La capacidad de distinguir entre dos clases de asteroides con un solo color permite estudiar la variación taxonómica en las familias y establecer un límite para uno de los modelos de formación de la familia Flora.

El tercer artículo es una continuación del primero, esta vez considerando 5 bandas fotométricas (r, i, Z, Y, J), lo cuál permite implementar un sistema de análisis más robusto basado en ML, que ofrece más precisión y detalle en los resultados. Con este sistema analizamos 87 objetos de la muestra, encontrando resultados que están más de acuerdo con los de estudios previos. También analizamos 151 objetos con los métodos utilizados en los primeros artículos, encontrando que el método más simple no es apto para estudiar la distribución de NEOs. La realización de este último artículo coincidió con la publicación de la muestra clasificada de NEOs más grande a la fecha, la cuál utilizamos como muestra control. El contar con esta base de datos permitió estudiar la eficacia de los diferentes métodos de clasificación. Por lo tanto, además de ofrecer la taxonomía de los objetos, nuestro estudio explora mecanismos de clasificación no ordinarios en el área, aspecto de utilidad para los datos que serán generados por los proyectos de gran escala próximos a operar.

4. Caracterización de NEOs utilizando fotometría de respuesta rápida con RATIR

En este artículo se presentan observaciones en las bandas r e i tomadas en 2014 y 2015. Durante este tiempo la cámara infraroja de RATIR estaba dañada, por lo que decidimos trabajar exclusivamente con mediciones en el rango óptico del espectro. Tomando en cuenta las capacidades del telescopio, cada noche se eligen de manera completamente automática los objetos a observar. Estos se seleccionan de una lista de NEOs recientemente descubiertos, ya que son relativamente más brillantes y por lo tanto es posible estudiarlos.

El artículo se enfoca en encontrar la cantidad de asteroides ricos en contenido orgánico en relación a los objetos con alto contenido de silicatos (expresado como la razón C/S). El análisis de los datos es de tipo estadístico y está basado en el índice de color $r-i$.

Originalmente, la intención era encontrar las abundancias relativas de asteroides de tipo C y S por medio de dos ajustes gaussianos, cada uno centrado en el color característico de estos tipos de asteroides. Los resultados no eran convincentes, por lo que este método solo se utilizó como referencia y a manera de guía para determinar el límite de error fotométrico de las observaciones. Para crear un modelo un poco más robusto, se construyó una función de probabilidad utilizando cada una de las observaciones. Para extraer el resultado de esta función se realizaron 10^7 simulaciones Monte Carlo, considerando asteroides de tipo C, S, X y Q, los cuáles se espera que sean los mayores componentes de nuestra muestra (Thomas et al., 2011; Mommert et al., 2016; Binzel et al., 2019). En cada una de las simulaciones se genera una función de probabilidad asociada a los objetos sintéticos y se compara con la equivalente de nuestras observaciones por medio de la prueba del chi cuadrado reducido.

Este artículo proporciona una herramienta útil para aproximar la dis-

tribución taxonómica en una población contando con solo un color fotométrico. Cabe destacar la utilidad del color utilizado, ya que está en el rango visible, mientras que las características espectrales principales que diferencian las distintas taxonomías están en el cercano infrarojo. Encontramos que nuestra muestra presenta un $C/S=1.06$.

Mis directores de tesis y mi asesor externo, el Dr. Michael Mommert sugirieron la metodología a seguir y me brindaron las referencias que determinan los resultados a esperar. También me ayudaron a analizar o incluso solucionar una situación en etapas cuando no me era claro cómo proceder. Los otros coautores contribuyeron con la pipa de reducción y/o a planear el proyecto del cuál mi investigación forma parte. Dicho esto, yo realicé toda la investigación presentada en este artículo. A continuación se menciona de manera resumida las actividades que llevé a cabo.








Se esperaba que generar el primer artículo fuera trivial, sin embargo los datos no eran congruentes. Por mi participación en el proyecto presentado en la Sección A supuse que RATIR no era apto para estudiar asteroides, sin embargo el Dr Trilling comentó que debería ser posible extraer resultados. Por alrededor de un año hice diferentes pruebas, las cuáles incluyeron: explorar diferentes métodos estadísticos simples para tratar los datos, de esto derivó la implementación posterior del *z-score* (puntaje *z*); estudiar el desempeño de la pipa de reducción, lo que me permitió identificar y descartar observaciones incorrectas con barras de error pequeñas. Modifiqué los resultados de la pipa respecto al punto cero y otro parámetro de calibración, lo cuál no tuvo ningún efecto significativo. El estudio de la pipa sugirió utilizar cada una de las magnitudes observadas durante una visita en vez de utilizar la suma de ellas hecha por la pipa. A consecuencia de lo anterior se escribió un pequeño código para organizar las tablas de datos arrojadas por la pipa. Después de este proceso los datos eran más congruentes, no obstante la distribución de color no era similar a la esperada, por lo que seguía siendo necesario encontrar una manera de extraer los resultados. Evalué el uso de un ajuste gaussiano y de la simulación MC. Para esto hi-

ce pruebas considerando diferentes combinaciones taxonómicas, límites de error para las observaciones, etc., analizando en cada caso la congruencia del resultado obtenido. Escribí todos los códigos para realizar las pruebas, generar y analizar los resultados.

Algunas de las técnicas estudiadas en este artículo son utilizadas en los dos siguientes.



First Results from the Rapid-response Spectrophotometric Characterization of Near-Earth Objects Using RATIR

S. Navarro-Meza^{1,2}, M. Mommert^{2,3} , D. E. Trilling² , N. Butler^{4,5} , M. Reyes-Ruiz¹, B. Pichardo⁶ , T. Axelrod⁷ ,
R. Jedicke⁸ , and N. Moskovitz³ 

¹ Instituto de Astronomía, Universidad Nacional Autónoma de México, Ensenada B.C. 22860, México; snavarro@astro.unam.mx

² Department of Physics and Astronomy, Northern Arizona University, Flagstaff, AZ 86001, USA

³ Lowell Observatory, Flagstaff, AZ 86001, USA

⁴ School of Earth and Space exploration, Arizona State University, Tempe, AZ 85287, USA

⁵ Cosmology Initiative, Arizona State University, Tempe, AZ 85287, USA

⁶ Instituto de Astronomía, Universidad Nacional Autónoma de México, Ciudad Universitaria, D.F. 04510, México

⁷ Steward Observatory, University of Arizona, Tucson, AZ 85721, USA

⁸ Institute for Astronomy, University of Hawaii at Manoa, Honolulu, HI 96822, USA

Received 2018 June 29; revised 2019 March 15; accepted 2019 March 18; published 2019 April 22

Abstract

As part of our multi-observatory, multifilter campaign, we present $r-i$ color observations of 82 near-Earth objects (NEOs) obtained with the reionization and transients infrared camera (RATIR) instrument on the 1.5 m robotic telescope at the San Pedro Martir's National Observatory in Mexico. Our project is particularly focused on rapid-response observations of small ($\lesssim 850$ m) NEOs. The rapid response and the use of spectrophotometry allows us to constrain the taxonomic classification of NEOs with high efficiency. Here we present the methodology of our observations and our result, suggesting that the ratio of C-type to S-type asteroids in a size range of ~ 30 –850 m is 1.1, which is in accordance with our previous results. We also find that 10% of all NEOs in our sample are neither C- nor S-type asteroids

Key words: minor planets, asteroids: individual (near-Earth objects) – surveys

1. Introduction

Solar system minor bodies are tracers of the solar system's formation and evolution, and hence can be used as current samples of the processes that occurred in the early days of the system and its formation (Delsemme 1991; Malhotra 1997). Therefore, studies with numerous samples, focused on analyzing colors, taxonomies, and orbital and physical properties of asteroids from different populations have been made (see, for example, Ivezić et al. 2001; Carvano et al. 2010; Carry et al. 2016).

Near-Earth objects (NEOs) are of particular interest for their potential to explain the disagreement between the composition of meteorite falls on Earth and the composition observed in asteroids (Mommert et al. 2016). Furthermore, the Chelyabinsk event in 2013 showed us that there exist NEOs with the potential to cause moderate to devastating damage to our communities (Brown et al. 2013). It is worth noting that events like this can happen in any point on the globe. This event has motivated projects aimed to characterize those asteroids that could impact the Earth and that have enough energy to compromise its safety.

Discovery and characterization efforts aimed at NEOs have significantly increased in the last years. However, due to their general faintness, characterization of small NEOs lags behind. The most effective way to constrain NEO compositions is spectroscopy, which allows for the identification of both the overall continuum shape and diagnostic band features and enables their taxonomic classification. However, spectroscopy is very expensive in terms of telescope time, and is only possible with relatively bright objects, which generally are the largest objects. Only few small asteroids (with diameters smaller than 100 m) get bright enough to be observed spectroscopically (e.g., Moskovitz et al. 2015). Currently,

DeMeo et al. (2009) offer the most complete taxonomic classification system.

Photometric measurements at a few key wavelengths—*spectrophotometry*—can be sufficient to estimate asteroid taxonomies (see Mommert et al. 2016, and references therein). This technique has the advantage of making faint targets accessible because the light is collected within a broad bandpass instead of being dispersed as a function of wavelength. Furthermore, spectrophotometry can be performed with smaller telescopes than the ones necessary for spectroscopy. Here we present a combination of spectrophotometry and rapid-response observations, i.e., observations that are obtained shortly after the discovery of the target, when it is still relatively bright. This article constitutes the third of a series of papers oriented to taxonomically classify hundreds of small NEOs using spectrophotometry.

C (organic rich) and S (siliceous rock) taxonomic types are the dominant constituents of the distribution of large asteroids (Stuart & Binzel 2004; Thomas et al. 2011). However, the compositional distribution of small NEOs appears to be different from that of Main Belt asteroids, as well as from large NEOs. Mommert et al. (2016) find S and C+X complexes⁹ to be the main components of their sample of small NEOs. Also as pointed out by them, the compositional distribution of meteorite falls does not match the observed NEO distribution, a fact that can yield information on asteroid strength. This fact needs to be studied with better statistics on the small asteroid range in order to better understand the threat to Earth from impactors. It is important to remark that

⁹ Results from Mommert et al. (2016) make no distinction between the C and the X taxonomic complexes. For comparison purposes the notation C+X will be used here, which stands for the set of objects corresponding to both the C- and the X-complexes.

Table 1
Channels of the RATIR Instrument

Channel	Detector	Field size (arc minute square)	Filters
C0	CCD	5.3	SDSS ugr and seven others
C1	CCD	5.3	Fixed SDSS <i>i</i>
C2	H2RG	10	Fixed WFCAM <i>Z</i> and <i>Y</i>
C3	H2RG	10	Fixed MKO <i>J</i> and <i>H</i>

Note. All detectors are 2048×2048 pixels. C0 and C1 channels hold the visual range filters (observations reported in this paper were taken with the *r* and *i* filters), C2 and C3 channels contain the near-infrared filters, and H2RG (HAWAII-2RG) are teledyne mercury–cadmium–telluride detectors.

according to Thomas et al. (2011, 2014), Q-type asteroids can be an important component of a magnitude-biased NEO sample, due to their relatively high albedos. There are other teams interested in this same topic (see for example Ieva et al. 2018; Popescu et al. 2018).

This study is part of a worldwide systematic survey of NEO compositions. With the use of the 3.8 m United Kingdom Infrared Telescope (UKIRT) and KMTNet-SAAO telescope, we provide detailed information on the compositional distribution of NEOs with absolute magnitudes up to $H \sim 28$, i.e., with a few meters in diameter. Such rapid response is generally not feasible through classical observing proposals due to heavily oversubscribed classically scheduled major research facilities. Furthermore, this method allows us to classify small NEOs according to their taxonomy with a higher efficiency than current spectroscopic methods (see Galache et al. 2015 for a discussion). Furthermore, photometric studies of the partial light curves of our objects can lead to the improvement of the period distribution of asteroids on the smaller range (see Warner et al. 2009).

In Section 2 we describe the reionization and transients infrared camera (RATIR), the multiband instrument we use. Section 3 describes our rapid-response approach and the planning of our observations. Section 4 addresses our data selection and analysis. In Section 5 we provide our results and the corresponding discussion is given in Section 6. Finally in Section 7 we discuss the conclusions and the future outlook of this project.

2. Reionization and Transients Infrared Camera

Observations were performed with RATIR (Butler et al. 2012) on the San Pedro Martir (SPM) 1.5 m telescope at the National Mexican Astronomical Observatory (Observatorio Astronómico Nacional). This telescope is a Ritchey–Chrétien type, operated by the Universidad Nacional Autónoma de México. The instrument is equipped with two optical and two near-infrared (NIR) detectors, all of them 2048×2048 pixels. Each of these detectors corresponds to a different channel with specific filters, as shown in Table 1. RATIR takes four images of an object in a single shot.¹⁰ To minimize dark current and thermal background effects, the optical detectors are water cooled, while the NIR detectors are operated in a helium-cooled cryostat.

RATIR was designed to study gamma-ray bursts (e.g., Butler et al. 2017a, 2017b, 2017c), but other uses are possible as

¹⁰ See detailed information on RATIR’s web page: <http://ratir.astroscu.unam.mx>.

Table 2

Each of the Reported Targets According to Their Number or Designation, Observation Midtime of the Observing Run, and the Duration of the Run

Object	Obs. Midtime (UT)	Dur. (hr)	H_V (mag)	$r-i$ (mag)	Error (mag)
2014 MK6	2014 Jul 22 09:30	1.7	21.00	0.29	0.01
2014 MP5	2014 Jul 21 05:25	1.5	21.80	0.27	0.02
2014 OZ337	2014 Aug 04 08:13	0.3	22.50	0.35	0.02
2014 QQ33	2014 Aug 25 10:20	1.3	22.10	0.30	0.02
2014 TT35	2014 Oct 18 03:49	0.1	26.00	0.49	0.01
2014 TZ	2014 Oct 23 05:12	1.1	22.60	0.33	0.01
2014 UT192	2014 Nov 10 09:03	0.2	19.60	0.46	0.03
2014 UZ116	2014 Nov 03 06:41	1.6	20.90	0.36	0.04
2014 WX4	2014 Nov 20 07:16	0.5	26.40	0.40	0.02
2014 WZ4	2014 Nov 20 03:42	0.5	23.50	0.29	0.03
2014 YE35	2015 Jan 15 08:32	0.5	20.30	0.38	0.01
2014 YW34	2015 Jan 15 06:53	1.6	21.60	0.25	0.06
2015 EL7	2015 Apr 05 10:19	0.4	22.70	0.38	0.03
2015 EL7	2015 Apr 09 07:40	0.2	22.70	0.39	0.06
2015 EL7	2015 Apr 11 07:22	0.1	22.70	0.36	0.03
2015 EZ	2015 Mar 15 05:56	0.4	20.30	0.40	0.01
2015 FG120	2015 Apr 10 09:12	1.1	22.90	0.36	0.02
2015 FG120	2015 Apr 11 09:20	0.2	22.90	0.29	0.03
2015 FG120	2015 Apr 12 09:35	1.0	22.90	0.30	0.02
2015 FG120	2015 Apr 13 08:07	0.9	22.90	0.38	0.02
2015 FG120	2015 Apr 17 11:09	0.7	22.90	0.37	0.02
2015 FG37	2015 Apr 15 10:53	1.1	21.70	0.41	0.02
2015 FG37	2015 Apr 22 11:25	0.1	21.70	0.29	0.04
2015 FL290	2015 Apr 09 05:11	1.1	22.20	0.36	0.02
2015 FL290	2015 Apr 10 04:53	1.1	22.20	0.37	0.02
2015 FL290	2015 Apr 11 04:46	1.2	22.20	0.39	0.01
2015 FQ	2015 Mar 29 05:43	0.9	22.30	0.40	0.02
2015 FT118	2015 Apr 20 10:50	0.6	20.40	0.30	0.04
2015 FY284	2015 Apr 02 07:13	0.5	21.60	0.37	0.05
2015 GS13	2015 May 14 09:26	0.4	21.00	0.51	0.03
2015 GS	2015 Apr 15 09:34	1.1	20.60	0.35	0.02
2015 GS	2015 Apr 16 09:53	1.2	20.60	0.33	0.02
2015 GY	2015 Apr 15 05:14	0.6	21.70	0.41	0.01
2015 GY	2015 Apr 19 07:16	0.5	21.70	0.27	0.02
2015 HA1	2015 Apr 25 09:04	0.9	21.20	0.46	0.01
2015 HA1	2015 May 05 07:50	0.5	21.20	0.45	0.01
2015 HP171	2015 May 12 09:32	0.3	20.10	0.34	0.02
2015 HR1	2015 May 06 08:59	0.7	24.30	0.35	0.06
2015 HR1	2015 May 07 09:00	0.4	24.30	0.34	0.06
2015 HR1	2015 May 13 09:39	0.7	24.30	0.26	0.03
2015 HV171	2015 May 08 08:55	0.1	18.10	0.36	0.01
2015 HW11	2015 May 12 07:04	1.1	23.30	0.41	0.02
2015 JQ1	2015 May 18 05:03	1.0	20.30	0.26	0.05
2015 JQ1	2015 May 19 05:45	1.0	20.30	0.28	0.02
2015 KL122	2015 Jun 05 09:19	0.5	22.30	0.47	0.07
2015 KQ120	2015 May 30 10:10	0.1	26.70	0.43	0.04
2015 KQ57	2015 May 26 05:17	0.0	22.20	0.40	0.04
2015 KV18	2015 May 23 09:41	0.8	23.80	0.42	0.03
2015 KV18	2015 May 24 09:28	0.8	23.80	0.37	0.04
2015 KV18	2015 May 25 07:40	0.2	23.80	0.31	0.02
2015 KV18	2015 May 26 07:40	0.1	23.80	0.41	0.03
2015 LA2	2015 Jun 14 06:35	1.0	23.10	0.33	0.01
2015 LG14	2015 Jun 22 06:22	1.0	23.20	0.40	0.03
2015 LG14	2015 Jun 23 06:03	0.8	23.20	0.52	0.04
2015 LG2	2015 Jun 18 07:18	1.0	20.30	0.40	0.03
2015 LG2	2015 Jun 21 08:41	0.8	20.30	0.37	0.02
2015 LJ24	2015 Jun 18 05:11	0.2	20.00	0.42	0.03
2015 LJ	2015 Jul 04 06:43	0.8	24.70	0.45	0.05
2015 LJ	2015 Jul 04 07:50	0.8	24.70	0.33	0.07
2015 LJ	2015 Jul 13 05:21	0.8	24.70	0.27	0.03
2015 LJ	2015 Jul 25 06:54	0.9	24.70	0.29	0.06
2015 LQ21	2015 Jun 21 05:01	0.1	24.50	0.50	0.03

Table 2
(Continued)

Object	Obs. Midtime (UT)	Dur. (hr)	H_V (mag)	$r-i$ (mag)	Error (mag)
2015 MC	2015 Jun 20 06:18	0.2	24.10	0.45	0.02
2015 MC	2015 Jun 26 06:49	0.9	24.10	0.30	0.04
2015 ME116	2015 Jul 14 04:57	0.3	22.30	0.38	0.06
2015 ME116	2015 Jul 25 04:49	0.4	22.30	0.27	0.04
2015 MQ116	2015 Jul 15 08:09	0.8	23.40	0.35	0.05
2015 MS59	2015 Jul 13 10:15	0.9	21.00	0.25	0.01
2015 MS59	2015 Jul 14 09:26	0.9	21.00	0.49	0.02
2015 MS59	2015 Jul 15 09:25	1.0	21.00	0.41	0.02
2015 MS59	2015 Jul 23 09:48	0.9	21.00	0.37	0.04
2015 MU59	2015 Jul 09 10:01	0.8	20.00	0.31	0.02
2015 MU59	2015 Jul 13 09:15	0.8	20.00	0.44	0.01
2015 MU59	2015 Aug 04 08:44	0.6	20.00	0.39	0.01
2015 MX103	2015 Jul 04 05:13	0.5	24.40	0.46	0.02
2015 MX103	2015 Jul 06 06:16	0.6	24.40	0.38	0.02
2015 MY53	2015 Jul 03 05:59	0.5	25.40	0.39	0.06
2015 MY53	2015 Jul 03 06:49	0.2	25.40	0.52	0.03
2015 NK13	2015 Aug 04 07:07	0.8	21.00	0.40	0.03
2015 NK3	2015 Aug 04 05:56	0.8	21.30	0.26	0.03
2015 NK3	2015 Aug 07 06:57	1.0	21.30	0.28	0.01
2015 NU2	2015 Jul 21 07:10	0.6	20.90	0.28	0.04
2015 NU2	2015 Jul 24 05:15	1.1	20.90	0.35	0.04
2015 OF26	2015 Aug 07 05:37	0.3	21.60	0.32	0.02
2015 OM21	2015 Jul 24 09:55	0.7	22.50	0.38	0.03
2015 OM21	2015 Aug 06 08:00	0.9	22.50	0.45	0.03
2015 OM21	2015 Aug 07 08:05	1.0	22.50	0.48	0.02
2015 PA229	2015 Aug 21 09:39	1.0	21.40	0.41	0.02
2015 PA229	2015 Sep 05 08:55	1.0	21.40	0.39	0.05
2015 PQ56	2015 Sep 03 07:59	0.9	22.60	0.46	0.04
2015 PQ	2015 Sep 07 07:52	0.7	22.70	0.48	0.01
2015 QB	2015 Aug 21 08:32	1.0	24.20	0.39	0.01
2015 QG	2015 Aug 22 05:17	0.3	23.80	0.33	0.02
2015 QM3	2015 Aug 23 04:45	0.4	20.40	0.28	0.05
2015 QN3	2015 Aug 23 04:20	0.4	19.50	0.28	0.01
2015 QN3	2015 Aug 24 04:56	0.4	19.50	0.40	0.01
2015 QO3	2015 Aug 24 07:05	0.6	19.40	0.38	0.01
2015 RH36	2015 Sep 18 09:57	0.5	23.60	0.37	0.06
2015 RO36	2015 Sep 18 05:36	0.3	22.90	0.24	0.03
2015 RO36	2015 Sep 16 07:25	1.0	24.50	0.36	0.01
2015 RQ36	2015 Sep 19 09:05	0.6	24.50	0.35	0.02
2015 SO2	2015 Sep 26 09:01	0.3	23.90	0.37	0.03
2015 SO2	2015 Sep 27 09:33	0.3	23.90	0.29	0.03
2015 SO2	2015 Sep 28 10:57	0.3	23.90	0.50	0.03
2015 SO2	2015 Oct 02 11:21	0.4	23.90	0.32	0.03
2015 SV2	2015 Sep 29 05:31	0.9	20.80	0.33	0.03
2015 SY	2015 Oct 01 06:35	0.7	23.30	0.44	0.02
2015 SY	2015 Oct 02 06:09	0.8	23.30	0.33	0.03
2015 SZ	2015 Oct 02 05:22	0.4	23.50	0.36	0.01
2015 TE	2015 Oct 08 04:26	0.5	22.50	0.43	0.02
2015 TF	2015 Oct 10 05:15	0.6	22.20	0.39	0.01
2015 TW178	2015 Oct 26 04:18	0.9	21.20	0.28	0.04
2015 TY144	2015 Oct 26 10:14	0.5	21.30	0.48	0.05
2015 TY178	2015 Nov 06 06:52	0.7	21.80	0.32	0.04
2015 UJ51	2015 Oct 27 07:41	0.7	21.40	0.38	0.03
2015 US51	2015 Oct 28 04:54	0.6	22.40	0.44	0.02
2015 US51	2015 Nov 01 05:02	0.8	22.40	0.43	0.01
2015 US51	2015 Nov 02 04:35	0.8	22.40	0.44	0.01
2015 UT52	2015 Nov 05 07:40	0.8	20.90	0.45	0.03
2015 UT52	2015 Nov 11 10:56	0.6	20.90	0.40	0.04
2015 VJ2	2015 Nov 10 09:36	0.4	19.60	0.44	0.02
2015 VJ2	2015 Nov 18 10:50	0.2	19.60	0.37	0.03
2015 VJ2	2015 Nov 19 10:06	0.6	19.60	0.26	0.01
2015 VO66	2015 Nov 14 10:06	0.4	20.60	0.25	0.03
2015 VO66	2015 Nov 19 08:20	0.5	20.60	0.28	0.01

Table 2
(Continued)

Object	Obs. Midtime (UT)	Dur. (hr)	H_V (mag)	$r-i$ (mag)	Error (mag)
2015 VZ2	2015 Nov 19 04:15	0.9	22.70	0.46	0.04
2014 OT338	2014 Aug 17 11:10	1.4	21.40	0.45	0.02
2014 TX32	2014 Oct 16 05:35	1.1	20.20	0.42	0.01
2015 DE176	2015 Feb 28 06:18	1.0	19.70	0.35	0.03
2015 JV	2015 May 19 07:35	0.8	21.50	0.33	0.01
2015 KJ19	2015 May 24 04:53	0.6	22.50	0.28	0.07

Note. Also presented are the measured color indices (solar colors have been subtracted) and corresponding uncertainties.

shown here (see also García-Díaz et al. 2014; Tapia et al. 2014; Ricci et al. 2015). Observations are executed in an automated queue mode (Watson et al. 2012) if no gamma-ray burst events are ongoing. The results that we present are the first asteroid observations made with the instrument.

3. Observations

The observations we present here were taken during 2014 and 2015. During most of 2015 and 2016, RATIR's channels C2 and C3 (see Table 1) were not available due to technical problems. In this work, we analyze the set of optical-only data. Since the second half of 2016 we are obtaining observations in all four channels, which will be presented in a future publication. Table 2 presents the targets analyzed on this paper, among the main details from their observation.

Our rapid-response approach is the key feature of this project. We trigger rapid-response spectrophotometric observations of NEOs within a few days of their discovery when the objects are generally still bright enough to be observed with a 1.5 m aperture. We can observe and characterize objects as faint as $V \sim 20$. Such rapid response is generally not feasible through classical observing programs. The first results of NEO observations made by our team are presented in Mommert et al. (2016) and Erasmus et al. (2017).

Potential targets are identified and uploaded into the RATIR queue on a daily basis. Accessible targets are identified among those NEOs that have been discovered within the last four weeks; this duration is partially arbitrary,¹¹ but the method usually leads to a number of well-observable and bright potential targets. A target is considered accessible if it has a visible brightness $V \leq 20$ and an airmass ≤ 2.0 , as provided by the JPL Horizons system (Giorgini et al. 1997), for at least the duration of the estimated RATIR integration time. Potential targets are manually selected from the list of accessible targets, prioritizing objects with high absolute magnitudes H_V (small sizes) and large values of $H_V - V$, where V stands for the apparent magnitude of the target of the upcoming night. A high value of $H_V - V$ ensures that our target is observed when it is close to the Earth. RATIR queue observing scripts are automatically created for the selected targets, using the latest orbital elements of the objects of interest provided by JPL Horizons. The exposure time of each frame, as well as the total integration time in each band per visit, are a function of the object's brightness. Exposure times usually range between 5

¹¹ After the closest approach, NEOs fade at a rate of typically 0.5 mag within 1 week and 5 mag within 6 weeks (Galache et al. 2015).

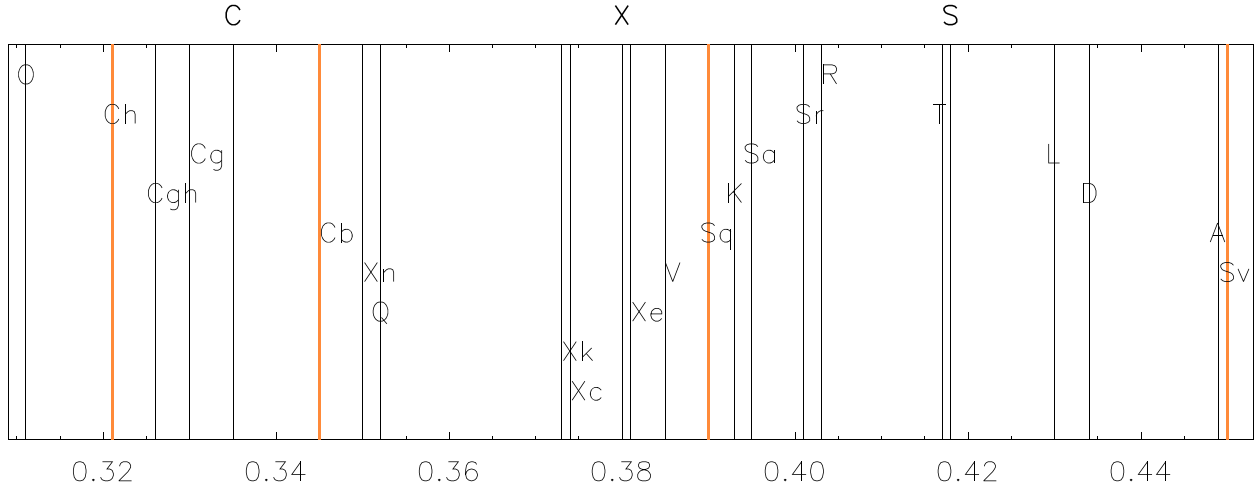


Figure 1. All $r-i$ indices considered in this work according to the Bus-DeMeo taxonomies. Orange lines are the subtypes that are most distant from the C- and S-type respectively, thus defining the limits of these complexes. Notice that the C and S subtype are in the middle of their complexes.

and 30 s, while the total integration time per target is usually less than 1 hr.

Our observations are biased in favor of bright objects. At a given distance from Earth, for objects of a given diameter, objects with higher albedo are easier to observe. For targets close to our limiting magnitude, only those with relatively high albedos will be observed. Hence, our sample may contain a higher fraction of S and Q objects than the actual asteroid population.

4. Data Analysis

4.1. Taxonomic Classification

We use the Bus-DeMeo classification scheme (DeMeo et al. 2009) to classify our sample. This is a widely used taxonomic scheme that combines the visible and near-infrared ranges, covering from 0.45 to 2.45 μm . The taxonomy includes 24 classes, most of which correspond to the C-, S-, and X-complexes that include the majority of the known asteroids (see DeMeo et al. 2009, and Section 1). For this reason, we considered these three complexes in our analysis, as well as the Q-type, which, as described by Thomas et al. (2011, 2014), can be an important component of a magnitude-biased NEO sample like ours. Other taxonomic types were not considered, as they are not expected to be a significant part of the distribution (perhaps up to 20%; Mommert et al. 2016; Erasmus et al. 2017; Lin et al. 2018; Perna et al. 2018) and due to the simplicity of our model. We revisit this assumption below.

We obtain the characteristic color of each taxonomic type from a sample of measured asteroid spectra.¹² For each object from the sample, its reflectance spectrum is convolved with the spectral response of each filter of RATIR and the solar spectrum. Details of the process can be found at Mommert et al. (2016, their section Section 3. Figure 1 shows these color indices in the $r-i$ color.

4.2. Photometry

Image reduction and photometry is carried out using a pipeline developed for gamma-ray burst observations (see, e.g., Littlejohns et al. 2015; Becerra et al. 2017). Briefly, the

pipeline reduces, sky-subtracts, and aligns input frames. These frames are then stacked into a sky image. The stellar point-spread function (PSF) is determined and fit using custom Python scripts to determine the photometric zero-point in comparison with the Sloan Digital Sky Survey (SDSS), Two Micron All Sky Survey (2MASS), and/or The United States Naval Observatory (USNO) photometric catalogs. After finishing the gamma-ray burst pipeline reduction, we create a source mask using the sky image. By then coadding the frames in the moving frame of the target, keeping track of the exposure per pixel, the non-moving sources are removed and we retain only the signal from the target. The PSF determined from the sky image is then fit to the moving-target image and the zero-point from the sky image is applied to normalize the photometry.

The magnitude of an object as a function of the observing time is generated by dyadically combining the masked frames, selecting a sufficiently long time interval for each photometric epoch as to adequately fill in masked pixels prior to PSF fitting. In principle, single frame photometry is possible because we propagate the exposure pixel by pixel; however the accuracy can depend strongly on the stability of the PSF.

Therefore, the pipeline yields photometry on the original image, on a set of stacked images, and on the overall visit's stacked frame. The stacking creates new images with different virtual exposure times, which are integer multiples of the real exposure time. The result of this procedure is available in data tables and through a graphical display in a private data portal. In our analysis we use the photometry measured in individual r -band and i -band images. With this information we measure the $r-i$ color index. The solar $r-i$ was subtracted from our measurements in order to make them compatible with the synthesized colors (see Section 4.1).

4.3. Outlier Rejection

In order to reject photometric outliers we performed a 10σ clipping on the $r-i$ index for each visit: a weighted mean of the $r-i$ index was taken, then any measurement further than 10σ from the mean was rejected and the weighted mean was calculated again. This process was carried out three times. Each time the photometric errors from the individual measurements were propagated to obtain the weights (Taylor 1997).

¹² <http://smass.mit.edu/minus.html>

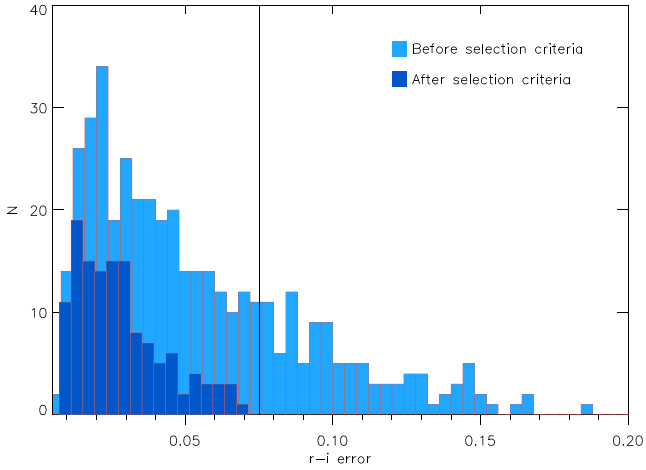


Figure 2. Error distribution of the color from our sample. The vertical line shows the upper error limit set for the sample. See Section 4.4 for details on the selection criteria used.

Therefore, the corresponding error on the $r-i$ index from a visit is

$$\zeta = \frac{1}{\sqrt{\sum w_k}}, \quad (1)$$

where

$$w_k = \frac{1}{e_k^2} \equiv \frac{1}{e_r^2 + e_i^2}, \quad (2)$$

where e_k is associated with the $r-i$ from each of the non-rejected data points of that visit and e_r and e_i are the photometric errors from the r - and i -band measurements. The values of ζ are plotted in Figure 2.

4.4. Selection of the Best Observations

We only consider measurements of those objects that passed through all of our selection criteria, the first of which is a clean visit-stacked image: a well-defined source and a successful removal of the non-moving sources (see Section 4.2 for details on the photometry). Note that we use the visit-stacked image only to check the quality of the photometry and of the observation itself, e.g., with respect to background sources confusion. Also, a limit on the color index's error due to photometric uncertainty must be set. The difference in color index between the C- and S-type asteroids is 0.084, hence it is convenient that we only consider the objects that have an error lower than this threshold. Based on the discussion on Section 6.2, we decide to use 0.075 as an upper error limit on the color determination. We require a minimum of four measurements per visit.

The outcome of this selection process is 82 different objects observed in 131 visits.

4.5. Probability Density

After the selection process described in the previous section, we have one $r-i$ index and its associated error for each visit in our clean sample. These indices are shown in Figure 3. In order to analyze the taxonomic distribution of our sample, we model it based on the known asteroid colors. We consider every count in Figure 3 as a normalized Gaussian centered at the $r-i$ value

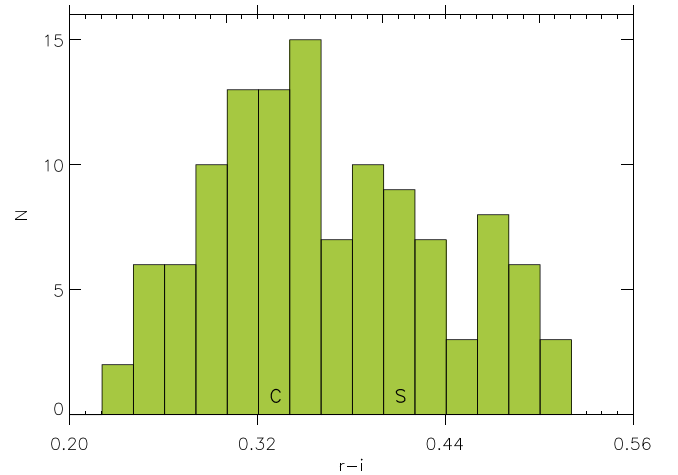


Figure 3. Color distribution of our sample. Color indices were obtained after performing the rejection process described in the text. The main subtypes from the C- and S-complex are shown (see Figure 1).

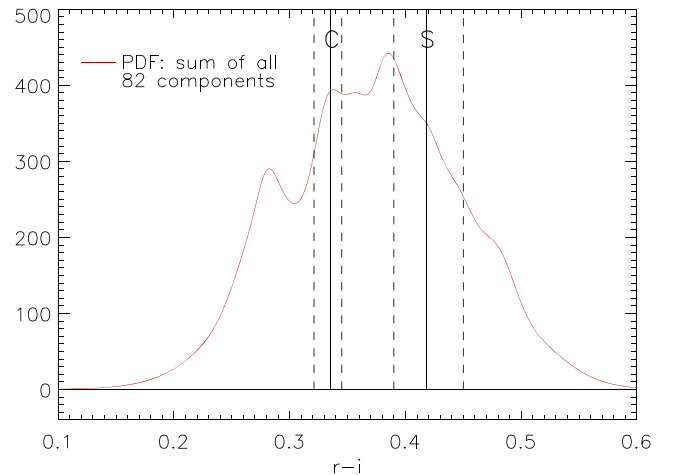


Figure 4. Probability density function of the color in our sample. Every visit is considered as a Gaussian centered in the color index obtained. Vertical lines represent the limits of the C- and S-complexes. See the text for a full explanation.

of that object with the width of the Gaussian equal to the error on the $r-i$ index (the height is therefore a free parameter). For objects observed more than once, the Gaussian's normalization factor is divided by the number of visits each object has. That way an object observed in more than one visit will be represented by different Gaussians, all of which add up an area of unity. The Gaussians corresponding to all objects were added up to obtain the probability density function (PDF), shown in Figure 4.

4.6. Monte Carlo Simulation

In order to measure the compositional distribution from the PDF, we conducted a Monte Carlo (MC) simulation, which consists of creating 10^7 samples of synthetic asteroids, each sample with the same number of objects as our data sample but with different taxonomic distributions. In each run the S-, C-, and X-complexes and the Q-types are considered, and the number of objects in each taxonomy is set with a pseudo-random number generator. We call the resulting color index distribution from each run the random probability density

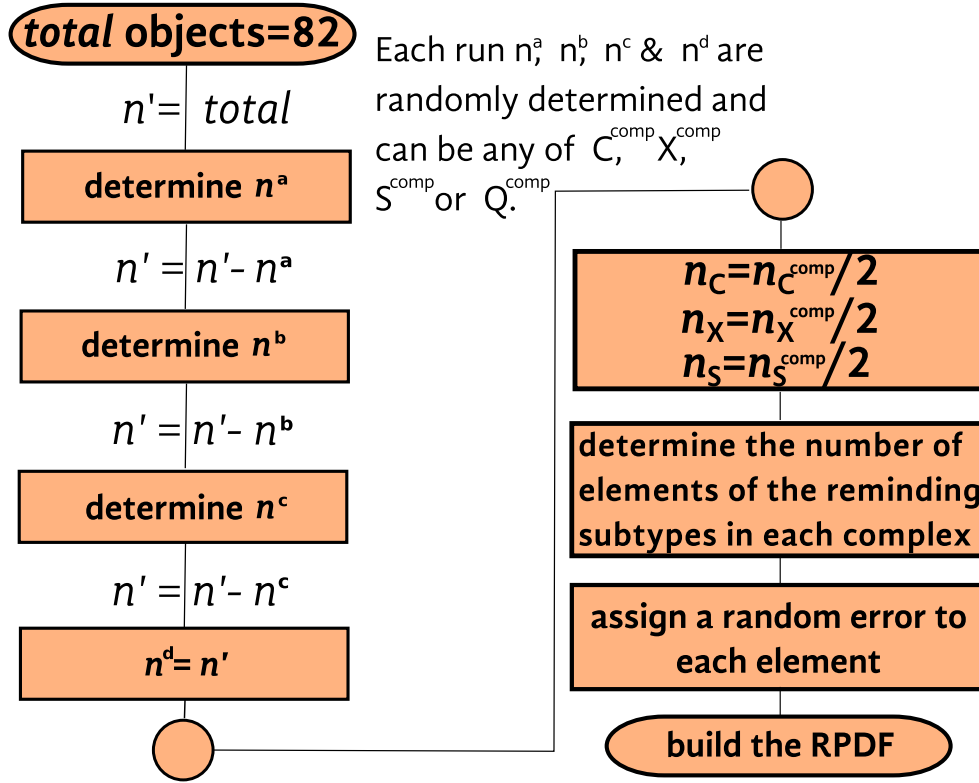


Figure 5. Main processes in the Monte Carlo simulation. Particularly the procedure for setting the number of objects of each type in the synthetic sample. Every box including the word “determine” involves a random process. n is the number of objects of a certain type or complex in a single run; the subindex indicates the referred taxonomy. Since there are C-, S-, and X-complexes, as well as a C-, S-, and X-types, a super index comp indicates when the variable is associated to the complex. n' is the number of objects available for the unassigned taxonomies at a certain point.

function (RPDF) to distinguish it from the PDF from our data. The process to generate each distribution is the same. The details of our MC simulation are as follows.

Eighty two synthetic objects were used in each MC run in order to directly compare the RPDF with the PDF. From Mommert et al. (2016) and Erasmus et al. (2017), we expect the C- and S-type asteroids to be the main components of our sample, and to find a C/S ratio of ~ 1 . However, we take into account the possibility that our sample is composed of any combination of the taxonomic types considered. This is achieved by using a pseudo-random number generator under a uniform distribution with equal weights for the three complexes and the Q-type. The process to obtain the composition on each of the runs is as follows.

The order in which the number of elements is set for each complex and the Q-type is randomly sorted. Each of them is labeled as n^a , n^b , n^c , or n^d . The assignation of the number of elements is always in alphabetical order, however the correspondence between the types and n^{a-d} is given by the pseudo-random number generator. Then n^a can be assigned with any number between 0 and 82, the availability for n^b is $82 - n^a$, and similar for n^c and n^d .

The main subtypes of the complexes, respectively the C-type, S-type and X-type, are the most likely to be present in our sample (Binzel et al. 2015). Therefore, in each of the random generated samples, half of the elements assigned to each complex are given to the main subtype, while the other half is uniformly distributed among the other subtypes (see Figure 1 for the $r-i$ index of each of the members of these complexes). The number of elements in the second half will

likely not be an integer multiple of the number of subtypes. For example, if 36 elements are assigned to the S-complex, 18 will correspond to the main type, the S-type. The remaining 18 will correspond to the other 4 subtypes of the complex, but $18 / 4$ is not an integer. The procedure is therefore as follows. If the number of elements assigned to the four subtypes are n_{S1} , n_{S2} , n_{S3} , and n_{S4} , then $n_{S1} = \text{round}(18/4) = 5$; $18 - 5 = 13$ elements available for the three other subtypes, $n_{S2} = \text{round}(13/3) = 4$; $13 - 4 = 9$, $n_{S3} = \text{round}(9/2) = 5$; and $9 - 5 = 4$, $n_{S4} = 4$.

In each run, the correspondence between the n_{S1-4} and the four subtypes is randomly sorted, so that over the 10^7 samples generated, none of the four subtypes are favored. The same criteria apply for the C- and the X-complex. The main processes of the simulation are represented in Figure 5.

After applying all the selection criteria (see Section 4.4), some of the objects that were observed during different visits showed a different $r-i$ index. This fact was not considered in the building of the RPDF. In the simulation, the elements that are not members of the C- or the S-complex are defined as pollution.

Once the number of elements of each type in a single run is determined, it is necessary to add an error to them in order to emulate the photometric uncertainty. In order to take this into account, we fitted a Gaussian function to the distribution from Figure 2 and created a random distribution under that function. Eighty two errors from that distribution were assigned to the $r-i$ indices of each of the determined types. This completes our generated sample. Eighty two elements were randomly selected following a distribution based on current NEO observations.

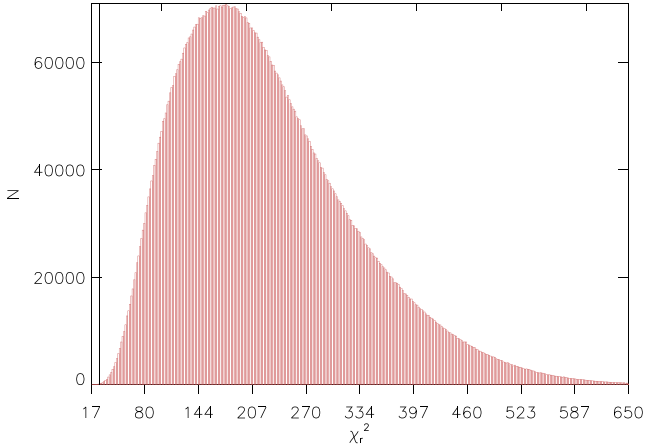


Figure 6. χ_r^2 from the 10^7 MC simulations. Vertical line shows the domain of the first percentile of simulations in terms of the χ_r^2 .

Each of the elements has an associated error, based on the error distribution of our observations. Having these, the RPDF was built up. After creating the 10^7 samples, the PDF was compared to each of the 10^7 RPDFs.

5. Results

In order to extract the results from the simulations, we calculated the reduced χ^2 (χ_r^2) between the RPDF and the PDF. Since we are allowing the simulation to create any possible combination of the taxonomies considered, the χ_r^2 range is wide as can be seen in Figure 6. We took the first percentile of simulations in terms of the χ_r^2 . This is a set of 88 simulations ($\sim 10^{-5}$ from the total). The difference in χ_r^2 between the best and the second-to-best case is minimal. Both present 36 elements of the S-type, the first one suggests 38 C-types, while the second 39. The main difference is in the number of X- and Q-type objects. To analyze the behavior of the best cases we calculated the distribution of the ratio C/S, which is shown in Figure 7. Our best case corresponds to a value of 1.06 in this space. Notice that value is well within 1 standard deviation from the mean, but not in the bin where the mean of the distribution is. We ascribe this to the fact the histogram is skewed to the left, which is discussed in the next section. Table 3 shows the percent compositions of the four taxonomic types considered according to our best case. The errors correspond to the standard deviation of the individual distribution of each class within the 1st percentile. Although we present results on the three complexes and the Q-type, the scope of this analysis is restricted to suggest a C/S ratio. All of our targets have a subkilometer diameter. We do not report subdivisions in size since there was not a clear trend on the results by doing so.

6. Discussion

6.1. Limitations and Comparison with Previous Studies

The strongest bias in our sample is the one presented by albedo. Our rapid-response approach is based on optically discovered objects, hence the sample targets are more likely to have moderate to high surface albedos. This can lead to an overestimated fraction of S objects, which means the real fraction of C/S can be higher than that estimated here. Hence, our sample is biased, and although debiasing of NEOs had been

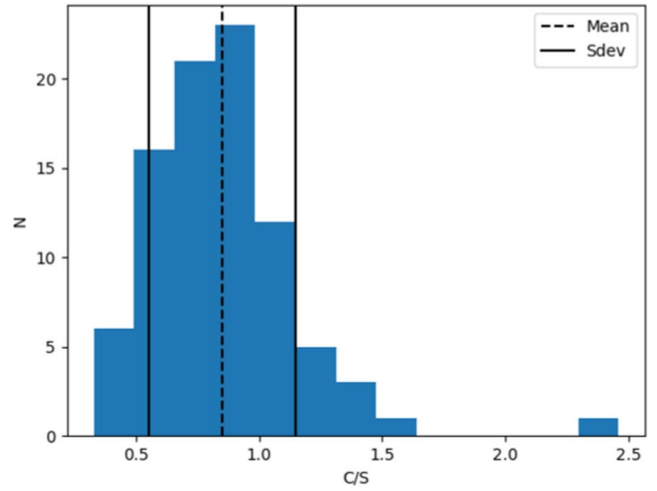


Figure 7. C/S distribution from the 1st percentile of our MC simulations in terms of χ_r^2 . Note that the element in the far right is the 66th best fit, therefore not considered an issue but still considered in the estimation of the mean and standard deviation.

Table 3
Compositional Fractions Found in Our Monte Carlo Simulation

Taxonomic Type	Percentage
C	46 ± 9
S	44 ± 8
X	8 ± 9
Q	2 ± 8

carried out (Stuart & Binzel 2004; Hinkle et al. 2015), we will address it in a future work.

Our full sample contains observations in up to six different bands in the optical and near-infrared range. However, the results presented here correspond to our control sample using only the $r-i$ color. Hence, one of the main goals of this paper is to describe the methodology we are using for our observations. Our future work will include data in all bandpasses.

The distribution in Figure 7 is skewed to the left due to the feature at $r-i \sim 0.26-0.30$ in Figures 3 and 4. It is likely due to a systematic error in the observations causing a bluer color. The analysis of the complete sample will allow us to test this idea.

Our full sample is one of the largest for small NEOs. The analysis of it as well as the work from other teams is needed for a comprehensive classification of these kinds of objects. (As a comparison, Ivezić et al. 2001 made a study of the Main Belt including $\sim 13,000$ objects). The results from other teams on a similar size range to ours (subkilometer) are compared next. The fraction of S-type we find is in agreement within the error bars of the other studies: Ieva et al. (2018), from the analysis of 67 NEOs found $\sim 61\%$ of S-types; Lin et al. (2018), presents 51 subkilometer NEOs. With this sample they found an S fraction of $\sim 33\%$. Perna et al. (2018), for a sample of 146 objects, found an S fraction of $\sim 40\%$. Our team, using different telescopes and samples than the one presented in this paper, found $\sim 40\%$ with 40 NEOs in Mommert et al. (2016), while Erasmus et al. (2017), with a sample of 45 objects, obtained an S fraction of $\sim 43\%$. Using a sample of 252 objects Stuart & Binzel (2004) found an S-type fraction of 22%. This number is a reference for the distribution of NEOs, but is not directly comparable with our results since they performed bias

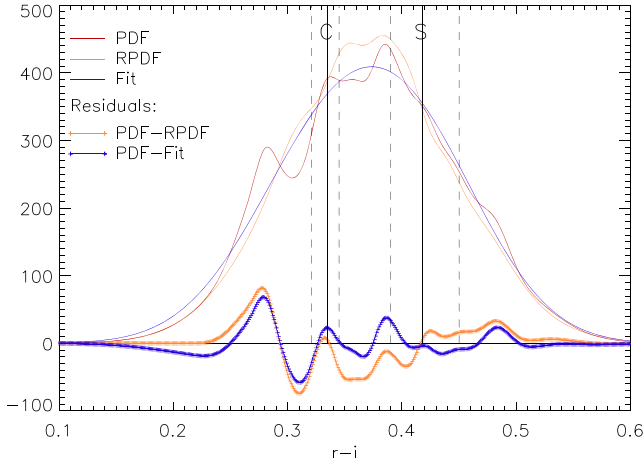


Figure 8. Probability density function (red) of the color in our sample. Equivalent to Figure 4, this time the best result from our MC simulation is overplotted (RPDF, orange). A Gaussian fit to the PDF is also overplotted (blue). Both the RPDF and the fit make a good match with the data, as can be seen on the residuals (dashed orange and blue). See Sections 5 and 6.2 for details.

correction, their sample includes Mars crossing asteroids, and includes objects up to the 10 km scale. Binzel et al. (2019) uses a sample of 1040 objects, with a median of 0.7 km and finds an S fraction of $\sim 50\%$. The C-type fraction found in these same papers varies and can be as low as 10% versus the $\sim 46\%$ we suggest.

6.2. Gaussian Fit

With the purpose of getting a result independent from the MC simulation, we performed a Gaussian fit on the PDF, for which, we considered two components with fixed mean: one centered on the color index of C-type asteroids (0.335), and the other one centered on the color index of S-type asteroids (0.418).

The result from our fit is overplotted to the PDF and RPDF in Figure 8. The two components of the fit are equivalent to 48% of S-type objects and 52% of C-type objects yielding $C/S = 1.07$, which is the same value than in the MC result. The residual (dashed blue in the figure) does not show a systematic behavior, and it is similar to the residual of subtracting the RPDF from the PDF (dashed yellow curve in the figure), so we assume this is primarily noise.

Fits considering other taxonomic types were made, yielding a larger residual. Because of this observation we decided only to consider the C- and S-type in the fitting process.

As can be seen in Figure 9, the width of both the C and S Gaussian distributions from our fit are wider than that of the PDF. This does not affect the result since we are using the ratio of the areas under the fits, but we explore different limits of integration on the abscissa axis for getting each of the areas:

- (a) $[-\infty, \infty]$
- (b) integrating under the limits of the taxonomic types plus the maximum error allowed in color (0.075);
- (c) and $[-\infty, \text{mid}_z]$ for the C Gaussian and $[\text{mid}_z, \infty]$ for the S Gaussian,

where mid_z is the middle point between the $r-i$ index of the C and S taxonomic complexes in terms of the z -score.

The three integration limits are shown in Figure 9. They yield a similar C/S ratio, but, method (b) proved to be more stable as a function of the pollution in test runs of the MC¹³ analysis. With the use of this method we made a cut in the tails of the Gaussians, obtaining more localized components. Notice from Figure 1 that the main types of the C- and S-complex are positioned nearly at the center of their corresponding complex range, making the integration reliable.

We explored the C/S ratio (obtained in Section 4.5) as a function of the upper error allowed in the clean sample. This dependence is shown in Figure 10. Excluding the extremes of the abscissa range on this plot, the C/S ratio does not present a strong dependence on the error limit. Additionally, more than 70% of the objects that passed our other selection criteria have an error lower than 0.075 (and most of the asteroids in our full sample too, see Figure 2).

6.3. Accuracy

The composition of the RPDF is generated during the simulation, therefore it is known per se. Hence, by applying a Gaussian fit to the RPDF, such as the one described in Section 4.5, we can obtain the reliability of the fit in a particular case with the relative error,

$$e = \frac{f_m - f_k}{f_k}, \quad (3)$$

where f_k stands for the known compositional fraction of a certain type in the RPDF, and f_m for the fraction measured through the Gaussian fit. Then we can consider all of the instances of a fixed k in the 10^7 runs with

$$\epsilon = \bar{e}, \quad (4)$$

and the spread of Equation (4) is measured with

$$\sigma = \sqrt{e^2 - \bar{e}^2}. \quad (5)$$

Equations (3)–(5) are identical for the three complexes and the Q-type.

As a general trend, ϵ was larger for the C-complex than for the S one. This suggests that if objects of the X-complex and Q-type are present in the data sample, it is more likely for them to be identified as members of the C-complex than the S-complex by performing a Gaussian fit. This was also observed in test runs where only the main type of each complex was used. In terms of the $r-i$ index, the Q-type is closer to the C-complex, while the X-complex is closer to the S (see Figure 1). It is possible that this behavior is due to the relative width of the C- and S-complexes and not to the position of the X-complex itself.

The errors reported in Table 3 were obtained by taking the standard deviation of each complex/type from the set of 12 best matches from the MC simulation described in previous subsection.

The Gaussian fit is not as robust as the MC analysis for obtaining the results, and therefore we can expect lower accuracy. Having a fit centered on the C and S taxonomic components, the ratio of the area under the corresponding Gaussians is directly related to the compositional fraction of the sample. The fraction of S-type elements obtained through a Gaussian fit is more reliable than the C-type one. For this

¹³ We used Equations (3)–(5) presented in Section 6.3 to compare the results.

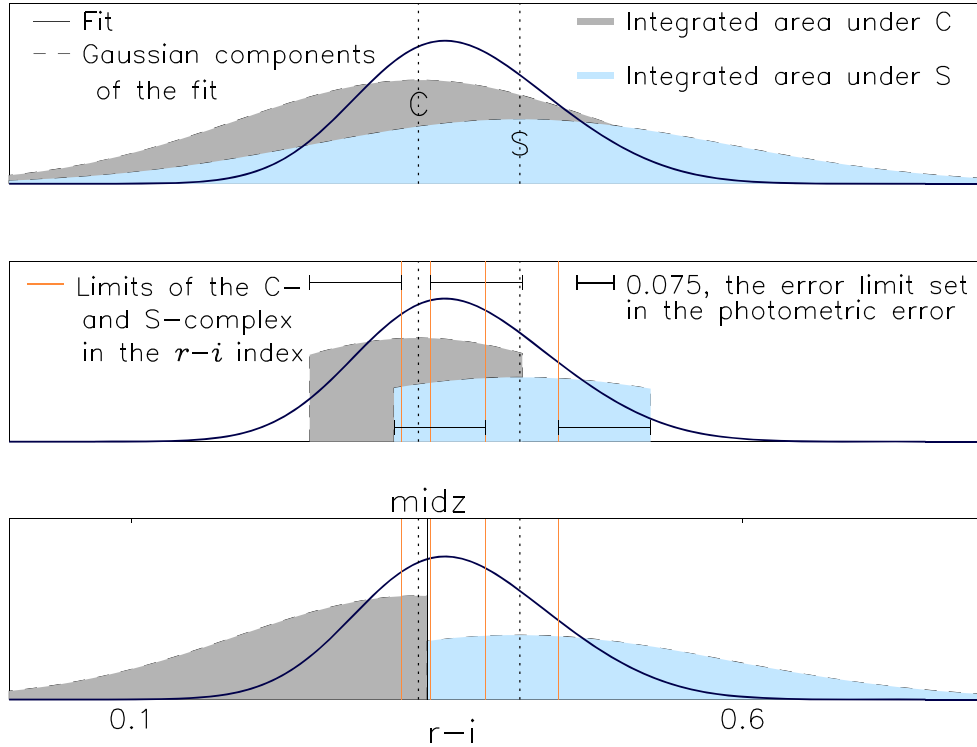


Figure 9. Integration limits considered for the Gaussian components of the fit. The fit is equivalent to the one showed in Figure 8. Vertical dotted shows the position of the main subtype of the C= and S-complex, thus the center of the Gaussian components. The width of the Gaussians is related to the error of the individual elements, and the ordinate axis has no practical meaning. See the text for more details.

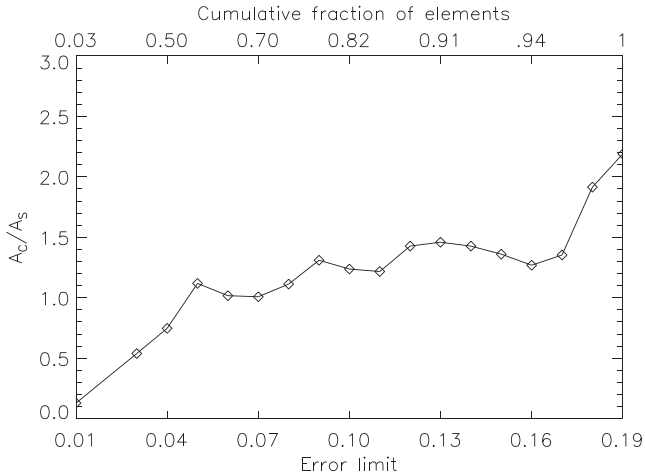


Figure 10. C-type to S-type ratio found with a Gaussian fit to the PDF after using different upper error selection criteria. Notice that this figure is a comparison of different error limits for our sample and it does not represent our main results.

reason, from the fit we focus on the S-type fraction obtained: 48%, which within the error bars is compatible with our MC result.

Although in our simulations we allowed for a wide range of variation in the randomly generated sample, our results partially rely on the assumptions described in Section 4.6.

7. Conclusions and Future Outlook

With the use of spectrophotometry on a 1.5 m robotic telescope, we performed rapid-response observations of small NEOs. Here we present the results from our optical sample. Measurements were simultaneously made in the r and i band. After applying selection criteria, our sample consisted on 131 observations of 82 different NEOs within the size range of ~ 30 –850 m.

For the size range considered, we found that the occurrence of a C-type asteroid is as frequent as one of an S-type, finding $C/S = 1.06$. Together, these two asteroid types represent $\sim 90\%$ of our sample, with the rest likely to be Q- and X-type asteroids. This compositional fraction is in agreement with the results of our previous publications (Mommert et al. 2016; Erasmus et al. 2017), which are based on UKIRT and KMTNet-SAAO observations.




Observations from our program are ongoing. The facility used in this study is now observing with the Z , Y , J , and H near-infrared bands in addition to the optical r and i . By analyzing the data set presented here, we created the tools to analyze the observations from the rest of the campaign (2016–present). Future publications from this study will include observations from multiple photometric bands, which will improve the accuracy of the results.

We would like to thank Carlos Román for his help on scheduling RATIR’s observations. We thank the anonymous referee for the valuable comments on this work. S.N.M. wants to dedicate this paper to coauthor, professor, and friend Bárbara Pichardo, RIP.

The data used in this paper were totally or partially acquired using the RATIR instrument, funded by the University of

California (UC) and NASA Goddard Space Flight Center (GSFC), on the 1.5 m telescope at Observatorio Astronómico Nacional, San Pedro Martir, operated and maintained by OAN-SPM and IA-UNAM. This project was supported in part by the National Aeronautics and Space Administration under the grant No. NNX15AE90G issued through the SSO Near Earth Object Observations Program. S.N.M. and M.R.R. also acknowledge the grant UNAM- DGAPA PAPIIT IN107316.

ORCID iDs

M. Mommert  <https://orcid.org/0000-0002-8132-778X>
 D. E. Trilling  <https://orcid.org/0000-0003-4580-3790>
 N. Butler  <https://orcid.org/0000-0002-9110-6673>
 B. Pichardo  <https://orcid.org/0000-0002-8195-8493>
 T. Axelrod  <https://orcid.org/0000-0002-5722-7199>
 R. Jedicke  <https://orcid.org/0000-0001-7830-028X>
 N. Moskovitz  <https://orcid.org/0000-0001-6765-6336>

References

- Becerra, R. L., Watson, A. M., Lee, W. H., et al. 2017, *ApJ*, **837**, 116
 Binzel, R. P., DeMeo, F. E., Bus, S. J., et al. 2019, *Icar*, **324**, 41
 Binzel, R. P., Reddy, V., & Dunn, T. L. 2015, in *Asteroids IV*, ed. P. Michel, F. E. DeMeo, & W. F. Bottke (Tucson, AZ: Univ. Arizona Press), 243
 Brown, P. G., Assink, J. D., Astiz, L., et al. 2013, *Natur*, **503**, 238
 Butler, N., Klein, C., Fox, O., et al. 2012, *Proc. SPIE*, **8446**, 844610
 Butler, N., Watson, A. M., Kutyrev, A., et al. 2017a, *GCN*, **21915**, 1
 Butler, N., Watson, A. M., Kutyrev, A., et al. 2017b, *GCN*, **22061**, 1
 Butler, N., Watson, A. M., Kutyrev, A., et al. 2017c, *GCN*, **22182**, 1
 Carry, B., Solano, E., Eggl, S., & DeMeo, F. E. 2016, *Icar*, **268**, 340
 Carvano, J. M., Hasselmann, P. H., Lazzaro, D., & Mothé-Diniz, T. 2010, *A&A*, **510**, A43
 Delsemme, A. H. 1991, *ASSL*, **1**, 377
 DeMeo, F. E., Binzel, R. P., Slivan, S. M., & Bus, S. J. 2009, *Icar*, **202**, 160
 Erasmus, N., Mommert, M., Trilling, D. E., et al. 2017, *AJ*, **154**, 162
 Galache, J. L., Beeson, C. L., McLeod, K. K., & Elvis, M. 2015, *P&SS*, **111**, 155
 García-Díaz, M. T., González-Buitrago, D., López, J. A., et al. 2014, *AJ*, **148**, 57
 Giorgini, J. D., Yeomans, D. K., Chamberlin, A. B., et al. 1997, *BAAS*, **29**, 1099
 Hinkle, M. L., Moskovitz, N., Trilling, D., et al. 2015, *AAS/DPS Meeting Abstracts*, **47**, 301.04
 Ieva, S., Dotto, E., Epifani, E. M., et al. 2018, *A&A*, **615**, A127
 Ivezić, Ž., Tabachnik, S., Rafikov, R., et al. 2001, *AJ*, **122**, 2749
 Lin, C.-H., Ip, W.-H., Lin, Z.-Y., et al. 2018, *P&SS*, **152**, 116
 Littlejohns, O. M., Butler, N. R., Cucchiara, A., et al. 2015, *MNRAS*, **449**, 2919
 Malhotra, R. 1997, *BAAS*, **28**, 1102
 Mommert, M., Trilling, D. E., Borth, D., et al. 2016, *AJ*, **151**, 98
 Moskovitz, N., Thirouin, A., Binzel, R., et al. 2015, *IAUGA*, **22**, 2255616
 Perna, D., Barucci, M. A., Fulchignoni, M., et al. 2018, *P&SS*, **157**, 82
 Popescu, M., Perna, D., Barucci, M. A., et al. 2018, *MNRAS*, **477**, 2786
 Ricci, D., Ramón-Fox, F. G., Ayala-Loera, C., et al. 2015, *PASP*, **127**, 143
 Ryan, E. L., Mizuno, D. R., Shenoy, S. S., et al. 2015, *A&A*, **578**, A42
 Stuart, J. S., & Binzel, R. P. 2004, *Icar*, **170**, 295
 Tapia, M., Rodríguez, L. F., Tovmassian, G., et al. 2014, *RMxAA*, **50**, 127
 Taylor, J. R. 1997, *An Introduction to Error Analysis* (2nd ed.; Mill Valley, CA: Univ. Science Books), 176
 Thomas, C. A., Emery, J. P., Trilling, D. E., et al. 2014, *Icar*, **228**, 217
 Thomas, C. A., Trilling, D. E., Emery, J. P., et al. 2011, *AJ*, **142**, 85
 Warner, B. D., Harris, A. W., & Pravec, P. 2009, *Icar*, **202**, 134
 Watson, A. M., Richer, M. G., Bloom, J. S., et al. 2012, *Proc. SPIE*, **8444**, 84445L

5. Investigando la diversidad taxonómica en familias de asteroides utilizando ATLAS

Para este artículo se tomaron del archivo del Minor Planet Center las observaciones de 1612 asteroides realizadas por los telescopios de ATLAS entre 2015 y 2018.

Determinar si un objeto pertenece a una familia de asteroides no es una tarea trivial y depende de los elementos orbitales propios (Nesvorný et al., 2015, hace una discusión al respecto). Para determinar si los objetos de nuestra muestra son miembros de una familia de asteroides se utilizó un catálogo creado por Nesvorný (2015), quien basa su análisis en el método más utilizado para este propósito (Zappala et al., 1990).

Por medio del método Lomb-Scargle (Lomb, 1976; Scargle, 1982) se calculó el periodo de rotación de cada uno de los objetos estudiados. Este método es ampliamente usado para extraer el periodo de una serie de datos con un espaciado no uniforme. Solo fueron usadas las mediciones en el filtro o por tener una frecuencia mayor, sin embargo no se espera que esto introduzca ningún sesgo. Para obtener el color de un objeto dado se pusieron en fase las curvas de ambos filtros tomando en cuenta el periodo obtenido y se le aplicó un ajuste polinomial a la curva del filtro o . Para poder aplicar el mismo ajuste a la curva del filtro c es necesario aplicar un offset, dicho offset es por definición color del objeto.

Los objetos de esta muestra corresponden a familias de asteroides que han sido estudiadas previamente. A excepción de los miembros de la familia Vesta (con asteroides tipo V) se espera que la gran mayoría de los objetos sean de tipo C y S como es observado en el cinturón principal. Por esta razón nuestro análisis supone que toda la muestra está compuesta por objetos de tipo C y S. De esta manera se clasifica cada uno de los objetos utilizando el índice de color $c-o$ para los asteroides de estos tipos calculados a partir de los espectros promedio provistos por DeMeo et al. (2009). Para

tomar en cuenta el error en la medición, se utilizó un método similar al del primer artículo, generando clones de las observaciones por medio de una simulación Monte Carlo. Se generaron 10,000 clones de cada objeto con una distribución centrada en el valor medido y con un ancho equivalente al error en la medición. Posteriormente se clasificó cada uno de los clones de acuerdo a la distancia respectiva entre su posición en el eje $c-o$ y los índices de color de los tipos C y S. El promedio de las 10,000 clasificaciones determina la taxonomía para cada uno de los objetos de la muestra. 16 % de los objetos estudiados fueron clasificados por un estudio independiente (Warner et al., 2009), por lo que fue posible comparar los resultados. La clasificación de los objetos coincide en un 85 %, mientras que los periodos de rotación concuerdan en un 89 % si se considera una barra de error del 10 %.

Aún cuando las familias tienen típicamente la misma taxonomía, existen diferentes razones para que haya miembros de diferentes clasificaciones en una familia determinada (ver por ejemplo Cellino et al., 2001; Russell et al., 2012). Este trabajo identifica la diversidad taxonómica en las familias Vesta, Nysa-Polana y Flora. Al relacionar los elementos orbitales propios con dicha diversidad, se observa una posible dependencia, la cuál es consistente con algunos de los modelos de formación de dichas familias (ídem), pues uno de los modelos de formación de la familia Flora sugiere que un asteroide de tipo C colisionó con uno de tipo S. La alta proporción de objetos de tipo C encontrada en la familia Flora (principalmente de tipo S), y la dependencia de la misma en el tamaño de los objetos, sugiere un límite en el tamaño del cuerpo carbonáceo.

Parte de la metodología para clasificar los objetos está basada en el artículo anterior. El incorporar un mecanismo estadístico para considerar el error en las mediciones en un método de clasificación simple brindó solidez a los resultados. También contribuí con la escritura del artículo y discusión relacionada con trabajos anteriores.



Investigating Taxonomic Diversity within Asteroid Families through ATLAS Dual-band Photometry

N. Erasmus¹, S. Navarro-Meza^{2,3}, A. McNeill³, D. E. Trilling^{1,3}, A. A. Sickafoose^{1,4,5}, L. Denneau⁶, H. Flewelling⁶,
A. Heinze⁶, and J. L. Tonry⁶

¹ South African Astronomical Observatory, Cape Town, 7925, South Africa; nerasmus@sao.ac.za

² Instituto de Astronomía, Universidad Nacional Autónoma de México, Ensenada B.C. 22860, México

³ Department of Astronomy and Planetary Science, Northern Arizona University, Flagstaff, AZ 86001, USA

⁴ Department of Earth, Atmospheric, and Planetary Sciences, Massachusetts Institute of Technology, Cambridge, MA 02139-4307, USA

⁵ Planetary Science Institute, Tucson, AZ 85719-2395, USA

⁶ Institute for Astronomy, University of Hawaii, Honolulu, HI 9682, USA

Received 2019 July 24; revised 2019 November 13; accepted 2019 November 13; published 2020 February 20

Abstract

We present here the c – o colors for identified Flora, Vesta, Nysa–Polana, Themis, and Koronis family members within the historic data set (2015–2018) of the Asteroid Terrestrial-impact Last Alert System (ATLAS). The Themis and Koronis families are known to be relatively pure C- and S-type Bus-DeMeo taxonomic families, respectively, and the extracted color data from the ATLAS broadband c - and o -filters of these two families are used to demonstrate that the ATLAS c – o color is a sufficient parameter to distinguish between the C- and S-type taxonomies. The Vesta and Nysa–Polana families are known to display a mixture of taxonomies possibly due to Vesta’s differentiated parent body origin and Nysa–Polana actually consisting of two nested families with differing taxonomies. Our data show that the Flora family also displays a large degree of taxonomic mixing and the data reveal a substantial H -magnitude dependence on color. We propose and exclude several interpretations for the observed taxonomic mix. Additionally, we extract rotation periods of all of the targets reported here and find good agreement with targets that have previously reported periods.

Unified Astronomy Thesaurus concepts: Main belt asteroids (2036); Asteroids (72); Broad band photometry (184); Sky surveys (1464); Minor planets (1065); Small solar system bodies (1469); Lomb-Scargle periodogram (1959); Period determination (1211); Light curves (918)

Supporting material: figure set, machine-readable table

1. Introduction

Asteroid families are groups of objects where members of the group display similar proper orbital elements. This suggests a common collisionally disrupted parent-body source for a family. Since the identification of asteroid families (Hirayama 1918), several studies have also shown that for many of the identified families there is also a strong correlation between taxonomic type and family membership (Bus 1999). For instance, family members of the Massalia, Eunomia, and Koronis families all have observed spectra or colors that are consistent with the Bus-DeMeo S-type taxonomy (Lazzaro et al. 1999; Masiero et al. 2015; Erasmus et al. 2019). On the other hand, members of the Hygiea, Adeona, and Themis families all have observed spectra or colors that are consistent with the Bus-DeMeo C-type taxonomy (Carruba 2013; Masiero et al. 2015; Erasmus et al. 2019). This leads to the assumption that the individual parent-body sources of each of these families must have had a pure composition with either a S-type or C-type spectral signature (see Figure 1 for spectra in the visible of the Bus-DeMeo S- and C-type taxonomies).

However, there are several families that display a large variation in observed spectra or color and therefore potentially contain a significant mix of two (or more) taxonomies. Some explanations that have been proposed include: nested families, i.e., two overlapping families in orbital space that are actually two separate families with differing taxonomies (Cellino et al. 2001); two colliding parents that had completely different mineralogy; size-dependent space-weathering that modifies the spectral shape of a subgroup within the family (Brunetto & Strazzulla 2005); a large differentiated parent body having variations in mineralogy

(Binzel & Xu 1993); or simply incorrectly assigning membership (sometimes referred to as interlopers).

In this work we present the c – o colors and rotation periods of 1612 (414 Vesta, 494 Flora, 304 Nysa–Polana, 204 Themis, and 197 Koronis) main-belt targets. In Sections 2 and 3 we briefly summarize the Asteroid Terrestrial-impact Last Alert System (ATLAS) system and the approach for identifying the relevant family members within its data set. In Section 4 we explain how the colors are derived from the data set’s dual-band photometry. The method for extracting color relies on the determination of the rotation periods, hence the latter are a convenient byproduct of our analysis. In Section 5 we discuss how we assign taxonomies to the targets. Section 6 contains results of validation tests using previously reported taxonomies and rotation periods. We also show validation results using the ATLAS c – o colors of the Themis and Koronis targets that have known and relatively pure taxonomic distributions. In Sections 7 and 8 we perform a more in-depth study on the observed taxonomic diversity of the Vesta, Nysa–Polana, and Flora families and use this to draw conclusions on the origin of the Flora family by comparing to the Vesta and Nysa–Polana families that have known reasons for the observed mixture in the taxonomies present.

2. ATLAS Data

Observations were performed between 2015 and 2018 by ATLAS.⁷ Currently consisting of two units both located in Hawaii, ATLAS is designed to achieve a high survey speed per

⁷ <http://atlas.fallingstar.com>

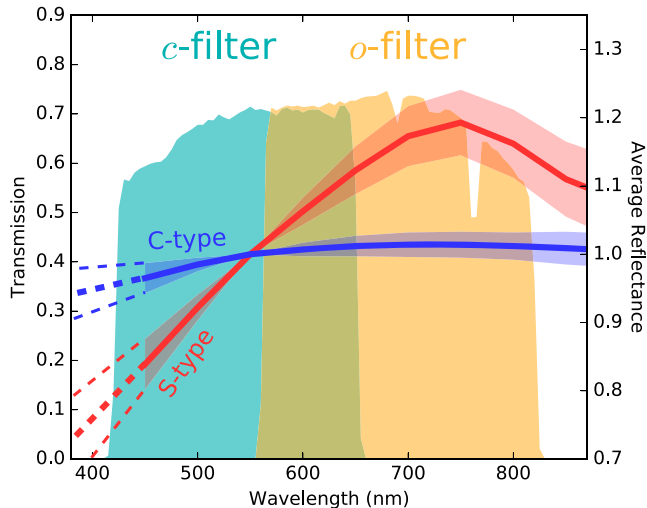


Figure 1. Transmission curves of the *c*- and *o*-filters of ATLAS (Tonry et al. 2018a) are plotted together with the averaged visible wavelength reflectance spectra, normalized at 550 nm, of the Bus-DeMeo S- and C-type taxonomies (DeMeo et al. 2009). The upper and lower bounds of the two taxonomic spectra provided by DeMeo et al. (2009) are also indicated with shading. The dashed lines are linear interpolations of the spectra and bounds since no data below 450 nm are provided.

unit cost (Tonry et al. 2018a). Its main purpose is to discover asteroids with imminent impacts with Earth that are either regionally or globally threatening in nature. To fulfill this, the two current ATLAS units scan the complete visible northern sky every night enabling it to make numerous discoveries in multiple astronomical disciplines, such as supernovae candidate discovery (Prentice et al. 2018), gamma-ray burst phenomena (Stalder et al. 2017), variable stars (Heinze et al. 2018), and asteroid discovery. Since its inception ATLAS has found 39 potentially hazardous asteroids among the 370 near-Earth asteroids that it has discovered. All detected asteroid astrometry and photometry are posted to the Minor Planet Center, while the supernova candidates are publicly reported to the International Astronomical Union Transient Name Server.

The two ATLAS units are 0.5 m telescopes each covering 30 deg² field-of-view in a single exposure. The main survey mode mostly utilizes two custom filters, a “cyan” or *c*-filter with a bandpass between 420 and 650 nm and an “orange” or *o*-filter with a bandpass between 560 and 820 nm (see Figure 1). For further details on ATLAS, ATLAS photometry, and the ATLAS All-sky Stellar Reference Catalog see Tonry et al. (2018a, 2018b) and Heinze et al. (2018).

3. Family Determination

To identify Flora, Vesta, Nysa–Polana, Themis, and Koronis family members within the ATLAS data set we utilize and cross-correlate with data from Nesvorný (2015) obtained through The Planetary Data System⁸ (PDS) to associate objects from the ATLAS data set with known collisional families. The Nesvorný (2015) data set makes use of the Hierarchical Clustering Method (Zappala et al. 1990) to assign families. The data set also supplies a “*c*-parameter” (see Nesvorný 2015 for a description) that can be used to identify suspected interlopers. For the ATLAS data set the interloper contamination is low with a percentage of suspected interlopers for the Flora, Vesta,

Nysa–Polana, Themis, and Koronis of 4.5%, 0.0%, 13.5%, 6.4%, and 5.6% respectively.

4. Rotation Period Extraction and Color Calculation

Rotation periods were extracted from the ATLAS data by generating a Lomb–Scargle periodogram (Lomb 1976; Scargle 1982) of each target’s *o*-filter photometric data since this is the most abundant data out of the two filters used by ATLAS. We only considered ATLAS targets that had at least 30 photometric data points in the *o*-filter and 10 photometric data points in the *c*-filter. See the top plots of Figure 2 for example *o*- and *c*-filter photometric data of Flora family member 1785 Wurm (1941 CD), Koronis family member 1809 Prometheus (2522 P-L), and Vesta family member 2511 Patterson (1980 LM). Targets that had periodograms containing peaks with a confidence (Zechmeister & Kürster 2009) larger than 50% were flagged to have potentially extractable rotation periods. See the middle plots of Figure 2 for example periodograms that resulted in high confidence peaks. The final extracted light-curve period is determined from the strongest periodogram peak, and the uncertainty of this periodicity is determined by fitting a Gaussian function to the periodogram peak and using the rms width (σ) as the uncertainty (see the superimposed black curve and σ of the fitted function in the periodogram plots in Figure 2). It has to be noted that because of the ATLAS observing cadence there is significant alias ambiguity in our periodograms due to the daily interval between observations. Therefore, there is the likelihood that some of the periods we extract are offset from the actual period by a frequency that is a multiple of a day (24 hr). This is evident by the presence of multiple peaks in some of our periodograms that have a similar confidence. The rotation periods (twice the extracted light-curve period), uncertainty, and confidence in the periods are recorded in Table 1.

To determine the colors of each ATLAS target we fold both the *c*- and *o*-filter data with the extracted rotation period. A spline fit in the form of a high-order polynomial is fitted to the more abundant *o*-filter data with the fit weighted on the uncertainty of the photometric values. The same polynomial that is fitted to the *o*-filter data, with the inclusion of a magnitude offset as a variable fit parameter, is fitted to the *c*-filter data. The *c*–*o* color is assigned as this fitted magnitude offset. The uncertainty in this color value is derived from the weighted (by uncertainty of the photometric values) standard deviation of the residuals of the two filter fits and the respective filter data. See the bottom plots of Figure 2 for examples of the results of this procedure with the *c*–*o* color values and uncertainty displayed in bottom left corner of each plot. This derived color value is not dramatically affected if by chance the folding is performed using an alias of the rotation period instead of the actual rotation period.

In a final step we remove photometric outliers and low-quality data from our data set by discarding targets that have a *c*–*o* color that falls more than 3σ from the median measured *c*–*o* color of the relevant family and targets that had an uncertainty in measured *c*–*o* color larger than 130% of the median uncertainty of the targets in the relevant family. The result was that we discarded on average roughly 25% of our targets for each family. The calculated *c*–*o* colors and the uncertainties are recorded in Table 1.

⁸ <https://pds.nasa.gov/>

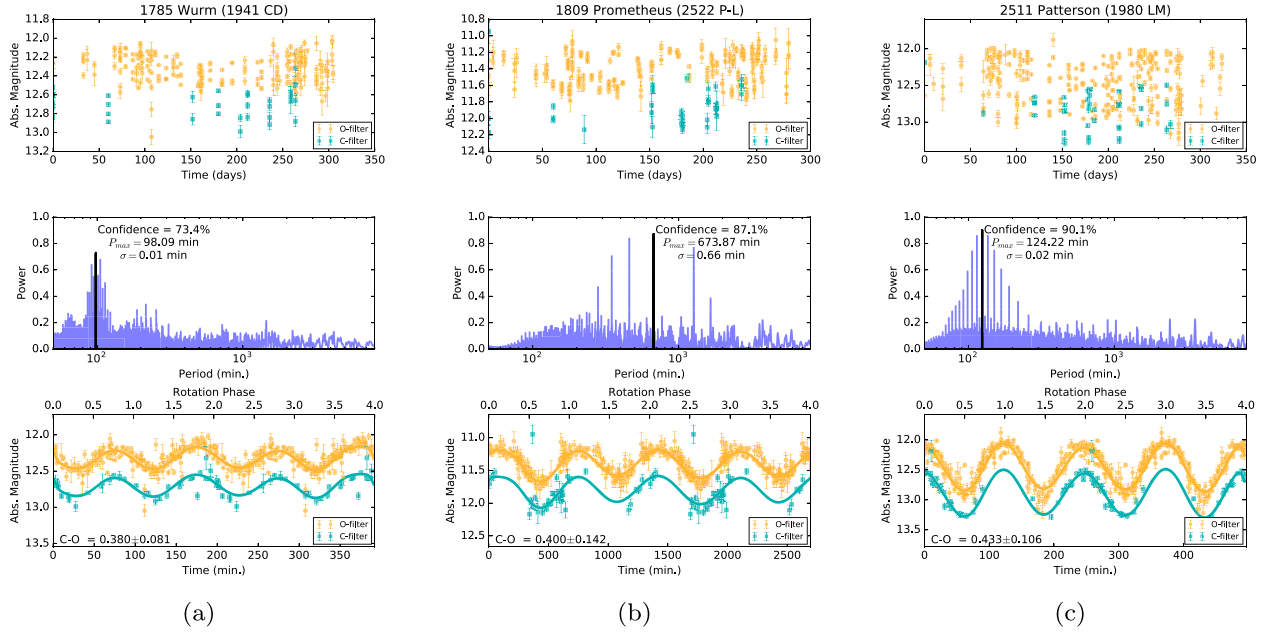


Figure 2. Example ATLAS photometric data (top plots), Lomb-Scargle periodograms of photometric data (middle plots), and phased photometric data (bottom plots) for (a) Flora family member 1785 Wurm (1941 CD), (b) Koronis family member 1809 Prometheus (2522 P-L), and (c) Vesta family member 2511 Patterson (1980 LM). For the periodograms we also indicate the extracted light-curve period ($P_{\max} = \frac{\text{Rot.Period}}{2}$), uncertainty in extracted period (σ), and confidence in extracted period. Fitted to the phased data are spline fits in the form of a high-order polynomial which are used to determine the color of each target (see Section 4 for detail). The determined $c-o$ color value and the uncertainty is displayed in the bottom-left of each plot. All 1612 images are available in the Figure Set. (The complete figure set (1612 images) is available.)

Table 1
ATLAS Colors, Extracted Rotation Periods, and Taxonomic Probabilities

No.	Target Name	Family	H^a (mag)	$c-o$ (mag)	Rotation Period (hr)	Confidence %	C-type (prob. in %)	S-type
0001	158 Koronis	Koronis	9.3	0.40 ± 0.09	14.204 ± 0.006	73	18	82
0002	167 Urda	Koronis	9.2	0.38 ± 0.06	13.060 ± 0.009	88	14	86
0003	208 Lacrimosa	Koronis	9.0	0.42 ± 0.09	14.087 ± 0.010	84	13	87
0004	222 Lucia	Themis	9.1	0.22 ± 0.09	9.371 ± 0.005	58	86	14
0005	243 Ida	Koronis	9.9	0.39 ± 0.10	4.225 ± 0.001	74	26	74
0006	254 Augusta	Flora	12.1	0.42 ± 0.12	5.895 ± 0.002	85	18	82
0007	263 Dresda	Koronis	10.2	0.39 ± 0.12	12.450 ± 0.055	72	28	72
0008	277 Elvira	Koronis	9.8	0.41 ± 0.04	29.676 ± 0.046	86	1	99
0009	281 Lucretia	Flora	12.0	0.44 ± 0.13	4.783 ± 0.001	70	17	83
0010	352 Gisela (A893 AB)	Flora	10.0	0.43 ± 0.09	7.480 ± 0.003	82	10	90

Note.

^a H magnitude was obtained from <https://ssd.jpl.nasa.gov/horizons.cgi>.

(This table is available in its entirety in machine-readable form.)

5. Taxonomic Determination

For this study we limit our target classification to the two most prominent Bus-DeMeo taxonomic classes, namely, the silicate-rich S-type and the carbonaceous C-type that make up roughly 50% and 35% of the main-belt population, respectively (Bus & Binzel 2002; DeMeo & Carry 2014; Erasmus et al. 2018). Because the Bus-DeMeo S- and V-type spectra are difficult to distinguish using only two broadband filters in the visible region we consider those two both as S-type in this study. To decide which of these two classifications is the most likely for each of our targets we calculate the expected $c-o$ ATLAS color for the mean Bus-DeMeo S- and C-type spectra provided by DeMeo et al. (2009) and compare that to the

target’s measured $c-o$ color. The expected $c-o$ color is determined by convolving the ATLAS filter responses with the mean Bus-DeMeo S- and C-type spectra (see Figure 1 for filter responses and spectra) and use the convolution of the ATLAS filter responses with the Sun’s spectrum as the zero-point magnitudes. The same was done for the the upper and lower bounds of the spectra to determine the uncertainty in the expected color. The expected $c-o$ color for an S-type asteroid is $0.388^{+0.011}_{-0.012}$ and for a C-type is $0.249^{+0.004}_{-0.004}$ (see the solid blue and red vertical lines in Figures 3–5 with the upper and lower bounds indicated in the dashed lines).

To assign the S- or C-type taxonomy to each of our targets we use a probabilistic approach using a Monte Carlo method where we generate 10,000 pseudo-measured colors with a

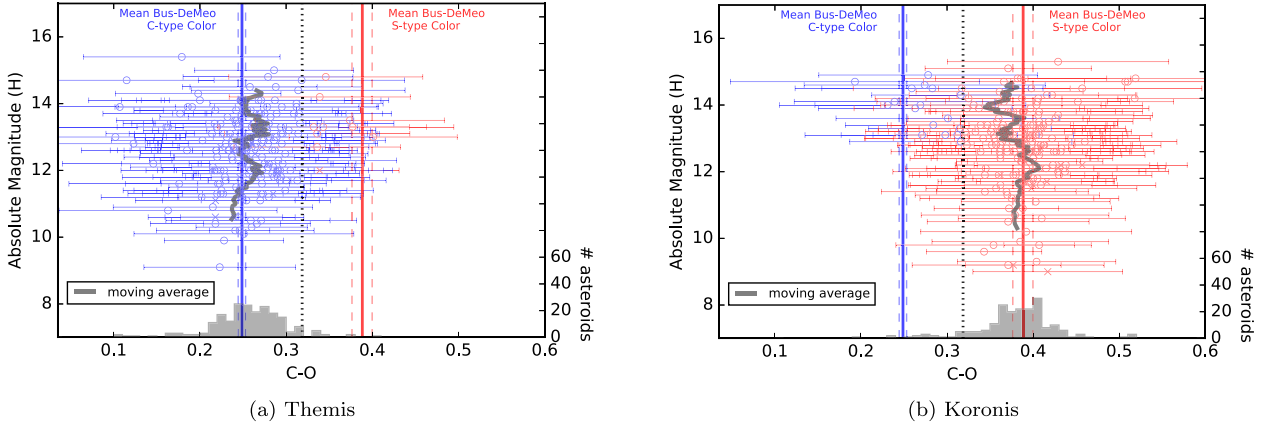


Figure 3. Plotted are the $c-o$ colors that could be extracted (see Section 4) from the ATLAS data set of (a) Themis family members and (b) Koronis family members. The data points are colored depending on the final assigned taxonomy (see Section 5, S-type = red and C-type = blue). The Themis and Koronis families are two known C- and S-type Bus-DeMeo taxonomic families, respectively, and the color histograms centered at the relevant mean Bus-DeMeo color therefore illustrate that the ATLAS $c-o$ color is a suitable parameter to distinguish between the C- and S-type taxonomies.

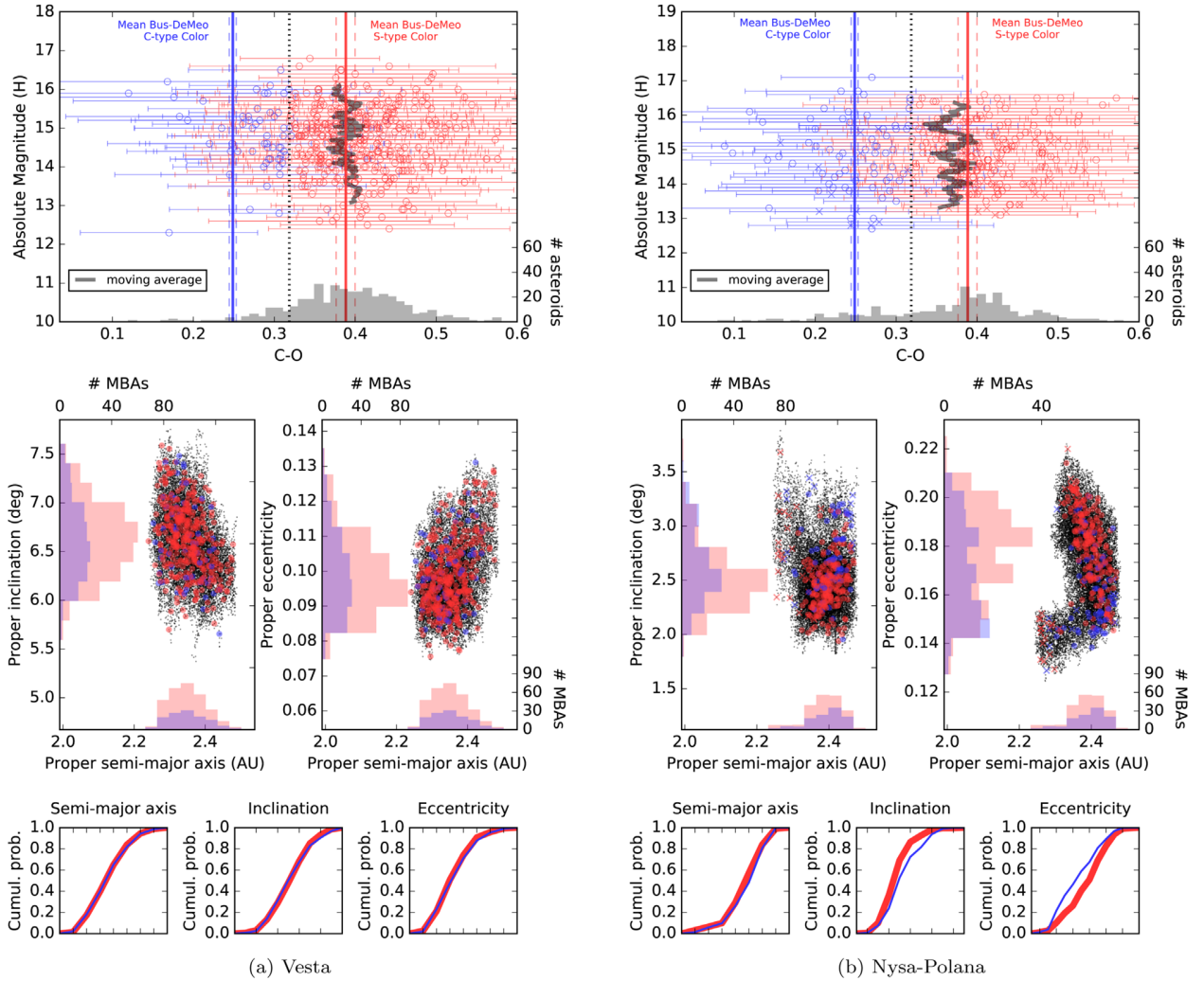


Figure 4. (Top) Plotted are the $c-o$ colors that could be extracted (see Section 4) from the ATLAS data set of (a) Vesta family members and (b) Nysa–Polana family members. The data points are colored depending on the final assigned taxonomy (see Section 5, S-type = red and C-type = blue). (Middle) Proper orbital elements of all ATLAS targets with all known family members from Nesvorný (2015) plotted as small black data points in the background (suspected interlopers plotted with a cross symbol). Also included are the histograms of the taxonomic probabilities (see Section 5) indicating the taxonomic dependence on orbital parameters. (Bottom) The cumulative probabilities of the two taxonomies with respect to the three orbital parameters: broad red line = S-type and narrow blue line = C-type (see Section 7).

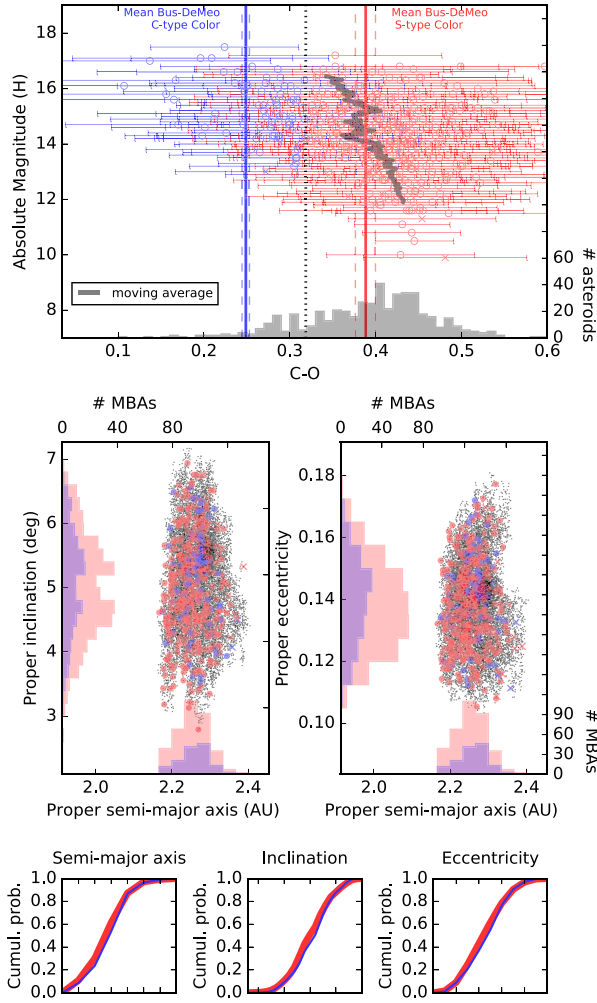


Figure 5. (Top) Plotted are the $c-o$ colors that could be extracted (see Section 4) from the ATLAS data set of Flora family members. The data points are colored depending on the final assigned taxonomy (see Section 5, S-type = red and C-type = blue). (Middle) Proper orbital elements of all ATLAS targets with all known family members from Nesvorný (2015) plotted as small black data points in the background (suspected interlopers plotted with a cross symbol). Also included are the histograms of the taxonomic probabilities (see Section 5) indicating the taxonomic dependence on orbital parameters. (Bottom) The cumulative probabilities of the two taxonomies with respect to the three orbital parameters: broad red line = S-type and narrow blue line = C-type (see Section 7)

normal distribution centered on the target’s measured color and the width of the distribution equal to the uncertainty in the measured color (see Navarro-Meza et al. 2019 for a similar approach using $r-i$ colors to classify near-Earth asteroids). Each pseudo-measured color is classified as either S- or C-type depending on where it lies relative to the decision line located at the color value midway between the two expected $c-o$ color values for an S- and C-type asteroid (i.e., $c-o = 0.319$; see the dotted black vertical line in Figures 3–5). The pseudo-measured classifications are tallied to give the S- and C-type taxonomic probabilities for each target. The taxonomy with the highest probability is assigned to the target (data points in Figures 3–5 are color-coded depending on the final assigned taxonomy, S-type = red and C-type = blue). We use the probabilities instead of the discrete classification for all our analyses in Sections 7 and 8. The taxonomic probabilities for each target are recorded in Table 1.

6. Validation of Rotation Periods and Taxonomic Determination

To validate our procedures of extracting rotation periods and determining taxonomic types, we cross-reference our results with The Asteroid Light Curve Database (LCDB; Warner et al. 2009, Updated 2019 January 31)⁹ and find that $\sim 10\%$ of our targets are also present in the LCDB. For the 262 targets present in both data sets we derive the same taxonomy as that reported in the LCDB for 85% of the targets (for this we consider V-type and S-type as a match as well as B-type and C-type as a match) and also match the reported rotation periods within an error margin of 1% for 76% of our targets and within an error margin of 10% for 89% of our targets (for this comparison we also included the two alias periods adjacent to the main extracted period).

As a second validation test, the Themis and Koronis families, which are two well-known relatively pure C- and S-type Bus-DeMeo taxonomic families, are used as benchmarks for our taxonomic determination. In Figure 3 we plot the extracted $c-o$ colors of the Themis and Koronis family members within the ATLAS data set. The data points are color-coded depending on the final assigned taxonomy, S-type = red and C-type = blue. Of the 204 Themis targets we classify 95% as C-type, and the color histogram shown in Figure 3(a) shows a clear peak centered at the expected mean Bus-DeMeo C-type color. Of the 197 Koronis targets we classify 91% as S-type, and the color histogram shown in Figure 3(b) shows a clear peak centered at the expected mean Bus-DeMeo S-type color. These two plots demonstrate that the ATLAS $c-o$ colors that we extract are a sufficient parameter to distinguish between the C- and S-type taxonomies.

7. Mixture of Taxonomies in the Vesta and Nysa–Polana Families

The Vesta family, a V-type family, has a spectral signature similar to the spectral shape of S-type asteroids but with the distinct S-type absorption feature at $1 \mu\text{m}$ enhanced in V-types. The Nysa–Polana family is also a known S-type family. However, observations have indicated that both contain a significant number of family members with spectra or color different from the majority of family members (Erasmus et al. 2019). This could be ascribed to the parent body of the Vesta family originally consisting of a differentiated object (Russell et al. 2012) and hence a plausible reason behind the range in colors observed within the Vesta family. Through albedo studies the Nysa–Polana family has been identified to consist of two subgroups overlapping in proper orbital space (Cellino et al. 2001), i.e., two nested families of which one shows S-type spectral characteristics and the other B-type spectral characteristics. The Bus-DeMeo B-type spectrum is similar to the spectral shape of C-type asteroids, flat and featureless, but with a slightly bluer slope in the visible. The top set of plots in Figure 4 are the extracted $c-o$ colors of the Vesta and Nysa–Polana family members within the ATLAS data set. The two-taxonomic mix is clearly evident in both families with only $\sim 70\%$ of Vesta targets having $c-o$ colors in the vicinity of the expected S(V)-type color while the Nysa–Polana targets have a 1:3 split between $c-o$ colors that match the expected C(B)-type and S-type colors, respectively.

⁹ <http://www.MinorPlanet.info/lightcurvedatabase.html>

By plotting the distributions of the two taxonomies as a function of proper orbital space (see the middle set of plots in Figure 4), the differing causes behind the taxonomic diversity seen in both of these families can be distinguished from one another. The assigned taxonomy of Vesta family members has no dependence on proper orbital space (consistent with a differentiated parent body origin), while the Nysa–Polana “B-type subgroup” is positioned at a lower eccentricity (and to a lesser extent a higher inclination) than the Nysa–Polana “S-type subgroup” (consistent with two nested families with slightly differing orbital parameters). This taxonomic dependence (or independence) on orbital parameters is highlighted by performing Kolmogorov–Smirnov (K-S) tests and plotting the resultant cumulative probabilities of the two taxonomies with respect to the three orbital parameters (see the bottom plots of Figure 4, broad red line = S-type and narrow blue line = C-type). The two taxonomies in the Vesta family have identical cumulative probabilities for the three orbital parameters (K-S statistics for semimajor axis, inclination, and eccentricity of 0.08, 0.04, and 0.01), while the two taxonomies in the Nysa–Polana family have obvious differing cumulative probabilities in eccentricity (K-S statistics for semimajor axis, inclination, and eccentricity of 0.05, 0.12, and 0.15). We use the cumulative probabilities of these two families as benchmarks for ascertaining the likely cause of the taxonomic diversity also seen in the Flora family.

8. Taxonomic Diversity of the Flora Family

The top plot in Figure 5 shows the the extracted c – o colors of the Flora family members within the ATLAS data set. As is the case with the Vesta and Nysa–Polana families, the Flora family also displays a significant taxonomic mix, or at least a significant range of colors. Roughly 70% of the targets have c – o colors consistent with the expected S-type color with the remaining targets displaying bluer C-like colors. This is a similar proportion to that of the Vesta family. The cumulative plots of the two colors in the Flora family (see the bottom of Figure 5) are identical for the three orbital parameters (as is the case for the Vesta family) as opposed to indicating a nested family as is the case for the Nysa–Polana family. Therefore, a nested family is unlikely as the source of the taxonomic mix in the Flora family.

9. Discussion

There are several possible interpretations for the taxonomic mix observed for the Flora family. Plotting the moving average of the colors as a function of H -magnitude (size) reveals a strong color dependence on size for the Flora family targets (see Figure 5). Since the smaller bodies are probably younger (more recently created through collisions) and therefore have fresher surfaces, one clear possibility is that the older surfaces on the larger bodies have been reddened through space weathering, whereas the younger surfaces on smaller bodies are unweathered and therefore less red. Thomas et al. (2011, 2012) report that small ($H \approx 15$) Koronis family objects are bluer than large ($H \approx 12$) Koronis family objects and attribute this difference to space weathering. We also observe a hint of this effect at a similar H -magnitude range in our Koronis family observations (see Figure 3(b)). However, this effect is subtle and cannot explain the large color range we observe for the Flora family (compare color ranges as a

function of H -magnitude for the Koronis and Flora families in Figures 3(b) and 5)

Another possibility is that, like the Vesta family, the heterogeneous Flora family may show evidence of a differentiated parent body. This is in agreement with a differentiated-body speculation by Gaffey (1984) based on several mineralogic and petrologic parameters derived for the surface material of asteroid Flora. Spectral data from the Galileo spacecraft on its flyby of Flora-family member 951 Gaspra also showed an olivine/pyroxene ratio that points to Gaspra being a fragment of at least a partially differentiated parent body (Veverka et al. 1994). However, various work (Vernazza et al. 2008, 2014; Dunn et al. 2013) has shown that the Flora family is likely the source of the undifferentiated LL chondrites, making this interpretation potentially problematic.

Alternatively, the C-like asteroids in the Flora family may simply be interlopers in the family membership list, though this would imply a relatively high contamination fraction of 28.3% that is significantly higher than the estimation for our data set of only 4.5% using the model of Nesvorný (2015).

Finally, two additional possible causes for the C-like colors that are observed could be due to shocked material and impact melt, which Kohout et al. (2014) and Reddy et al. (2014) have shown can make LL chondrite (S-like) spectra appear more C-like, or that a large member of the original S-type Flora family was simply impacted by a C-type asteroid that shattered, producing an embedded family within the Flora family that has a separate parent body (here we define an embedded family as one that was created through a collision between a family member and a non-family member, whereas a nested family occupies similar orbital element space but has an independent origin). Neither of these interpretations can be excluded by the taxonomic independence on orbital parameters we observe. The strong color dependence on size of our observed Flora family targets can be explained if the C-type impactor was smaller ($H \gtrsim 12$) than the original S-type Flora parent body.

These topics are discussed in further detail in a forthcoming paper (H. Sun et al. 2020, in preparation).

10. Conclusion

We have reported the c – o colors (and rotation periods) for identified Flora, Vesta, Nysa–Polana, Themis, and Koronis family members within the historic data set (2015–2018) of ATLAS. By using a probabilistic approach we also classify our targets as either S-type or C-type and compare to previously reported taxonomies and rotation periods to validate our methodologies. We use the Themis (a C-type family) and Koronis (a S-type family) targets in the ATLAS data set to demonstrate that the ATLAS c – o color is a sufficient parameter to distinguish between the C- and S-type taxonomies.


We find that the Flora family has a significant mixture of red (S-like) and blue (C-like) colors and a compelling observed H -magnitude dependence on the colors and we propose several possible causes of this range in colors.

This work has made use of data from the Asteroid Terrestrial-impact Last Alert System (ATLAS) project. ATLAS is primarily funded to search for near earth asteroids through NASA grants NN12AR55G, 80NSSC18K0284, and 80NSSC18K1575; byproducts of the NEO search include images and catalogs from the survey area. The ATLAS science products have been made possible through the contributions of the University of Hawaii

Institute for Astronomy, the Queen's University Belfast, the Space Telescope Science Institute, and the South African Astronomical Observatory.

This work is partially supported by the South African National Research Foundation (NRF), the Arizona Board of Regents' Regents Innovation Fund, the National Aeronautics and Space Administration (NASA), and by a grant from NASA's Office of the Chief Technologist.

ORCID iDs

N. Erasmus  <https://orcid.org/0000-0002-9986-3898>
 D. E. Trilling  <https://orcid.org/0000-0003-4580-3790>
 A. A. Sickafoose  <https://orcid.org/0000-0002-9468-7477>
 L. Denneau  <https://orcid.org/0000-0002-7034-148X>
 H. Flewelling  <https://orcid.org/0000-0002-1050-4056>
 A. Heinze  <https://orcid.org/0000-0003-3313-4921>
 J. L. Tonry  <https://orcid.org/0000-0003-2858-9657>

References

- Binzel, R. P., & Xu, S. 1993, *Sci*, **260**, 186
 Brunetto, R., & Strazzulla, G. 2005, *Icar*, **179**, 265
 Bus, S. 1999, PhD thesis, Massachusetts Inst. Tech.
 Bus, S. J., & Binzel, R. P. 2002, *Icar*, **158**, 146
 Carruba, V. 2013, *MNRAS*, **431**, 3557
 Cellino, A., Zappalà, V., Doressoundiram, A., et al. 2001, *Icar*, **152**, 225
 DeMeo, F. E., Binzel, R. P., Slivan, S. M., & Bus, S. J. 2009, *Icar*, **202**, 160
 DeMeo, F. E., & Carry, B. 2014, *Natur*, **505**, 629
 Dunn, T. L., Burbine, T. H., Bottke, W. F., & Clark, J. P. 2013, *Icar*, **222**, 273
 Erasmus, N., McNeill, A., & Mommert, M. 2018, *ApJS*, **237**, 19
 Erasmus, N., McNeill, A., & Mommert, M. 2019, *ApJS*, **242**, 15
 Gaffey, M. J. 1984, *Icar*, **60**, 83
 Heinze, A. N., Tonry, J. L., Denneau, L., et al. 2018, *AJ*, **156**, 241
 Hirayama, K. 1918, *AJ*, **31**, 185
 Kohout, T., Gritsevich, M., Grokhovsky, V. I., et al. 2014, *Icar*, **228**, 78
 Lazzaro, D., Mothé-Diniz, T., Carvano, J., et al. 1999, *Icar*, **142**, 445
 Lomb, N. R. 1976, *Ap&SS*, **39**, 447
 Masiero, J., DeMeo, F., Kasuga, T., & Parker, A. 2015, in Asteroid Family Physical Properties, ed. P. Michel, F. DeMeo, & W. Bottke (Tucson, AZ: Univ. Arizona Press), 323
 Navarro-Meza, S., Mommert, M., Trilling, D. E., et al. 2019, *AJ*, **157**, 190
 Nesvorný, D. 2015, *PDSS*, **234**, 1
 Prentice, S. J., Maguire, K., Smartt, S. J., et al. 2018, *ApJL*, **865**, L3
 Reddy, V., Sanchez, J. A., Bottke, W. F., et al. 2014, *Icar*, **237**, 116
 Russell, C. T., Raymond, C. A., Coradini, A., et al. 2012, *Sci*, **336**, 684
 Scargle, J. D. 1982, *ApJ*, **263**, 835
 Stalder, B., Tonry, J., Smartt, S. J., et al. 2017, *ApJ*, **850**, 149
 Thomas, C. A., Rivkin, A. S., Trilling, D. E., Enga, M.-t., & Grier, J. A. 2011, *Icar*, **212**, 158
 Thomas, C. A., Trilling, D. E., & Rivkin, A. S. 2012, *Icar*, **219**, 505
 Tonry, J. L., Denneau, L., Flewelling, H., et al. 2018b, *ApJ*, **867**, 105
 Tonry, J. L., Denneau, L., Heinze, A. N., et al. 2018a, *PASP*, **130**, 064505
 Vernazza, P., Binzel, R., Thomas, C., et al. 2008, *Natur*, **454**, 858
 Vernazza, P., Zanda, B., Binzel, R. P., et al. 2014, *ApJ*, **791**, 120
 Veverka, J., Belton, M., Klaasen, K., & Chapman, C. 1994, *Icar*, **107**, 2
 Warner, B. D., Harris, A. W., & Pravec, P. 2009, *Icar*, **202**, 134
 Zappala, V., Cellino, A., & Farinella, P. 1990, *AJ*, **100**, 2030
 Zechmeister, M., & Kürster, M. 2009, *A&A*, **584**, 577

6. Taxonomía de NEOs pequeños con RATIR -borrador-

En este artículo se analizan las observaciones realizadas por nuestro equipo con el instrumento RATIR de 2014 a 2018. Las mediciones de 2016 a 2018 incluyen información en bandas del rango óptico (r e i) y cercano infrarrojo (Z , Y , J y H), sin embargo la calidad de la medición en cada banda no es uniforme, porque ninguno de los objetos cuenta con mediciones en todas las bandas con calidad suficiente. Particularmente no fue posible utilizar mediciones en la banda H . Por lo anterior fue necesario utilizar diferentes modelos para analizar la muestra.

Considerando el color formado por dos filtros fotométricos arbitrarios, todos los objetos de cierta taxonomía tienen un color similar. En los dos artículos anteriores se demostró cómo un solo color puede ser de gran utilidad para estudiar la distribución taxonómica de una muestra de asteroides. Al contar con información de diferentes filtros, el objetivo es construir un método de análisis con la mayor cantidad de dimensiones (colores) posible para tener un resultado más exacto. Sin embargo el rango efectivo de nuestra muestra, así como de la muestra control no es uniforme en función de la longitud de onda, por lo que empleamos distintas combinaciones de filtros que tuviesen suficiente información en ambas muestras, y que el algoritmo de clasificación (resumido en el siguiente párrafo) ofreciera una exactitud confiable.

El análisis se centra en una técnica de Machine Learning conocida como k -NN (k -Nearest Neighbors). Este algoritmo identifica las zonas de cada clase en un espacio N -dimensional, en este caso las clases son las taxonomías de los asteroides y cada color una dimensión. Dado que todos los objetos de una misma taxonomía tienen colores similares, el algoritmo determina cuáles son los límites entre una taxonomía y otra en el espacio de colores. Se consideraron todas las taxonomías que cuentan con más de 5 espectros en la muestra control y que por lo tanto se espera que representen una

parte significativa de la muestra, esto incluye a los complejos taxonómicos C (formado por los tipos C, B y Ch), X (tipos X, Xn, Xk, Xe), S (tipos S, Sw, Sr, Srq, Sqw) Q (tipos Q y Sq) y los tipos D, V y L.

Para cada conjunto de filtros a utilizar, el algoritmo determina las zonas de cada taxonomía por medio de la muestra control, por lo que al introducir los objetos observados el algoritmo regresa su clasificación. Para tomar en cuenta el error en la observación se procedió de manera similar a los artículos anteriores, generando 1000 copias Monte Carlo de cada observación bajo una distribución gaussiana. Se encontró la clasificación para cada una de las copias y se determinó como cierta aquella con mayor peso estadístico. Basado en esto, presentaremos tablas con la probabilidad de cada objeto de pertenecer a las diferentes taxonomías.

87 objetos fueron tratados con *Machine Learning* y 151 con simulaciones Monte Carlo, con la metodología del primer artículo. Diferentes estudios acerca de la taxonomía de asteroides han considerado distintas taxonomías en su análisis, así como distintos rangos de tamaño, lo cuál afecta las proporciones reportadas por cada autor. Para comparar nuestros resultados con otros estudios decidimos utilizar el cociente entre objetos primitivos y evolucionados: $\frac{C+D+X}{A+K+L+O+Q+R+S+T+V}$. El análisis de resultados está en curso, sin embargo, los resultados preliminares concuerdan con los obtenidos en el trabajo más reciente de taxonomía de NEOs menores a 1 Km (Devogèle et al., 2019) y los del mayor estudio a la fecha del mismo tipo de objetos (Binzel et al., 2019). Por lo tanto -potencialmente-, al estudiar la distribución taxonómica, la combinación de mediciones fotométricas y herramientas de cómputo pueden ofrecer la misma calidad que la espectroscopía, pero de manera más eficiente.

Para este artículo seguí la metodología usada por uno de mis asesores en un trabajo similar con datos del telescopio UKIRT (Mommert et al., 2016), sin embargo yo escribí mis propios códigos. De manera similar al primer artículo, yo realicé la investigación asociada a este. Como trabajo

preliminar, escribí una rutina para organizar y limpiar los espectros de la muestra control. Esto incluyó eliminar mediciones repetidas o nulas, descartar los *Mars Crossers* y organizar cada espectro de acuerdo a la taxonomía reportada por el equipo de MITHNEOS (Binzel et al., 2019). Escribí una rutina adicional para recortar los espectros de la muestra control en los casos donde su cobertura no fuera suficiente en comparación con los filtros de RATIR. Esto para que la convolución no arrojara colores característicos falsos. Exploré el uso de *Principal Component Analysis* para encontrar los colores que brindan más información acerca de la clasificación de asteroides, no obstante decidí utilizar todos los colores con los que contaba en los casos donde fuera posible.

Taxonomy of Sub-kilometer NEOs from multiwavelength photometry with RATIR

S. NAVARRO-MEZA,^{1,2} M. MOMMERT,^{3,2} D.E. TRILLING,² N. BUTLER,^{4,5} AND M. REYES-RUIZ¹

¹*Instituto de Astronomia, Universidad Nacional Autónoma de México, Ensenada B.C. 22860, México.*

²*Department of Astronomy and Planetary Science, Northern Arizona University, Flagstaff, AZ 86011, USA*

³*Lowell Observatory, Flagstaff, AZ 86001, USA*

⁴*School of Earth and Space Exploration, Arizona State University, Tempe, AZ 85287, USA*

⁵*Cosmology Initiative, Arizona State University, Tempe, AZ 85287, USA*

ABSTRACT

As part of our multi-observatory, multi-filter campaign, we present results from observations of 238 near-Earth Objects (NEOs) obtained with the RATIR instrument on the 1.5 m robotic telescope at the San Pedro Martir’s National Observatory in Mexico. Our project is focused on rapid response photometric observations of NEOs with absolute magnitudes in the range 20-25. Data with coverage in the near infrared and optical range was analyzed with Machine Learning techniques, while optical-only data was analyzed via Monte Carlo simulations. The rapid response and the use of spectrophotometry allows us to obtain taxonomic classification of sub-kilometer objects with small telescopes, representing a convenient characterization strategy. We present taxonomic classification of the 87 objects observed in the optical and near infra-red. The ratio of primitive to non-primitive objects is estimated for all objects, finding values of ≈ 0.7 and ≈ 0.9 in our sample.

Keywords: asteroids: individual (near-Earth objects) — minor planets — surveys

1. INTRODUCTION

Solar System minor bodies are tracers of the System’s formation and evolution and they can be used as current samples of such processes (Delsemme 1991; Malhotra 1997). In order to understand the processes occurring in our System, studies with numerous samples focused on analyzing colors, taxonomies, orbital and physical properties of asteroids from different populations have been made (see for example Ivezić et al. 2001; Carvano et al. 2010; Carry

et al. 2016). Near-Earth Objects (NEOs), the minor bodies closest to us, originate from the asteroid Main Belt (MB) between the orbits of Mars and Jupiter. Hence our surrounding objects and inform us about the physical properties in the region of the gas giants (Bottke et al. 2002; Granvik et al. 2018) and enable us to take a closer look to the processes that occur in the Solar System.

It is well known that an asteroid of a few dozens of meters in diameter can cause serious damage when impacting (see for example Brown et al. 2013). Given that there exist nearly a million objects (Trilling et al. 2017) of that size or

larger, their discovery and characterization has become a high priority.

We report spectrophotometric observations of asteroids within a H magnitude range of 18.1 to 27.1, with median in 21.8. Using the average albedo for NEOS (Thomas et al. 2011), this is equivalent to a diameter range from diameters from approximately 10 to 600 meters. We acquired them using RATIR, a multi-imager with 4 channels, available to observe in the visible and near infrared wavelengths at the same time. Spectrophotometry consists of photometric measurements at a few key spectral bands, hence collecting the light within a broad bandpass instead of dispersing it as in spectroscopy. It has been shown that spectrophotometry can be sufficient to classify asteroids according to their main compositional features, via a taxonomic scheme (Tholen 1984; Hahn, & Lagerkvist 1988; Ivezić et al. 2001, etc.). Where objects of a given taxonomy cluster in a color diagram, generally creating different zones for each taxonomy. Different taxonomies are defined by distinctive spectral features of the objects. Spectrophotometry also has the advantage of being less expensive than spectroscopy in terms of telescope time and can be performed with smaller telescopes.

Recent observations of asteroids in near Earth space (Devogèle et al. 2019; Binzel et al. 2019; Navarro-Meza et al. 2019; Lin et al. 2018; Perna et al. 2018; Ieva et al. 2018; Erasmus et al. 2017; Mommert et al. 2016), have shown that the taxonomy of NEOs is size dependent and different from the objects in the MB. Currently we are unable to observe subkilometer objects in the MB, so a comparison between these and small NEOs is not possible. These studies agree that S- and Q-types (unweathered version of the former), together with the primitive types C and X, constitute the majority of the small NEOs.

However, the percentage of each taxonomy in the distribution reported by each study can differ by a factor larger than 3: Devogèle et al. (2019) report 17% of S-types, while Ieva et al. (2018) estimates 61%. Several factors affect for the different estimations: the size range considered is not exactly the same; the small size of the sample in most of the studies; observational biases; some studies don't consider Q-types; the quality of the data; the methodology followed, etc. To help with this discrepancy, it is needed to increase the fraction of characterized NEOs. During the process it would be helpful to make studies with larger samples (a few hundreds of objects) using an homogeneous classification method.

Here we present a combination of spectrophotometry and *rapid-response* observations, i.e., observations that are obtained shortly after the discovery of the target, when it is still relatively bright. This study is part of a worldwide systematic survey of NEO compositions (See Mommert et al. 2016; Erasmus et al. 2017; Navarro-Meza et al. 2019, for our previous results), aimed to increase the number of small NEOs with physical information. Which is of interest for science, industry and planetary safety. The rapid response approach is generally not feasible through classical observing proposals due to heavily oversubscribed classically scheduled major research facilities. Furthermore, this method allows us to classify small NEOs according to their taxonomy with a higher efficiency than current spectroscopic methods (see Galache et al. 2015 for a discussion).

Section 2 describes our rapid response approach and the instrument we used. Section 3 addresses our data selection and analysis. In Section 4 we provide our results and the corresponding discussion is given in 5. Finally in

Section 6 we present our conclusions.

2. OBSERVATIONS

We present data taken from 2014 to 2018. Observations were performed with the Reionization And Transients InfraRed camera (RATIR, Butler et al. 2012), on the San Pedro Martir (SPM) 1.5 m telescope at the National Mexican Astronomical Observatory (Observatorio Astronómico Nacional). The instrument is equipped with two optical and two near-infrared (NIR) detectors, all of them 2048x2048 pixels. Each of these detectors correspond to a different channel with specific filters in the optical and NIR, as shown in Table 1. RATIR takes four images of an object in a single shot, enabling us to observe with 6 different filters at a time¹.

Potential targets are identified and uploaded into the RATIR queue on a daily automated basis. Accessible targets are identified among those NEOs that have been discovered within the last four weeks; this duration is partially arbitrary², but the method usually leads to a number of well-observable and bright potential targets. A target is considered accessible if it has a visible brightness $V \leq 20$ and an air-mass ≤ 2.0 , as provided by the JPL Horizons system (Giorgini et al. 1997), for at least the duration of the estimated RATIR integration time.

Potential targets are manually selected from the list of accessible targets, prioritizing objects with high absolute magnitudes H_V (small sizes) and large values of $H_V - V$, where V stands for the apparent magnitude of the target of the upcoming night. A high value of $H_V - V$ ensures

that our target is observed when it is close to the Earth. RATIR queue observing scripts are automatically created for the selected targets, using the latest orbital elements of the objects of interest provided by JPL Horizons. The exposure time of each frame, as well as the total integration time in each band per visit are a function of the object’s brightness. Exposure times usually ranges between 5 and 30 seconds, while the total integration time per target is usually less than 1 hour. A visit is defined as an observational run. One object can have one single visit during our campaign or different ones, made during different days or all in one night. The maximum number of visits of a target reported here is 4.

Our rapid response approach is the key feature of this project. We trigger rapid response spectrophotometric observations of NEOs within a few days of their discovery when the objects are generally still bright. We can observe and characterize objects as faint as $H_{\text{mag}} \approx 27$ (equivalent to a dozen of meters). Such rapid response is generally not feasible through classical observing programs.

Image reduction and photometry is carried out using a pipeline developed for Gamma Ray Burst observations (see, e.g. Littlejohns et al. 2015; Becerra et al. 2017). The pipeline was adapted for working with asteroids: it removes sidereal sources to extract the NEO from the image and coadds in the moving frame of the target. The PSF determined from the sky image is then fit to the moving-target image and the zero point from the sky image is applied to normalize the photometry (see Navarro-Meza et al. (2019) for details). We obtain from the pipeline the magnitude and error of the observed object in each of the 6 broadbands used, which enables us to have 15 different pair wise astronomical colors. The error associated to each color is ob-

¹ See detailed information in RATIR’s web page: <http://ratir.astroscu.unam.mx>

² After the closest approach, NEOs fade at a rate of typically 0.5 mag within one week and 5 mag within 6 weeks (Galache et al. 2015).

Channel	Detector	Field size (arc minute square)	Filters
C0	CCD	5.3	SDSS ugr and seven others
C1	CCD	5.3	Fixed SDSS i
C2	H2RG	10	Fixed WFCAM Z and Y
C3	H2RG	10	Fixed MKO J and H

Table 1. Channels of the RATIR instrument. All detectors are 2048x2048 pixels. C0 and C1 channels hold the visual range filters. C2 and C3 channels contain the near infrared filters; H2RG (HAWAII-2RG) are Teledyne mercury-cadmium-telluride detectors. We report observations using the r, i, Z, Y, J and H filters. For more details, see <http://ratir.astroscu.unam.mx/public/wiki>

tained by adding in quadrature the errors from each of the corresponding bands.

The colors reported in this article were estimated in the Vega system and the solar component has been subtracted.

2.1. Outlier rejection

Our observations were planned in order to observe faint objects within our facility’s capabilities. However, the weather or other factors might interfere during our automated observations. Hence, we use several criteria in order to identify and reject photometric outliers. In next section we describe the different methods we used to analyze our data. One of them makes use of multiple colors to classify each object, while the other one makes the classification using only one color. The rejection method is very similar for all the data, however the multidimensional approach is more accurate, hence we imposed more relaxed limits on the selection of the data analyzed with such method.

For all targets, we visually confirm the performance of the pipeline by verifying that the image resulting from the coaddition is clean: a well defined source and a successful removal of the background sources is required. The next lines describe the selection process of the objects analyzed with the multi-dimensional approach.

We use a $10 - \sigma$ clipping algorithm applied to the measured colors: for all the objects of the sample under analysis, we estimated the variance of each color, and used the largest of them as the standard deviation for the σ clipping. If any of the colors of an object is not within the $10 - \sigma$ limit, all measurements from that object are removed. The later is to keep the set of observations “complete”, concept that will be explained in the next Section. The $10 - \sigma$ clipping was carried out 3 times. Each time the photometric errors from the individual measurements were propagated to obtain the weights for the average. Notice that this step is conservative since it uses the color with the largest, not the smallest variance. However, using the shortest could clip many good measurements in other colors. The rejection process has an additional stage in which we exclude those objects outside the limits of the expected distribution of colors. The expected range is the color distribution(s) of the sample with measured spectra that we use as a reference plus a flexibility of 0.3Δ , where Δ is the range of a given color in the training sample. We reject observations with an error in color larger than 0.13 We tested this upper limit by giving it values between .07 and 0.13, finding no direct correlation between this value and the accuracy on the taxonomy probability for objects in Set 1 (Table 4). For objects

from Set 2, the accuracy in the classification is negatively correlated to the photometric error. However for Set 2, even objects with high error can be classified as primitive or evolved. For example, object 2016 FB (see Table 4) has a $Z - Y$ error of 0.127, but the probability of it being a non-primitive object is 85%.

The procedure applied to objects classified with the 1-dimensional approach is as follows: A limit on the color index's error due to photometric uncertainty of 0.07 was set. The difference in color index between the C- and S-type asteroids is 0.091, hence it is convenient that we only consider the objects that have an error lower than this threshold. As explained below, the 1-D analysis is made with a fit considering the average colors from each of the considered types in the training sample. Objects with a measured color larger than the largest average value (plus the 0.07 error limit) and smaller than the smallest average value (minus 0.07) are excluded. We require a minimum of 4 measurements per visit.

The outcome of this selection process is 87 different for the multidimensional analysis, and 151 objects observed for the 1-D analysis. Making a total of 238 objects.

3. DATA ANALYSIS

We use the MITHNEOS database as a reference for the asteroid's colors. This is hitherto the largest sample of measured NEO spectra³. To obtain the characteristic color of each taxonomic type, its reflectance spectrum is convolved with the spectral response of each of RATIR's filters and the solar spectrum. Details of the process are discussed by Mommert et al. (2016), Section 3. Hereafter, we refer to this

³ <http://smass.mit.edu/minus.html>

database as 'Control Sample'. When referring to all the objects we observed with RATIR we'll do it as 'Observed Sample'.

In an ideal case, the Control Sample would cover the same wavelengths as RATIR's broadband filters. However not all the objects in the control sample have observations in the same wavelength range, and not all the objects from the observed sample have valid measurements in all of the considered bands. To address this, we only consider those objects that have at least half of the coverage in wavelength of a given RATIR's filter.

3.1. Taxonomic classification

We use the Bus-DeMeo scheme (DeMeo et al. 2009) to classify our sample. This is a widely used taxonomic scheme that combines the visible and near infrared ranges, covering from 0.45 to 2.45 μm . The taxonomy includes 24 classes, most of which are sub-types of the C-, S- and X-complexes, which include the majority of the known asteroids (see DeMeo et al. 2009).

The control sample includes objects of most of the classes in the Bus-DeMeo scheme. We train our Machine Learning algorithm on the characteristic colors of each type (see next subsection), we only considered taxonomies that have at least 5 spectra to provide sufficient training data. Based on this constraint and Machine Learning test runs, we decided to use the S, C, X and Q⁴ taxonomic complexes. but not to make a distinction between their individual classes; we also considered the D- and the

⁴ We group the Sq-types with the Q-types, forming the 'Q complex'. In our previous paper we included the Sq-types in the S complex, however in this study we found that the colors of such class are clearly more similar to the ones of the Q- rather than the S-types. Sq-types also tend to be clustered in a 2-dimensional color space. However, the Sqw-types have colors more similar to the S-complex and they are scattered rather than clustered.

V-type objects.

3.2. Machine Learning

We base our analysis on the k-Nearest Neighbors (k-NN), a supervised classification/regression algorithm implemented in Python via Scikitlearn (Pedregosa et al. 2011). We train the algorithm on the training data set, which allows it to classify new data by itself based on what it learned. Then the algorithm is able to work by itself on new data based on what it learned. Our training sample is the MITH-NEOS database (Binzel et al. 2019, data available at: <http://smass.mit.edu/minus.html>) and the algorithm learns the regions of each taxonomic class in an N-dimensional space, where N depends on the number of bands that constitute a particular Complete Set. Once the algorithm is trained, it is fed with a Complete Set and the classification of each of its objects is returned according to their position on the N-dimensional color space.

We recall that not all of the observed objects have valid measurements in the same number of bands. Particularly the colors involving the H band don't meet the criteria explained in Section 2.1, hence we decided not to use such band. We use k-NN and cross validation via GridSearchCV from Scikitlearn to study the training sample and determine which combination of bands is more convenient for classifying the objects. With the use of GridSearchCV (Pedregosa et al. 2011), our ML algorithm uses 80% of the control sample to train itself and 20% to evaluate the training by re-classifying the objects, keeping track of its success on doing so. This is made iteratively, mixing the sample and taking every time different specific objects. The average of the success of assigning the correct classification is the so-called 'test accuracy'. We judge the different filter combinations options by considering the outputs from

GridSearchCV and the number of observed objects with valid measurements on each of the combinations. Table 2 shows the 3 combinations selected and their structure: photometric bands, number of objects, k, training sample accuracy and test sample accuracy. We call each of these combinations 'Complete Sets'. For each of the Sets we obtain an equivalent one from the Control Sample to train our algorithm. Next we extract from the observed sample the objects with valid measurements in such bands. The objects that don't fulfil the selection criteria for Set 1 are returned to the poll of observed data to be considered by Set 2. Equivalently those not suitable for Set 2 are considered for Set 3. This last one is constituted by the $r-i$ color and its analysis is described in Section 3.3.1. All the objects from the observed sample that meet the selection criteria from Section 2.1 belong to a Complete Set.

We exemplify the procedure described above for the case of the first Set: we extract 185 objects with 10 different colors from the control sample to train our code with the use of 10-NN. As a result, we obtained a 10-dimensional space, in which each of the taxonomies considered occupies a characteristic region. Then we fed the code with our observed 1st Complete Set and the algorithm determines the classification of each member according to its position on this 10-dimensional space. Data was scaled prior to the k-NN analysis by using the StandardScaler from Scikitlearn, which normalizes the mean and scales the variance to one. The results from GridSearchCV applied on the training sample, also determine the best parameters to use in each Set for classifying the observed objects.

3.2.1. Monte Carlo clones

The true $a-b$ color from one of our objects for any a,b bands is expected to be in the interval $[\alpha - \varsigma, \alpha + \varsigma]$ in a $1-\sigma$ confidence level, where

Complete Set	Bands	No. of classified objects	k	Training accuracy	Test accuracy
1	r, i, Z, Y, J	64	4	0.884	0.828
2	i, Z, Y	23	9	0.761	0.671
3	r, i	151	-	-	-

Table 2. For its analysis, our data is splitted in three independent Sets. By combining two different bands (out of r, i, Z, Y, J) in a non-commutative way, Set 1 is constituted by 10 different colors, producing a 10-dimensional model (10-D). Similarly, Set 2 makes a 6-D model and Set 3 a 1-D one. Set 1 and 2 are analyzed with a Machine Learning approach using a k-Nearest Neighbors algorithm (see Section 3.2). The third Set is analyzed with a Monte Carlo approach (see Section 3.3.1)

α is the measured value of $a - b$ and ς is the photometric error derived by the pipeline. In order to account for the uncertainty in our classification scheme, 10,000 copies of each Complete Set were generated and classified. From this we can obtain the likelihood of an object to be assigned to different taxonomies, as well as the error in the taxonomy distribution of the Set. The 10,000 copies of each object in the Set were generated under a Gaussian distribution with a mean equal to the measured value of each color and a standard deviation equal to ς . For objects with multiple visits a similar procedure is done: a Gaussian distribution is formed with each visit, centered in the color measured and with a width equal to the error in the measurement. Then, the Gaussians are added and a Gaussian fit is made to them, its mean is taken as the color of the object and its standard deviation as the error. For members of Set 1 with multiple visits, we obtained the taxonomy of each visit independently finding the same classification in the great majority of the objects.

3.3. 1-Dimensional analysis

3.3.1. Monte Carlo simulations with synthetic objects

We consider every object from the third Complete Set as a normalized Gaussian centered at the $r-i$ value and with its width equal to the error on the $r-i$ index. To account for objects observed in different telescope visits, the Gaussian’s normalization factor is divided by the number of visits each object has. The Gaussians from all the objects are added up to build a probability density function (PDF). To obtain the compositional distribution from the PDF, we performed a Monte Carlo (MC) simulation consisting of 10^7 samples of synthetic asteroids. each sample with the same number of objects as in Set 3 but with different taxonomic distributions. The types considered for the synthetic population were selected according to the following criteria. From all the objects reported in the Control Sample’s chart (Binzel et al. 2019), those NEOs with $H > 17$ are extracted, which correspond to subkilometer objects considering an average albedo of 0.28 (Thomas et al. 2011). From these, we use those types that have a representation of more than 1% of the training sample and that belong to one of the taxonomy complexes (we consider Q as a complex), namely: B, C, X, S, Sr, Sk, Sw, Q, Sq. Considering more types could overdue the simplicity of model. The number of objects belonging to these taxonomies is set with

a pseudo-random number generator. First it is assigned the amount of objects in the S, Q and “C+X” complexes.

A Monte Carlo simulation requires a distribution with information from the system. For this we use three Gaussian distributions centered on the expected values of the complexes used, which are derived from the Control Sample: The percentage of spectra classified as each of the complexes is scaled to the sum of all the complexes ($\approx 90\%$). This is equivalent to our model’s assumption that all the objects are members from a complex. We give room for testing other distributions by means of the standard deviation of the Gaussians. In terms of the $\frac{C+X}{S+Q}$ space, our simulations are centered on 0.35 and cover the range $\frac{C+X}{S+Q} \approx [0.06, 0.85]$, considering one standard deviation from the mean of the distributions, thus the actual tested range over 10^7 simulations is wider.

The resulting color index distribution from each run is added up as described at the beginning of this section. We call the result Random Probability Density Function, RPDF, to distinguish it from the PDF from our data. The process is repeated 10^7 times and the reduced χ^2 (χ_r^2) between the distributions is calculated. This 1-D analysis is based on the approach taken in P1 were more details from the process are given.

3.3.2. 1 Nearest Neighbor

We explore the use of the method used in [Erasmus et al. \(2020\)](#) to distinguish between C- and S-type objects. The method can be understood as a simplification of the MC approach previously explained. 10,000 clones are generated under a Gaussian distribution centered in the measured color and with an error equivalent to the propagated photometric error corresponding to the $r-i$ color. The taxonomy

of each synthetic object is determined depending on its relative distance to the characteristic color of the C- and S-types. The classification of each of the observed objects is estimated from the highest probability, based on the classification of each of the clones.

In order to obtain an accuracy value similar to the ‘testing accuracy’ but for the 1-D algorithms, we use the Control Sample as an input on each of them and measured the accuracy of the reclassification. We derive the colors of the color sample from spectra, hence to make this procedure it was needed to approximate the error in the color by propagating the uncertainty from the observations. Both 1-D algorithms over-estimated approximated the value of *fraction* from the Control Sample. The Monte Carlo presented a relative error of 1.02, while the 1-Nearest Neighbor presented a relative error of 2.51. The higher discrepancy using 1-NN is due to the characteristic color of the Q-complex. Q- and Sq-types have characteristic colors between those of the X- and S-complex. Hence, in a binary⁵ 1-NN approach, the classification of members of the Q-complex will be splitted between X- and S-types while due their features they are more similar to the S-types. 1-NN tests were made including the possibility of an object being classified as a Q-type, however the accuracy didn’t improve.

4. RESULTS

We present independently the results obtained with the multi-dimensional Machine Learning approach on the objects with data in the optical and NIR range, and the ones obtained with a one-dimensional approach on the objects with optical-only data. Different authors have taken different approaches and considerations while

⁵ The only possible classifications are X or S

studying small NEOs. Among the factors with a larger effect on the results (ergo the comparison between different ones) is the taxonomies that are considered. For this reason we present the individual classification of each asteroid and the taxonomic distribution when possible, but we also present the results as the ratio of primitive to non-primitive asteroids, roughly equivalent to 'carbonaceous' to 'rocky' type: $fraction = \frac{C+D+X}{A+K+L+O+Q+R+S+T+V}$. Where, C, X, Q and S correspond to the complexes and all types within them. Taxonomies not considered under a particular model have a value equal to zero. Notice that primitive objects tend to have low albedo and a relatively similar color among them, while non-primitive tend to be brighter, with similar colors among them as well.

Table 3 shows the taxonomic distribution found in the 87 objects analyzed with the Machine Learning algorithm, equivalent to a $fraction = 0.64 \pm 0.12$. Figure 1 compares our results by taxonomic type in comparison with the latest study of subkilometer NEOs (Devogèle et al. 2019) and to largest study up to date of this kind (Binzel et al. 2019). Figure 2 compares the value we find for $fraction$ with the corresponding one of such studies, as well as the fraction we find for the 151 objects analyzed with the Monte Carlo (MC) method. Table 4 shows some of the objects classified with this method -full table available online-. This table displays the probability of an object to be assigned to each of the main taxonomies, the highest of them is denoted in bold. The last column refers to the Complete Set that was used to estimate the probabilities: 1 is the 10-D model, 2 is the 6-D model, while 3 is the 1-D model, all of them defined in Table 2.

For the objects with only the $r-i$ color available, we estimate the result from the 7 best matching cases out of the 10^7 runs in the MC

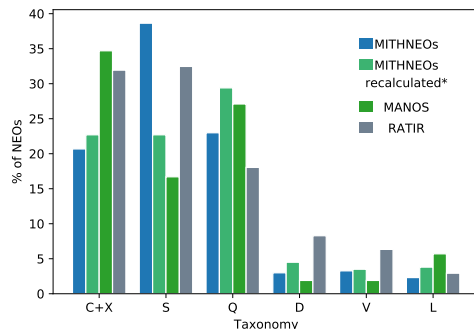


Figure 1. Taxonomic fractions found in our sample analyzed with Machine Learning in comparison with those found by the MITHNEOS survey (Binzel et al. 2019), the MANOS survey (Devogèle et al. 2019) and the MITHNEOS' as re-calculated in Devogèle et al. (2019). We remark that the MITHNEOS and MANOS teams also considered other taxonomies, here we only plot the intersection with the classes we considered, which constitute the majority of the population.

simulation. These 7 cases show the lowest χ^2 values and converge on the number of objects from the S complex. The average of these 7 cases produces a $fraction = 0.87 \pm 0.29$. Considering the relative error obtained for the MC simulations in Section 3.3, the sample could have a $fraction$ as low as 0.43, producing the asymmetric bars shown in Figure 2. The analysis using the 1-NN algorithm yields a $\frac{C}{S} = 1.34 \pm 0.24$.

5. DISCUSSION

5 broad band filters (10 colors) are enough to build a robust model able to distinguish between C, X, Q, S, D, V and L types. The accuracy or detail in the classification can be affected by two main factors. When the training and the observed sample don't match completely in the wavelength range covered, or when a lower amount of bands is available. We find that a model with 5 bands is robust enough to allow for high photometric errors without affecting the general quality of the results.

Taxonomy	Percentage
C+X	31.9 \pm 6.0
S	32.5 \pm 6.2
Q	18.0 \pm 4.5
D	8.3 \pm 3.0
V	6.3 \pm 2.8
L	2.9 \pm 3.4

Table 3. Taxonomic distribution found in the 87 objects analyzed with the Machine Learning algorithm.

Object	Ob. Midtime	Dur.	Hv	P(C)	P(X)	P(Q)	P(S)	P(D)	P(V)	Set
2014 MP5	2014-07-21 04:55	0.5	21	0.00	0.00	0.00	98.40	1.60	0.00	1
2014 MK6	2014-07-22 08:54	0.5	21	71.70	28.20	0.00	0.10	0.00	0.00	1
2014 PT59	2014-08-17 07:32	0.1	20	69.00	15.10	4.90	11.00	0.00	0.00	1
2014 QQ33	2014-08-25 10:04	0.8	22	0.00	7.30	0.00	10.40	82.30	0.00	1
2016 DZ	2016-02-28 06:16	0.6	22	46.40	28.20	6.00	19.40	0.00	0.00	1
2016 DZ	2016-03-02 05:52	0.3	-	-	-	-	-	-	-	-
2016 FB	2016-03-19 06:25	0.2	23	9.20	5.60	30.10	46.80	0.70	7.60	2

Table 4. Observed targets. Observation Midtime, duration of the observing run and absolute magnitude is presented for all objects. For objects classified with Machine Learning in a multidimensional space, it is also shown the probability of an object to be assigned to each of the main taxonomies. In bold the highest of these probabilities. The last column refers to the Complete Set that was used to estimate the probabilities (see Table 2) -full table available online-.

5.1. Efficiency of each method and observational errors

The test accuracy for Set 2 is low (67%, see Table 2), however by using Monte Carlo copies of the objects to 'spread' the error around the color measurement, we are able to obtain highly reliable classifications for some objects. We observed that the dependence of the result on the observational error shallows by increasing the dimensions of the model. For the Machine Learning algorithm we measure this dependence by counting the amount of objects with a taxonomic probability higher than 60% and 90%

as a function of the maximum error on the color allowed for the objects. The proportions from Set 1 (10-D) were not significantly affected while ranging the error limit from 0.07 to 0.13. For Set 2 (6-D), adding objects with an error in color higher than 0.07, will likely produce a less reliable classification. This is not always the case, since the object could have a large error in the filter with least sensitivity but smaller errors in the rest.

The values presented in table 3 are obtained by adding up the probability of every object to belong to each taxonomy. This is equivalent

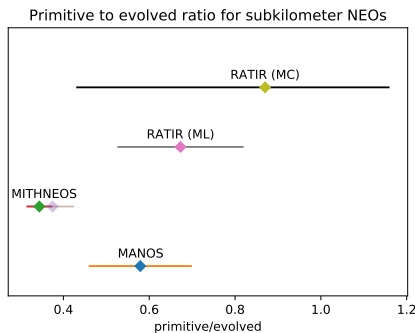


Figure 2. Comparison of the ratio of primitive to non-primitive objects (see text) found in the 87 objects analyzed with Machine Learning (ML) and in the 151 objects analyzed with the Monte Carlo approach (MC). Also shown the equivalent values from MANOS (Devogèle et al. 2019) and MITHNEOS (Binzel et al. 2019). The value from MITHNEOS as re-calculated by (Devogèle et al. 2019) is shown with a water mark .

to adding the probability columns in Table 3 and dividing by the number of objects. This procedure is statistically more correct, since it yields the distribution of the sample as a whole instead of using the result of each individual object to build it. The difference in the percentage of each taxonomy obtained by the two different procedures is lower than 2% and the value of *fraction* differs only by $\sim 5\%$. The low difference between these values suggests robustness in our model, despite the fact that some of the objects in Table 3 have large uncertainty in the classification.

5.2. Limitations and comparison with other studies

Our observations are biased in favor of bright objects. At a given distance from Earth, for objects of a given diameter, those with higher albedo are easier to observe. For targets close to our limiting magnitude, only those with relatively high albedos will be observed. Hence, our sample may contain a higher fraction of S and Q objects than in the actual asteroid population. A similar bias is imposed by the Minimum Orbit

Intersection Distance (MOID) as remarked by Devogèle et al. (2019). For small objects, only those that get close to Earth (small MOID) will be visible with a ground-based small telescope. The close encounter with Earth of an asteroid can cause the rejuvenation of its surface by tidal forces, reducing the effects of space-weathering. This phenomenon could increase the real proportion of Q-types observed from Earth (the ‘nearest Earth objects’), but not necessarily in the whole NEO population.

While using different methodologies on biased and relatively small samples, it is not expected to find exact matches between results of the taxonomic distribution from different studies. Devogèle et al. (2019) finds that even the same sample analyzed with different methods can yield results that do not agree within $1\text{-}\sigma$ Poisson error bars. The results presented in Table 3 and Figure 1 are in better agreement with the ones from the MITHNEOS team presented in Binzel et al. (2019). If we restrict our multi-dimensional analysis to the 74 objects in the range $20 \leq H_V \leq 25$ and compare them to the objects from MITHNEOS in the same range, both distributions agree with the only exception of the D-types objects (see Bottom panel from Figure 3). Perhaps our model is classifying a small amount of S objects as D, or possibly objects of taxonomies not considered by our model are being classified as D-types. This and the other small percentual differences increases the value of *fraction* we derive for this magnitude range, however, as can be seen in the upper panel from Figure 3, our value still agrees with all the other cited studies.

Given the high amount of Q-type objects present in the NEO population, we do not consider the 1-NN model to be appropriate for analyzing this population, due to its high rate of classifying members of the Q complex as C

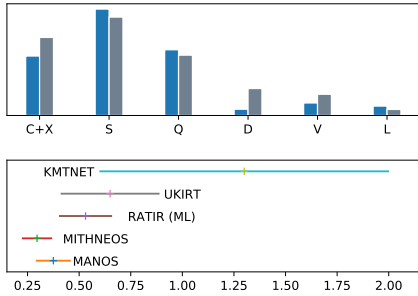


Figure 3. Top: Taxonomic distribution found in our sample analyzed with Machine Learning. Only objects with $20 \leq H_V \leq 25$ are considered. The distribution found by the MITHNEOS (Binzel et al. 2019) team in the same range is shown in comparison. Bottom: Comparison of the fraction of primitive to non-primitive objects for the same H_V range. Values from (MANOS Devogèle et al. 2019), (UKIRT Mommert et al. 2016) and (KMTNET Erasmus et al. 2017) are also included .

types. Having the MITHNEOS sample (Binzel et al. 2019) allowed us to refine our Monte Carlo model with respect to our previous publication (Navarro-Meza et al. 2019). The 1-D analysis performed here includes the objects reported in such work, hence although the results agree within the error bars, we consider the one presented here to be more correct.

While analyzing size dependency in the sub-kilometer NEO population, authors have split the sample in absolute magnitudes bins of $H_V < 20$, $20 \leq H_V < 25$ and $H_V \geq 25$, or analyzed the sample by mass fraction (see Mommert et al. 2016; Erasmus et al. 2017; Binzel et al. 2019). Our observations are focused on targets of magnitudes in the range $20 \leq H_V \leq 25$, hence we have very few objects in the other ranges to make a similar size dependence analysis. We find no variations within the $20 \leq H_V < 25$ range. The value of *fraction* we find for this bin agrees within $1-\sigma$ with all the works cited.

5.3. Implications for large scale projects

The methodologies explored in this article allow for smaller telescopes to study the taxonomy of subkilometer NEOs. They also offer an efficient way to analyze data for large telescopes. Our Machine Learning analysis classified effectively objects with an error in color as large as 0.13 (equivalent to 0.091 magnitude error per band). With high precision photometric measurements, this machinery can classify hundreds of objects in minutes with high accuracy. For example, the Rubin Observatory (Brough et al. 2020) will count with the filters u, g, r, i, Z, Y, four of which we studied here. As a first stage, it would be recommendable to expand the MITHNEOS (Binzel et al. 2019) catalog, since it lacks on observations on the visible range. This would improve the accuracy of the method and likely enable it to distinguish between the classes that compose the taxonomic complexes.

6. CONCLUSIONS

We present a taxonomic study of 238 sub-kilometer NEOs taken with a 1.5 m robotic telescope over the course of 4 years. We obtain our results using 2 different models. The first one is a Machine Learning approach that uses the database from the MITHNEOS survey (Binzel et al. 2019) to classify the objects using multiple photometric color combinations. The second one is a Monte Carlo approach to obtain the taxonomic distribution from the objects in our sample with measurements in only one color. The taxonomic distribution found for the objects analyzed via Machine Learning in the absolute magnitude range that our observations are focused: $20 \leq H_V \leq 25$ match the ones obtained by Binzel et al. (2019) from spectral analysis. In order to compare our results from the different methods and with respect to previous studies which consider different taxonomies,

we also present our results in terms of the ratio of primitive to non-primitive objects. Such value, denoted as *fraction* agrees within the error bars with different previous studies for our main magnitude range. The *fraction* value obtained for all our sample is in better agreement with the equivalent value from Devogèle et al. (2019). The Monte Carlo method offers an approximation that matches within the error bars, however its use is suggested for cases when only two photometric bands are available. In all cases, we find that the primitive asteroids, often denoted as carbonaceous, are a little less common than siliceous objects for the sub-kilometer-biased- population of NEOs.

7. ACKNOWLEDGMENTS

We would like to thank Carlos Román-Zúñiga and Diego Butriago for their help on scheduling

RATIR's observations.

The data used in this paper were totally or partially acquired using the RATIR instrument, funded by the University of California (UC) and NASA Goddard Space Flight Center (GSFC), on the 1.5 meter telescope at Observatorio Astronómico Nacional, San Pedro Martir, operated and maintained by OAN-SPM and IA-UNAM. This project was supported in part by the National Aeronautics and Space Administration under the Grant No.NNX15AE90G issued through the SSO Near Earth Object Observations Program. SNM also acknowledges the grant UNAM- DGAPA PAPIIT IN107316.

REFERENCES

- Becerra, R. L., Watson, A. M., Lee, W. H., et al. 2017, ApJ, 837, 116
- Binzel, R. P., Morbidelli, A., Merouane, S., et al. 2010, Nature, 463, 331
- Binzel, R. P., Reddy, V., & Dunn, T. L. 2015, Asteroids IV, 243
- Binzel, R. P., DeMeo, F. E., Turtelboom, E. V., et al. 2019, Icarus, 324, 41
- Brown, P. G., Assink, J. D., Astiz, L., et al. 2013, Nature, 503, 238
- Bottke, W. F., Morbidelli, A., Jedicke, R., et al. 2002, Icarus, 156, 399
- Brough, S., Collins, C., Demarco, R., et al. 2020, arXiv:2001.11067
- Butler, N., Klein, C., Fox, O., et al. 2012, Proc. SPIE, 8446, 844610
- Butler, N., Watson, A. M., Kutyrev, A., et al. 2017, GRB Coordinates Network, Circular Service, No. 21915, #1 (2017), 21915, 1
- Butler, N., Watson, A. M., Kutyrev, A., et al. 2017, GRB Coordinates Network, Circular Service, No. 22061, #1-2018 (2017), 22061, 1
- Butler, N., Watson, A. M., Kutyrev, A., et al. 2017, GRB Coordinates Network, Circular Service, No. 22182, #1 (2017), 22182, 1
- Carry, B., Solano, E., Eggl, S., & DeMeo, F. E. 2016, Icarus, 268, 340
- Carvano, J. M., Hasselmann, P. H., Lazzaro, D., & Mothé-Diniz, T. 2010, A&A, 510, A43
- DeMeo, F. E., Binzel, R. P., Slivan, S. M., & Bus, S. J. 2009, Icarus, 202, 160
- DeMeo, F. E. & Carry, B. 2014, Nature, 505, 629
- Devogèle, M., Moskovitz, N., Thirouin, A., et al. 2019, AJ, 158, 196
- Delsemme, A. H. 1991, IAU Colloq. 116: Comets in the post-Halley era, 167, 377 Nature and history of the organic compounds in comets - an astrophysical view,
- Erasmus, N., Mommert, M., Trilling, D. E., et al. 2017, AJ, 154, 162
- Erasmus, N., Navarro-Meza, S., McNeill, A., et al. 2020, ApJS, 247, 13
- Granvik, M., Morbidelli, A., Jedicke, R., et al. 2018, Icarus, 312, 181
- Hahn, G., & Lagerkvist, C.-I. 1988, Icarus, 74, 454
- Ieva, S., Dotto, E., Epifani, E. M., et al. 2018, A&A, 615, A127
- Galache, J. L., Beeson, C. L., McLeod, K. K., & Elvis, M. 2015, Planet. Space Sci., 111, 155

- García-Díaz, M. T., González-Buitrago, D., López, J. A., et al. 2014, *AJ*, 148, 57
- Giorgini, J. D., Yeomans, D. K., Chamberlin, A. B., et al. 1997, *BAAS*, 29, 1099
- Hinkle, M. L., Moskovitz, N., Trilling, D., et al. 2015, *AAS/Division for Planetary Sciences Meeting Abstracts #47*, 47, 301.04
- Ivezić, Ž., Tabachnik, S., Rafikov, R., et al. 2001, *AJ*, 122, 2749
- Littlejohns, O. M., Butler, N. R., Cucchiara, A., et al. 2015, *MNRAS*, 449, 2919
- Lin, C.-H., Ip, W.-H., Lin, Z.-Y., et al. 2018, *Planet. Space Sci.*, 152, 116
- Mainzer, A., Bauer, J., Grav, T., et al. 2011, *ApJ*, 731, 53
- Malhotra, R. 1997, *Bulletin of the American Astronomical Society*, 29, 23.02
- McAdam, M. M., Sunshine, J. M., Howard, K. T., et al. 2018, *Lunar and Planetary Science Conference*, 49, 2081
- Mommert, M., Trilling, D. E., Borth, D., et al. 2016, *AJ*, 151, 98
- Moskovitz, N., Thirouin, A., Binzel, R., et al. 2015, *IAU General Assembly*, 22, 2255616
- Navarro-Meza, S., Mommert, M., Trilling, D. E., et al. 2019, *AJ*, 157, 190
- Popescu, M., Perna, D., Barucci, M. A., et al. 2018, *MNRAS*, 477, 2786
- Ricci, D., Ramón-Fox, F. G., Ayala-Loera, C., et al. 2015, *PASP*, 127, 143
- Stuart, J. S., & Binzel, R. P. 2004, *Icarus*, 170, 295
- Pedregosa, F., Varoquaux, G., Gramfort, A., et al. 2011. *Journal of Machine Learning Research*, 12, 2825
- Perna, D., Barucci, M. A., Fulchignoni, M., et al. 2018, *Planet. Space Sci.*, 157, 82
- Ryan, E. L., Mizuno, D. R., Shenoy, S. S., et al. 2015, *A&A*, 578, A42
- Tapia, M., Rodríguez, L. F., Tovmassian, G., et al. 2014, *RMxAA*, 50, 127
- Taylor, John R. 1997, *An introduction to error analysis*, 2nd Ed, , p. 176, University Science Books]
- Tholen, D. J. 1984, Ph.D. Thesis
- Thomas, C. A., Trilling, D. E., Emery, J. P., et al. 2011, *AJ*, 142, 85
- Thomas, C. A., Emery, J. P., Trilling, D. E., et al. 2014, *Icarus*, 228, 217
- Trilling, D. E., Valdes, F., Allen, L., et al. 2017, *AJ*, 154, 170
- Warner, B. D., Harris, A. W., & Pravec, P. 2009, *Icarus*, 202, 134

All Authors and Affiliations

S. NAVARRO-MEZA,^{1,2} M. MOMMERT,^{3,2} D.E. TRILLING,² N. BUTLER,^{4,5} AND M. REYES-RUIZ¹

¹*Instituto de Astronomía, Universidad Nacional Autónoma de México, Ensenada B.C. 22860, México.*

²*Department of Astronomy and Planetary Science, Northern Arizona University, Flagstaff, AZ 86011, USA*

³*Lowell Observatory, Flagstaff, AZ 86001, USA*

⁴*School of Earth and Space Exploration, Arizona State University, Tempe, AZ 85287, USA*

⁵*Cosmology Initiative, Arizona State University, Tempe, AZ 85287, USA*

7. Discusión

Presentamos métodos para determinar la taxonomía de asteroides que son más eficientes en términos de tiempo y recursos que los típicamente utilizados. Esto es conveniente ya que por razones de seguridad planetaria, es apremiante tener información física de los NEOs de menor tamaño, dado que la fracción de ellos que tenemos caracterizada es muy pequeña y son los que presentan mayor posibilidad de impactar la Tierra.

Utilizamos 3 tipos diferentes de clasificación que son recomendables dependiendo de la calidad y cantidad de información que se tenga a partir de las observaciones. En nuestro caso, la mayoría de los NEOs solo tenía mediciones válidas en los filtros del espectro visible r e i . La complejidad de cada modelo es diferente, por lo tanto cada uno considera diferentes clases de asteroides. Para comparar los resultados entre nuestros modelos, así como con otros estudios, dividimos los asteroides en primitivos (generalmente no rocosos) y evolucionados (generalmente rocosos). En el primer grupo se incluyen los asteroides de los complejos C, X y el tipo D, mientras que en el segundo los complejos S, Q y los tipos A, K, L, O, R, T y V.

Nuestro primer modelo se basa en el análisis de dos bandas del espectro visible, r e i , y utiliza una simulación Monte Carlo para generar objetos sintéticos que buscan aproximar la distribución taxonómica de la muestra. El método distingue entre los dos principales tipos de asteroides, C y S, así como los tipos X y Q, teniendo mayor precisión en la determinación de la fracción de tipo S. En este algoritmo hay dos tipos de variables, la distribución taxonómica de objetos sintéticos y los errores de cada uno de ellos. La convergencia del resultado podría darse por medio de los errores, arrojando una distribución incorrecta. Por esta razón generamos 10^7 simulaciones y el resultado se obtiene promediando las distribuciones de los mejores casos. La distribución taxonómica obtenida es en proporción al total de la muestra.

El segundo método es también unidimensional y más sencillo de imple-

mentar. La clasificación de un objeto se determina basándose en la taxonomía más próxima en el espacio unidimensional utilizado. Con este modelo sólo distinguimos entre asteroides de tipo C y S, sin embargo el modelo ofrece una ventaja sobre el primero en el sentido que brinda la clasificación específica de cada objeto observado. Concluimos que no es conveniente utilizar este esquema en poblaciones de asteroides donde es posible que haya objetos de tipo Q o Sq, tal como es el caso de los NEOs, ya que los colores $r-i$ característicos de estos tipos están entre los índices de los tipos C y S, provocando que algunos del complejo Q sean clasificados como C, sobre estimando así la proporción de objetos primitivos.

El tercer método utiliza diferentes filtros para hacer la clasificación y está basado en técnicas de inteligencia artificial. El método determina los límites entre cada clase de asteroide en un espacio multidimensional, por lo que es capaz de hacer una clasificación más detallada de la muestra observada, diferenciando entre las taxonomías C, X, S, Q, D, V y L para cada objeto observado.

El modelo de inteligencia artificial fue aplicado a dos conjuntos de datos, uno con las bandas fotométricas r, i, Z, Y, J , que genera un espacio de 10 dimensiones y otro con las bandas i, Z, Y , que produce un espacio en 6-D. Utilizando mediciones de 87 objetos, los resultados de estos dos conjuntos, sugieren una fracción: $\frac{\text{primitivos}}{\text{evolucionados}} = 0.64 \pm 0.12$. Mientras que con el método Monte Carlo empleado sobre 151 objetos obtenemos $\frac{\text{primitivos}}{\text{evolucionados}} = 0.87 + 0.29, -0.43$. Estos valores concuerdan con los resultados obtenidos por otros autores con muestras y metodologías distintas, particularmente con el de Devogèle et al. (2019) que encuentran un valor de 0.58 para esta fracción. Sin lugar a dudas el método que utiliza inteligencia artificial es el más robusto en términos de precisión y del detalle taxonómico ofrecido, siendo además capaz de clasificar objetos que poseen errores observacionales grandes.

Por otro lado hicimos un estudio de asteroides miembros del cinturón

principal utilizando datos archivados del proyecto de protección planetaria ATLAS. Encontramos que un color en la región óptica del espectro es suficiente para estudiar la diversidad taxonómica de una familia de asteroides. La efectividad del método depende de la posible distribución taxonómica de la familia a estudiar y de los índices de color característicos de esas clases. Sin embargo, típicamente las familias están dominadas por objetos de tipo C y S, cuyos colores característicos son notablemente distintos. Encontramos la clasificación taxonómica y los periodos de rotación de 1612 asteroides, pertenecientes a las familias Flora, Nysa-Polana, Vesta, Themis y Korionis. Estudiando la familia Flora se relacionó la abundancia de asteroides de tipo C con los parámetros orbitales propios de tales objetos. Una de las interpretaciones de este análisis es que el objeto que posiblemente dio origen a la familia Flora como producto de una colisión, era menor a 2 km de diámetro.

La exploración de métodos computacionales es inminente, ya que en la década entrante operará la nueva generación de telescopios espaciales y terrestres que producirán una gran cantidad de descubrimientos serendípicos en adición al tiempo de observación ya asignado a cuerpos menores del sistema solar. Particularmente podemos mencionar el Observatorio Rubin (Ivezić et al., 2019; AURA, 2020). Este telescopio, que se espera que entre en funcionamiento total en 2023, contará con los filtros u, g, r, i, Z, Y, cuatro de ellos utilizados en nuestro análisis. La calidad de las mediciones realizadas por este telescopio con primario de 8.4 metros serán de una calidad incomparable a las analizadas en nuestro estudio. Por lo tanto cualquiera de los métodos analizados aquí sería suficiente para estimar la razón entre objetos primitivos y evolucionados en una muestra de objetos observada con tal telescopio. Para un análisis más detallado se podría utilizar el modelo multidimensional aquí analizado con las siguientes consideraciones. Nuestra muestra control (necesaria para el funcionamiento del modelo) cuenta con pocos objetos con mediciones en la región óptica del espectro. Una opción sería enriquecer la muestra control con mediciones que incluyan pero no estén limitadas al rango visible, esto sería lo más

recomendable, ya que al contar con más objetos control sería posible distinguir entre las subclases que forman cada complejo taxonómico. Cabe destacar que para este caso la muestra control debe ser construida con la misma metodología, ya que Devogèle et al. (2019) encuentran que la misma muestra de espectros puede generar distribuciones diferentes dependiendo de las herramientas de análisis. Otra opción es extrapolar cuidadosamente el espectro de los objetos en la muestra control, algo que no se hizo en nuestro estudio por limitaciones de tiempo. La tercera opción es utilizar solo las bandas i, Z, Y, tal y como hicimos para analizar una fracción de la muestra, sin embargo un menor número de filtros tiende a implicar una menor precisión y/o detalle en la clasificación.

8. Conclusiones

Después de analizar una muestra de 238 objetos cercanos a la Tierra (NEOs) concordamos con estudios recientes en que se observan ligeramente menos NEOs pequeños de tipo primitivo que de tipo rocoso, sin embargo la distribución taxonómica no concuerda con la encontrada en los meteoritos. Además de brindar la clasificación de los objetos, una parte fundamental de este trabajo fue utilizar tres métodos diferentes para estudiar asteroides utilizando fotometría.

El método más robusto utilizado consiste en utilizar técnicas de inteligencia artificial para analizar mediciones fotométricas en múltiples bandas. En términos de taxonomía, este método puede ser tan útil como la espectroscopía, lo cuál representa una ventaja en términos de recursos. También encontramos que este modelo permite trabajar con errores fotométricos grandes sin comprometer la calidad de la clasificación. El método con simulaciones Monte Carlo ofrece una aproximación a la distribución taxonómica en casos donde solo se cuenta con dos bandas fotométricas. El tercer método, basado en la distancia relativa en el espacio de color, permite clasificar de manera simple objetos en poblaciones dominadas por dos tipos de asteroides con colores característicos distintos. En poblaciones más variadas la efectividad de este método se reduce, por lo tanto se considera efectivo para analizar familias de asteroides en el cinturón principal, pero no para el entorno terrestre.

Apéndice: Trabajos adicionales

En esta sección se presentan trabajos en los que participé y que se concluyeron o llevaron a cabo durante el transcurso de mi doctorado. En cada uno se menciona mi nivel de participación.

A. Tránsitos de exoplanetas con múltiples filtros y observatorios

El proyecto consistió en realizar un seguimiento a lo largo de 2 años de más de una docena de exoplanetas con el objetivo principal de encontrar variaciones en el periodo orbital y explorar la posible dependencia de la estimación del radio planetario en el filtro fotométrico utilizado para la observación.

Realicé o ayudé a realizar y planear un gran número de las observaciones tomadas con el telescopio de 84 cm del OAN-SPM. Para esto tomé junto con otros un curso informal de observación con el Dr. Raúl Michel, ya que mi maestría tuvo un enfoque 100 % numérico. Contribuí menormente en la extracción de resultados y análisis. Durante los huecos de observación en el tiempo asignado a este proyecto realicé mis primeras observaciones de asteroides.



Multi-filter Transit Observations of HAT-P-3b and TrES-3b with Multiple Northern Hemisphere Telescopes

D. Ricci^{1,2,3}, P. V. Sada⁴, S. Navarro-Meza³, R. López-Valdivia⁵, R. Michel³, L. Fox Machado³, F. G. Ramón-Fox⁶, C. Ayala-Loera^{3,15}, S. Brown Sevilla⁷, M. Reyes-Ruiz³, A. La Camera⁸, C. Righi^{9,10}, L. Cabona^{9,10}, S. Tosi^{11,12}, N. Truant^{1,2,13}, S. W. Peterson¹⁴, J. Prieto-Arranz^{1,2}, S. Velasco^{1,2}, E. Pallé^{1,2}, and H. Deeg^{1,2}

¹Instituto de Astrofísica de Canarias, E-38205 La Laguna, Tenerife, Spain; davide.ricci82@gmail.com

²Universidad de La Laguna, Departamento de Astrofísica, E-38206 La Laguna, Tenerife, Spain

³Observatorio Astronómico Nacional, Instituto de Astronomía—Universidad Nacional Autónoma de México, Ap. P. 877, Ensenada, BC 22860, México

⁴Departamento de Física y Matemáticas—Universidad de Monterrey, Avenida Ignacio Morones Prieto 4500 Pte., Jesús M. Garza, 66238 San Pedro Garza García, N.L., México

⁵Instituto Nacional de Astrofísica, Óptica y Electrónica, Luis Enrique Erro 1, Tonantzintla, Puebla 72840 México

⁶SUPA, School of Physics and Astronomy, University of St. Andrews, North Haugh, KY16 9SS, Scotland, UK

⁷Facultad de Ciencias Físico-Matemáticas, Benemérita Universidad Autónoma de Puebla, Av. San Claudio y 18 Sur, 72570 Puebla, México

⁸Dipartimento di Informatica, Bioingegneria, Robotica e Ingegneria dei Sistemi (DIBRIS), Università di Genova, Via Dodecaneso 35, 16146 Genova, Italy

⁹Università degli Studi dell'Insubria, via Valleggio 11, 22100 Como, Italy

¹⁰INAF-Osservatorio Astronomico di Brera, via Bianchi 46, 23807 Merate (LC), Italy

¹¹Dipartimento di Fisica—Università degli studi di Genova, Via Dodecaneso 33, 16146 Genova, Italy

¹²Istituto Nazionale di Fisica Nucleare—Sezione di Genova, Via Dodecaneso 33, 16146 Genova, Italy

¹³Dipartimento di Fisica—Università degli Studi di Trieste, Via Alfonso Valerio, 2, 34127 Trieste, Italy

¹⁴Kitt Peak National Observatory, National Optical Astronomy Observatory, 950 N Cherry Avenue, Tucson, AZ, 85719, USA

¹⁵Observatório Nacional MCTIC, Rua Geral José Cristino 77, Rio de Janeiro, RJ, 20921-400, Brasil

Received 2017 March 6; accepted 2017 April 4; published 2017 May 4

Abstract

We present a photometric follow-up of transiting exoplanets HAT-P-3b and TrES-3b, observed by using several optical and near-infrared filters, with four small-class telescopes ($D = 36\text{--}152$ cm) in the Northern Hemisphere. Two of the facilities present their first scientific results. New 10 HAT-P-3b light curves and new 26 TrES-3b light curves are reduced and combined by filter to improve the quality of the photometry. Combined light curves fitting is carried out independently by using two different analysis packages, allowing the corroboration of the orbital and physical parameters in the literature. Results find no differences in the relative radius with the observing filter. In particular, we report for HAT-P-3b a first estimation of the planet-to-star radius $R_p/R_* = 0.1112^{+0.0025}_{-0.0026}$ in the B band which is coherent with values found in the $VRIZ/JH$ filters. Concerning TrES-3b, we derive a value for the orbital period of $P = 1.3061862 \pm 0.0000001$ days which shows no linear variations over nine years of photometric observations.

Key words: planets and satellites: fundamental parameters – (stars:) planetary systems

1. Introduction

The literature of exoplanetary transit observations started with the works of Charbonneau et al. (2000) and Henry et al. (2000), who separately confirmed radial velocity shifts of the star HD 209458 (Vogt et al. 1994; Baranne et al. 1996) due to the presence of its companion HD 209458 b. Since then, big efforts have been made to build up ground-based survey projects such as WASP (Pollacco et al. 2006); HAT (Bakos et al. 2004) and its implementation HATSouth in the Southern Hemisphere (Bakos 2011; Penev et al. 2011); TrES (Alonso et al. 2007); XO (McCullough et al. 2005); KELT (Pepper et al. 2007); and the recent NGTS (Wheatley et al. 2013).

Among the current and forthcoming dedicated space-based programs, we mention *Kepler* (Borucki et al. 2010), PLATO (Rauer et al. 2014), and TESS (Ricker et al. 2010), as well as

the European CHEOPS mission (Fortier et al. 2014), which will help to infer and characterize the exoplanetary population, and which also has the ambition to detect exomoons (Simon et al. 2015) and other interesting features. Such a huge amount of data can benefit from useful online databases such as ETD (Poddany et al. 2010)¹⁶ and exoplanets.eu¹⁷ (Schneider et al. 2011) to help astronomers in programming their observations or defining the best candidates for an independent follow-up.

In this framework, we have recently shown (Ricci et al. 2015) the adequacy of the *San Pedro Mártir—Observatorio*

¹⁶ See, for example, the observations provided by Phil Evans and flagged with a quality of “2” and “3” at <http://var2.astro.cz/ETD/etd.php?STARNAME=WASP-39&PLANET=b>, used to complement Ricci et al. (2015) data.

¹⁷ <http://exoplanets.eu>

Astronómico Nacional (OAN-SPM) facilities, located in north-west Mexico, as a valid resource in the Northern Hemisphere for the follow-up of exoplanetary transits, particularly that of hot Jupiters. The survey, which started in 2014 (Ricci et al. 2014) and is still ongoing, has allowed, to date, the observation of a total of 30 transiting exoplanetary systems¹⁸, mainly with the 84 cm telescope, achieving good quality light curves in several filters, most of them through the Johnson’s *VRI* filters.

In this paper, we focus on two objects: the Jupiter-sized HAT-P-3b and the grazing transiting planet TrES-3b, which we present in Sections 2.1 and 2.2, respectively. Moreover, we will present data from other sites by using not only OAN-SPM survey data, but also light curves obtained from the following facilities: the *Observatorio de la Universidad de Monterrey* (UDEM) in the state of Nuevo León, Mexico; the *Telescopio Carlos Sánchez* (TCS) at the *Observatorio del Teide* (OT) in Tenerife, Spain, provided with WIDE-FASTCAM, a new concept of fast camera with a wide field of view (FoV); and the *Osservatorio Astronomico Regionale Parco Antola, comune di Fascia* (OARPAF) in northern Italy. All of the telescopes and the relative instruments involved in our observations are described in Section 3.1. In particular, WIDE-FASTCAM is a new instrument, and OARPAF is a new facility, and we present their first scientific results. In Sections 3.2 and 4 we focus on observations and data reduction of HAT-P-3b and TrES-3b. Conclusions are described in Section 5.

2. Targets

2.1. HAT-P-3

In the framework of the HATNet survey, Torres et al. (2007) discovered HAT-P-3b, a Jupiter-size planet with a period of 2.899703 ± 0.000054 days, which was the smallest of the 18 transiting extrasolar planets known at that time, with a planet radius $R_p = 0.890 \pm 0.046 R_J$, where R_J stands for the radius of Jupiter. HAT-P-3b immediately appeared to be metal-rich, with a content representing 75 Earth masses M_\oplus , (or, in Jupiter masses, $0.24 M_J$). Radial velocity measurements allowed authors to estimate a planetary mass of $M_p = 0.599 \pm 0.026 M_J$, and found a distance between planet and parent star of 0.03894 ± 0.00070 au, assuming no orbital eccentricity.

System parameters with an improved precision were then updated by Gibson et al. (2010) by fitting seven light curves obtained after performing aperture photometry on short-exposure (4–5 s), wide-band filter (500–700 nm) Liverpool Telescope data. Particular attention was given to possible Earth-mass planets in the inner and outer 2:1 orbital resonance, but the lack of evidence of transit timing variations (TTVs) excluded this hypothesis. Furthermore, Nascimbeni et al. (2011, 2012) refined the orbital parameters and ephemerides

with a timing accuracy of 11 s, demonstrating the potential of the observing and reduction strategy of the TASTE¹⁹ survey.

The anomalous radius of HAT-P-3b, smaller than a pure hydrogen-helium planet suggested the presence of a heavy-element core estimated to be $100 M_\oplus$. This was the subject of the investigation of Chan et al. (2011, 2012), who observed the target in the *i* and *z'* bands, again finding no deviations in the timing of eclipses. Chan et al. (2011) found a period of $P = 2.8997360 \pm 0.0000020$ days, a planet-to-star radius ratio of $R_p/R_* = 0.1063 \pm 0.0020$, an orbital inclination of $i = 87.07 \pm 0^\circ.55$, and a scaled semimajor axis of $a/R_* = 10.39 \pm 0.49$, adopting a circular orbit. An additional follow-up at Kitt Peak National Observatory was carried out by Sada et al. (2012), while Southworth (2012) conducted a homogeneous study of more than 30 extrasolar planets including HAT-P-3b, based on all available data sets in the literature. The author found a larger stellar radius ($0.947^{+0.015}_{-0.027} M_\odot$) and pointed out that further photometric monitoring was needed to get rid of the discrepancy between the data sets of Torres et al. (2007); Gibson et al. (2010); Nascimbeni et al. (2011), and Chan et al. (2011). Finally, a space-based investigation of secondary eclipses in 3.6–4.5 μm spectral bands of the *Spitzer Space Telescope* was carried out by Todorov et al. (2013), finding inefficiencies in heat redistribution, but letting the scenario open about thermal inversion in the atmosphere. Moreover, Todorov et al. (2013) found the eccentricity of HAT-P-3b consistent with zero.

2.2. TrES-3b

TrES-3b is a massive transiting hot Jupiter discovered by O’Donovan et al. (2007) and confirmed by radial velocity measurements. The authors derived a period of $P = 1.30619 \pm 0.00001$ days, a semimajor axis of $a = 0.0226 \pm 0.0013$ au and a near-grazing inclination value of $i = 82.15 \pm 0^\circ.21$. The mass of the planet is estimated to be $M_p = 1.92 \pm 0.23 M_J$ in front of a stellar mass of $M = 0.9 \pm 0.15 M_\odot$, while the planet radius is $R_p = 1.295 \pm 0.081 R_J$. de Mooij & Snellen (2009) reported a temperature of the planet of $T = 2040 \pm 185$ K by measuring the thermal emission in the *K* band using secondary eclipse observations which were carried out with the William Herschel Telescope, which complemented the space-based observations of the Spitzer Telescope.

The same value was found by de Mooij & Snellen (2011). de Mooij & Snellen (2009) also suggest that the planet is in a non-circular orbit. Measurements of the radius of the planet in the *K* band do not significantly differ from the results obtained with optical observations.


Many follow-ups were carried out by several groups in optical and ultraviolet (UV) bands (Turner et al. 2011;

¹⁸ <http://www.astrosen.unam.mx/~indy/spm-transits/>

¹⁹ The Asiago Search for Transit timing variations of Exoplanets.

Table 1

Main Characteristics of Observing Facilities and their Photometric Instruments and Altitude on the Map on the Right



Telescope		OAN-SPM	UDEM	IAC-TCS	OARPAF
Diameter	cm	84	36	152	80
Focal ratio	f/f	15.0	10.0	13.8	8
Latitude	N	31°02'39"	25°40'17.0"	28°18'01.8"	44°35'27.9"
Longitude	W	115°27'49"	100°18'31.0"	16°30'39.2"	350°47'47.0"
Instrument		MEXMAN	SBIG STL-1301E	WIDE-FASTCAM	SBIG STL 11000M
CCD size	px	2043 × 4612	1280 × 1024	1024 × 1024	2004 × 1336
Resolution	arcsec/px	0.25	1.0	0.50	0.29
Field of View	arcmin	8.4 × 19.0	21.3 × 17.1	8 × 8	10 × 10
Gain	e^-/ADU	1.8	2.3	0.10	0.8
Read Out Noise	e^-	4.8	16	2.7 (g1m200)	12

Jones et al. 2012; Smith et al. 2012; Vaňko et al. 2012; Walker-LaFollette et al. 2012). In particular, Turner et al. (2013) did not detect any early ingress in UV as predicted by Vidotto et al. (2011), resulting in an abnormally small strength of the magnetic field. The observations in the near-infrared by de Mooij & Snellen (2009), and the near-UV by Turner et al. (2013), do not show differences in the value of the radius of the planet.

An attempt to calculate TTVs was made for the first time by Thakur et al. (2013), using 32 transits in the existing literature, and five new transits. Authors use dynamic models to suggest the presence of an additional outer planet close to the 1:2 resonance with an estimated mass in terms of Earth masses, $\approx 100 M_{\oplus}$. The result contradicts that found by Kundurthy et al. (2013), which observed an additional set of 11 transits in the framework of the Apache Point Survey of Transit Lightcurves of Exoplanets (APOSTLE), excluding the possibility of other planets and confirming the system's parameters but with reduced error bars. Finally, transit times of TrES-3b were updated by Maciejewski et al. (2013), whose results also support no TTVs.

3. Observations

3.1. Facilities

Observations presented in this paper were carried out by using four different telescopes located in the Northern Hemisphere. A summary of their characteristics is shown in Table 1.

- The first telescope is the OAN-SPM 84 cm. It provides a set of instruments that can be mounted according to the observational needs, among which MEXMAN, a wide-field imager already successfully tested for the observation and characterization of exoplanets using the transit method (Ricci et al. 2015).
- The second telescope is the UDEM 36 cm, a LX200GPS college telescope located close to the city of Monterrey, Mexico, and classed with a minor planet center code of 720. It is available for student training and has been active

for almost 10 years in the field of exoplanetary transit observations Ramón-Fox & Sada (2013); Sada & Ramón-Fox (2016).

- The third telescope, the TCS, is a 152 cm equatorial Cassegrain telescope²⁰ located at the OT and managed by the Astrophysics Institute of Canary Islands (IAC), Spain. This telescope is provided with different instruments. One of them, FASTCAM, allows quasi-diffraction limited real-time observations using the Lucky Imaging technique, the implementation of the instrument being targeted to high temporal resolution up to tens of images per second (Oscos et al. 2008). Despite these advantages, FASTCAM is limited (Murga et al. 2010) by its $20'' \times 20''$ FoV.

For this reason, an implementation of the FASTCAM detector with a wider FoV was carried out: WIDE-FASTCAM offers a 1024×1024 px EMCCD array and an optical design (Murga et al. 2014) to provide observers with an $\approx 8 \times 8'$ FoV. We used WIDE-FASTCAM for our observations to test its small readout time and low electronic noise. Linearity tests on the camera on flat-field images show that the instrument works in the linear regime between 1700 and 4000 counts (Velasco et al. 2016, 2017). During the observations, we took care to tune the exposure time accordingly.

- The fourth telescope is the alt-azimuthal²¹ OARPAF 80 cm, located near Mt. Antola in Northern Italy, and whose scientific activity is managed by the physics department (DIFI) of the University of Genova, Italy. The telescope was designed by the Astelco company²² to foresee a double focal station: the first, provided with a field derotator, is dedicated to scientific observations and is currently equipped with an air-cooled SBIG STL 11000M camera and a standard *UBVRI* Johnson filter wheel (Federici et al. 2012); the second is dedicated to ocular observations by amateurs.

²⁰ <http://www.iac.es/telescopes/pages/es/inicio/telescopios/tcs.php>

²¹ <https://www.difi.unige.it/it/ricerca/altri-progetti/osservatorio-monte-antola>

²² <http://www.astelco.com>

Table 2
Log of HAT-P-3b Observations

Date (UT)	Filter	Exp. time	Observatory
2009-01-19	<i>Ic</i>	60 s	UDEM
2009-04-22	<i>Ic</i>	60 s	UDEM
2009-05-15	<i>JH</i>	30 s	KPNO ^a
2009-05-15	<i>z'</i>	60 s	KPNO-VCT ^a
2009-05-21	<i>Ic</i>	60 s	UDEM
2010-05-27	<i>JH</i>	20 s	KPNO ^a
2010-05-27	<i>B</i>	45 s	KPNO-VCT ^a
2012-04-22	<i>Ic</i>	60 s	UDEM
2012-05-24	<i>Ic</i>	60 s	UDEM
2013-06-02	<i>Ic</i>	60 s	UDEM
2014-04-01	<i>R</i>	120 s	OAN-SPM
2014-03-13	<i>R</i>	120 s	OAN-SPM
2014-03-16	<i>I</i>	120 s	OAN-SPM
2014-05-13	<i>V</i>	90 s	OAN-SPM

Note.

^a Published in Sada et al. (2012).

Pointing and positioning of the secondary mirror are controlled using the proprietary *AstelOS* software, provided by the constructor, on a dedicated Linux machine, while the image data capture is managed by the *MaxIm* software. The time stamp is obtained via a global positioning system (GPS) device. The instrument was recently fully characterized with standard stars observations in all available filters for zero-point determination and extinction coefficient determination. Concerning the CCD commissioning, deep tests allowed calculation of: gain, Read Out Noise, dark current, plate scale, and linearity regime (Righi 2016).

3.2. Targets

We carried out four observations of HAT-P-3b at OAN-SPM in nearly full-moon conditions in 2014 over a period spanning five months and using three filters: two with the *R* filter, one with the *I* filter, and the final one with the *V* filter. Except for the first *R* observation, we were able to follow the target for roughly five hours. We also obtained six transits from UDEM taken with the *Ic* filter between 2009 and 2013. Moreover, we also aggregated four already published observations from Sada et al. (2012): two light curves from the Kitt Peak National Observatory (KPNO) 200 cm telescope observed with the *JH* filter, and one light curve from the KPNO Visitor Center Telescope (KPNO-VCT) 51 cm telescope with the *B* filter and one curve from the same telescope with the Sloan *z'* filter. A log of HAT-P-3b observations is shown in Table 2.

Concerning TrES-3b, we obtained three complete light curves in the *R* band at OAN-SPM, and two in the *I* band. Except for the first *I* light curve, we used the defocused photometry method described in detail by Southworth et al.

Table 3
Log of TrES-3b Observations

Date (UT)	Filter	Exp. time	Observatory
2007-07-23	<i>Ic</i>	120 s	UDEM
2007-08-09	<i>Ic</i>	120 s	UDEM
2008-07-11	<i>Ic</i>	60 s	UDEM
2008-07-15	<i>V</i>	90 s	UDEM
2008-10-04	<i>V</i>	90 s	UDEM
2009-05-06	<i>z'</i>	45 s	KPNO-VCT
2009-05-10	<i>z'</i>	120 s	KPNO-VCT
2009-05-31	<i>Ic</i>	120 s	UDEM
2009-07-17	<i>z'</i>	120 s	UDEM
2010-04-04	<i>z'</i>	40 s	StPr
2010-04-25	<i>V</i>	90 s	UDEM
2010-06-19	<i>V</i>	90 s	UDEM
2010-07-19	<i>V</i>	90 s	UDEM
2010-08-05	<i>Ic</i>	90 s	UDEM
2011-04-27	<i>Ic</i>	90 s	UDEM
2011-06-08	<i>Rc</i>	60 s	UDEM
2011-08-24	<i>Rc</i>	60 s	UDEM
2012-08-12	<i>Rc</i>	60 s	UDEM
2013-08-14	<i>Rc</i>	60 s	UDEM
2013-10-08	<i>V</i>	90 s	UDEM
2014-06-13	<i>Rc</i>	60 s	UDEM
2015-07-17	<i>R</i>	120 s	TCS ^a
2015-08-03	<i>R</i>	120 s	OARPAF
2015-08-22	<i>R</i>	120 s	OAN-SPM
2016-04-09	<i>R</i>	120 s	OAN-SPM
2016-04-13	<i>R</i>	120 s	OAN-SPM
2016-05-30	<i>I</i>	60 s	OAN-SPM ^b
2016-06-03	<i>I</i>	60 s	OAN-SPM

Notes.

^a Binning 120 individual frames of 1 s each.

^b Binning 6 individual frames of 10 s each.

(2014) and in previous papers of the series. We also present 18 UDEM transits: six with the *V* filter, five with the *Rc* filter, six in the *Ic* band, and finally one in the *z'* band. Additional *z'* data come from KPNO (two curves). An additional curve in the *z'* band comes from the KPNO-VCT operator Steven Peterson (StPr) using his private observatory, and located close to the KPNO facilities. TCS also observed the target one night by using WIDE-FASTCAM and short-exposure images of 1 s each, in the *R* band. Finally, one observation with the *R* filter was carried out at OARPAF. We carefully checked that the targets and reference stars were not relaying too close to hot or bad pixels or bad lines of devices, nor at the edge of their FoV. We also used a 2×2 binning for our observations in OAN-SPM, UDEM and OARPAF, windowing the devices in order to minimize the readout time. OAN-SPM, UDEM, and OARPAF telescopes were also slightly defocused in order to spread the point spread function over a large number of pixels, allowing longer exposure times, a shorter total readout time, and reducing errors due to pixel response or flat-field correction problems. A log of TrES-3b observations is shown in Table 3.

4. Data Analysis

Images of both targets were debiased and flat-field corrected. We used the aperture photometry technique to obtain light curves. In particular, we used the `defot` routine (Southworth et al. 2010) written in the IDL language that we modified to work with FITS headers generated by the OAN-SPM, TCS, and OARPAF telescopes, while UDEM data were reduced using independent custom IDL routines. OAN-SPM and OARPAF images were not aligned, as we decided to calculate and follow, for each image, the centroid of the target and that of the reference stars, by using a cross-correlation method that we re-implemented in `defot`. For the OARPAF data coming from an Alt-Az telescope, we set up a rotation tracking subroutine to correct for the residual rotation of the field due to eventual errors in the alignment between the optical axis, the derotator, and the CCD center.

Several field stars were tested to find a reference from which performing differential photometry, and for both HAT-P-3b and TrES-3b we chose a number between two and eight non-saturated reference stars with count values as close as possible to those of the target, also taking into account sky conditions and availability.

A first-order trend in light curves was removed with the technique described by Ramón-Fox & Sada (2013) to get rid of airmass effects. Timestamps of the light curve points were converted to the dynamical time-based system (BJD_{TDB}), applying the transformation given by Eastman et al. (2010).

Data were then combined by using the procedure described by Sada & Ramón-Fox (2016). Using this procedure, we obtained a total of seven combined curves for HAT-P-3b for each one of the following filters: *B* (one curve from KPNO-VCT), *V* (one curve from OAN-SPM), *R* (two curves from OAN-SPM), *I* (one curve from OAN-SPM), *Ic* (six curves from UDEM), *z'* (one curve from KPNO-VCT), and *JH* (two curve from KPNO).

The same technique was applied to TrES-3b data and we obtained a total of six combined curves in the different filters as follows: *V* (six curves from UDEM), *R* (three curves from OAN-SPM, one from TCS, and one from OARPAF), *Rc* (five curves from UDEM), *I* (two curves from OAN-SPM), *Ic* (six curves from UDEM), *z'* (two curves from KPNO, one from StPr, and one from UDEM).

Light curves were fitted with EXOFAST (Eastman et al. 2012, 2013). A value of the inclination i , of the semimajor axis in terms of the host star radius a/R_* , of the mid-time T_{mid} , and of the radius of the planet in terms of the host star radius R_p/R_* were fitted for each combined curve. An independent light curve fitting was performed by using the IDL software Transit Analysis Package (TAP) implemented by Gazak et al. (2011). Both software use a Markov Chain Monte Carlo (MCMC) method to find best fit parameters for the Mandel & Agol (2002) model.

HAT-P-3b combined light curves and fit

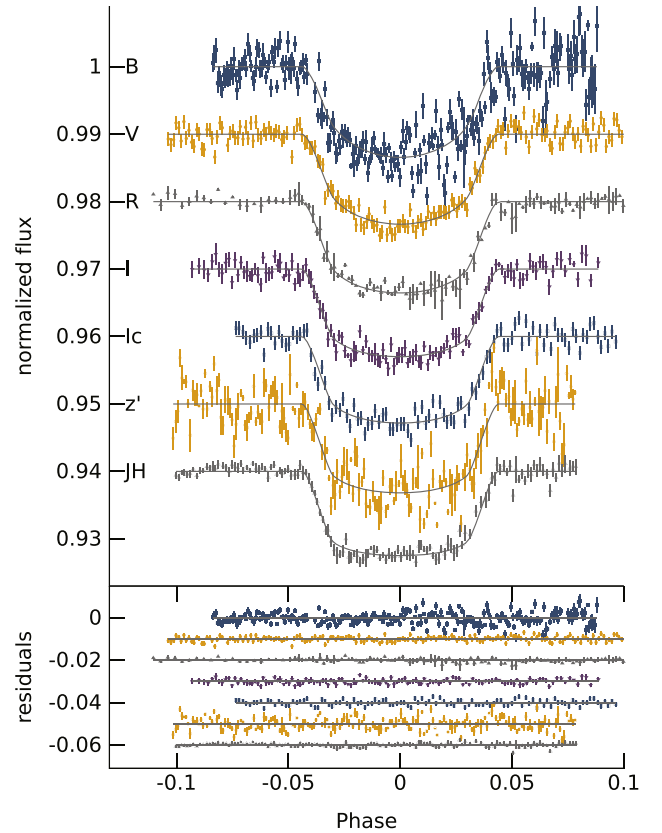


Figure 1. Combined light curves of HAT-P-3b and fit models. Models are slightly shifted in flux for better visualization. The lower panel shows the residuals.

Differing from EXOFAST, TAP allows fitting together, or separately, a set of parameters linking their value with a lock matrix. Thus, it was possible to simultaneously fit a unique value of the inclination i and of the scaled semimajor axis a/R_* for all combined curves, a different Mid-time T_{mid} value for each light curve, and a scaled planet radius R_p/R_* value for each of the different observing filter.

4.1. HAT-P-3b

In fitting procedures, we fixed the period: $P = 2.8997382$ days (Sada et al. 2012), and we supposed a circular orbit (eccentricity $e = 0$, argument of periastron $\omega = 0$). Concerning limb darkening, for EXOFAST fitting we used interpolated values from Claret (2000) with the following parameters: $T_* = 5224 \pm 69$ K, $\log g_* = 4.58 \pm 0.03$, and $[Fe/H]_* = 0.41 \pm 0.08$ (Torres et al. 2007, 2012); while for TAP fitting, we used an online tool (Eastman et al. 2012, 2013) that interpolates atmosphere models of Claret & Bloemen (2011).

Table 4
EXOFAST Fit Results for HAT-P-3b

Filter	Obs.	i	a/R_*	R_p/R_*
B	KPNO-VCT	$86.78^{+0.29}_{-0.27}$	$10.17^{+0.37}_{-0.34}$	$0.1112^{+0.0025}_{-0.0026}$
V	OAN-SPM	$86.57^{+0.27}_{-0.26}$	$10.19^{+0.34}_{-0.32}$	$0.1111^{+0.0018}_{-0.0018}$
R	OAN-SPM	$86.83^{+0.36}_{-0.39}$	$10.12^{+0.34}_{-0.36}$	$0.1079^{+0.0014}_{-0.0012}$
I	OAN-SPM	$86.71^{+0.29}_{-0.27}$	$10.18^{+0.32}_{-0.31}$	$0.1083^{+0.0015}_{-0.0015}$
Ic	UDEM	$86.74^{+0.31}_{-0.29}$	$10.18^{+0.32}_{-0.30}$	$0.1094^{+0.0012}_{-0.0012}$
z'	KPNO-VCT	$88.96^{+0.71}_{-0.90}$	$10.04^{+0.16}_{-0.21}$	$0.1129^{+0.0015}_{-0.0015}$
JH	KPNO	$86.60^{+0.25}_{-0.24}$	$10.16^{+0.29}_{-0.28}$	$0.1084^{+0.0008}_{-0.0008}$

Fit results obtained with EXOFAST are shown in Figure 1 and in Table 4. In particular, weighted means obtained with EXOFAST are consistent with those of Nascimbeni et al. (2011): EXOFAST obtain $i = 86.73^{+0.11}_{-0.11}$ against $86.75^{+0.10}_{-0.10}$ of Nascimbeni et al. (2011); $a/R_* = 10.13^{+0.11}_{-0.11}$ against $10.12^{+0.32}_{-0.32}$; and $R_p/R_* = 0.1093^{+0.0005}_{-0.0005}$ against $0.1094^{+0.0011}_{-0.0011}$. TAP calculates a unique value for the first two parameters: the inclination $i = 86.27^{+0.28}_{-0.18}$ and the scaled semimajor axis $a/R_* = 9.65^{+0.28}_{-0.18}$, which are slightly different from EXOFAST and Nascimbeni et al. (2011) results, but in agreement within 3σ . A visual comparison between EXOFAST and TAP fit values of the scaled planet radius R_p/R_* is shown in Figure 2.

Figure 2 also show additional TAP fit solutions obtained by fixing i and a/R_* found by Chan et al. (2011) and Nascimbeni et al. (2011), and fitting only a separate value of R_p/R_* for each observing filter. The figure gives evidence of the fact that we find no significant radius variation with the observing filter. Figure 3 shows the calculated mid-times.

4.2. TrES-3b

We used the same technique applied for HAT-P-3b fitting for what concerns TrES-3b limb darkening with following parameters: $\log(g_*) = 4.571 \pm 0.006$ (Southworth 2011), $T_* = 5650 \pm 75$ K, and $[Fe/H]_* = -0.19 \pm 0.08$ (Sozzetti et al. 2009).

EXOFAST fit results of TrES-3b are shown in Figure 4 and in Table 5.

While performing the TAP fit, we fitted a unique value of i and a/R_* for all combined curves, and we fitted separately a value of R_p/R_* for each considered filter. TAP results show good agreement with the EXOFAST weighted averages of i and a/R_* : $i = 81.70^{+0.17}_{-0.22}$ of TAP against $81.63^{+0.20}_{-0.23}$ of EXOFAST, and $a/R_* = 5.885^{+0.068}_{-0.080}$ of TAP against 5.903 ± 0.062 of EXOFAST. Results are slightly lower than, but in agreement with, the values provided by Kundurthy et al. (2013): $i = 81.86^{+0.08}_{-0.26}$ and $a/R_* = 5.91^{+0.04}_{-0.05}$. Concerning R_p/R_* , we have differences between the two fit procedures which are within -2σ (for the V filter) and $+1\sigma$ (for the I filter).

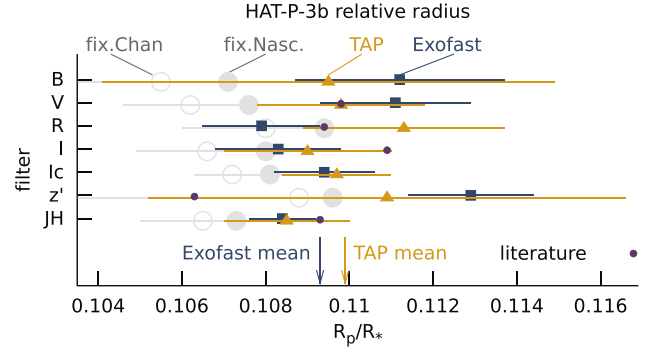


Figure 2. R_p/R_* values of HAT-P-3b for each observing filter resulting from EXOFAST and TAP fit procedures. Arrows show weighted means. Large light circles show TAP results obtained by fixing i and a/R_* with values provided by Chan et al. (2011) and Nascimbeni et al. (2011). Small bold circles show values provided in the literature: $V + R$ (Gibson et al. 2010), R (Nascimbeni et al. 2011), I (Torres et al. 2007), z' (Chan et al. 2011), and JH (Sada et al. 2012).

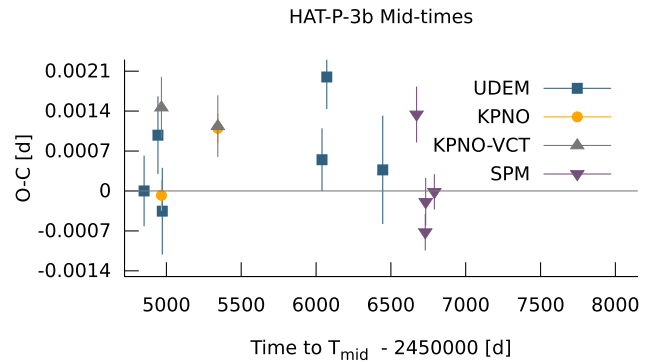


Figure 3. Observed minus calculated mid-times values for HAT-P-3b observations presented in this work.

Comparisons of R_p/R_* between different filters show a maximum absolute variation of 2.9σ between R and V curves in EXOFAST results, which are not confirmed by TAP results (0.04σ). We then assume no R_p/R_* variations with the observing filters, and we consider average results finding good agreement between fit procedures: $R_p/R_* = 0.1665^{+0.0081}_{-0.0050}$ for EXOFAST and $0.1667^{+0.0047}_{-0.0035}$ for TAP, against the value of 0.1649 ± 0.0015 provided by Kundurthy et al. (2013) in the r' band (see Figure 5).

Figure 5 also shows additional TAP fit solutions obtained by fixing i and a/R_* found by Kundurthy et al. (2013) and (Turner et al. 2013), and fitting only a separate value of R_p/R_* for each observing filter.

Mid-times fit linearly a period of $P = 1.3061862 \pm 0.0000001$ days (see Figure 6). Scatter of calculated values of T_{mid} corresponds to variations of ≈ 4 minutes peak-to-valley,

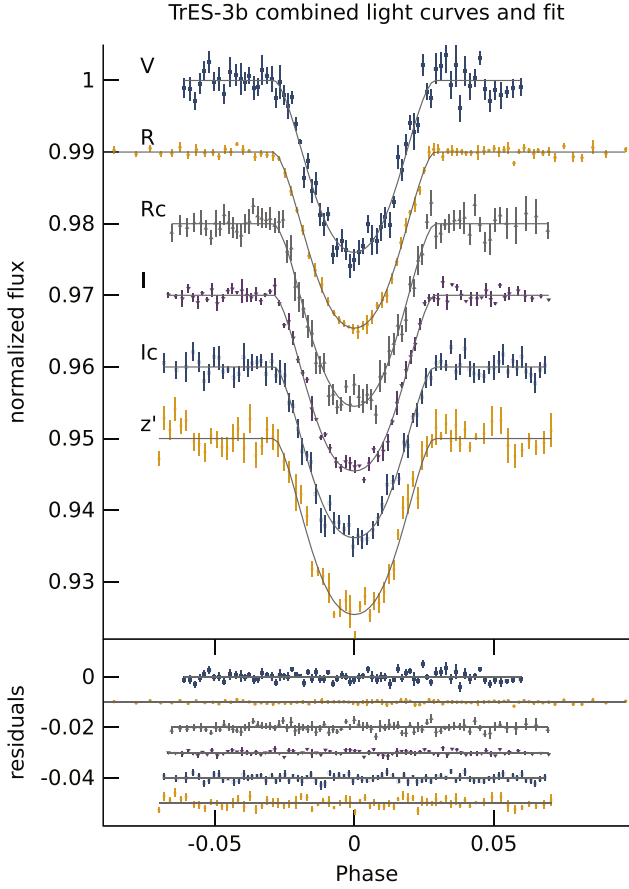

Figure 4. Light curves of TrES-3b and fit. The lower panel shows the residuals.

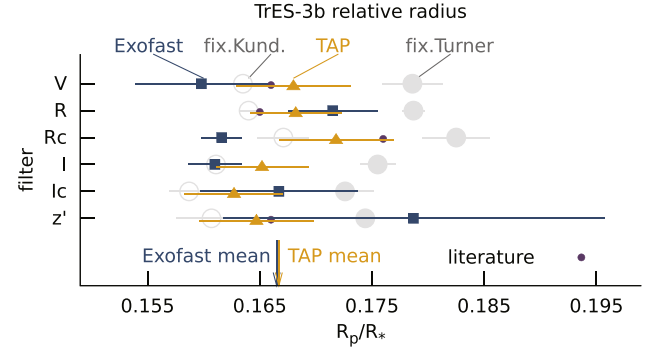
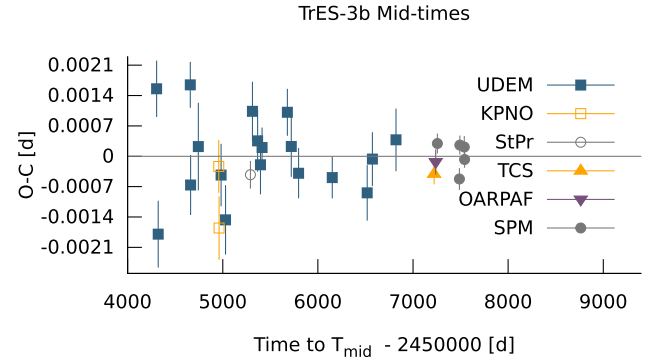
Table 5
 EXOFAST Fit Results for TrES-3b

Filter	Obs.	i	a/R_*	R_p/R_*
V	UDEM	$81.34^{+0.23}_{-0.25}$	$5.903^{+0.066}_{-0.066}$	$0.1598^{+0.0059}_{-0.0045}$
R	a	$81.80^{+0.15}_{-0.17}$	$5.899^{+0.054}_{-0.056}$	$0.1715^{+0.0040}_{-0.0030}$
Rc	UDEM	$81.59^{+0.15}_{-0.14}$	$5.913^{+0.060}_{-0.059}$	$0.1616^{+0.0018}_{-0.0019}$
I	OAN-SPM	$81.77^{+0.14}_{-0.16}$	$5.895^{+0.061}_{-0.061}$	$0.1610^{+0.0024}_{-0.0015}$
Ic	UDEM	$81.83^{+0.19}_{-0.22}$	$5.902^{+0.063}_{-0.064}$	$0.1667^{+0.0070}_{-0.0050}$
z'	b	$81.46^{+0.28}_{-0.37}$	$5.906^{+0.067}_{-0.066}$	$0.1787^{+0.0170}_{-0.0095}$

Notes.
^a Combining OAN-SPM, OARPAF, and TCS data.

^b Combining UDEM, KPNO, and StPr data.

mostly ruled by UDEM data, which is reduced to ≈ 1 minute peak-to-valley while considering OAN-SPM, OARPAF, and TCS data. Calculated mid-times show no significant linear variation of the period with the time and our sampling does not allow us to search for periodic variations in the 1:2 resonance as in the work of Thakur et al. (2013).


Figure 5. R_p/R_* values of TrES-3b for each observing filter resulting from EXOFAST and TAP fit procedures. Arrows show weighted means. Large light circles show TAP results obtained by fixing i and a/R_* with values provided by Kundurthy et al. (2013) and (Turner et al. 2013). Small bold circles show values provided in the literature: V and Rc (Turner et al. 2013), R (Kundurthy et al. 2013), and z' (O'Donovan et al. 2007).

Figure 6. Observed minus calculated mid-times values for TrES-3b observations presented in this work. Data are consistent with a $P = 1.3061862 \pm 0.0000001$.

5. Conclusions

We obtained 10 new exoplanetary transit observations of HAT-P-3b in the $BVRIZ'JH$ bands, and 26 new observations of TrES-3b in the $VRIz'$ bands, which confirmed the potential adequacy of small-size telescopes (36–152 cm) for this research topic. In particular, the new OARPAF observatory and the new instrument WIDE-FASTCAM at TCS can provide reliable photometric observations in the framework of ground-based exoplanetary transit follow-ups.

The simultaneous fit of light curves, carried out in multiple observing bands by several telescopes, allowed us to achieve orbital and physical parameters which corroborate results of Nascimbeni et al. (2011) for what concerns HAT-P-3b, and of Kundurthy et al. (2013) for what concerns TrES-3b.

We also report specific values of R_p/R_* in multiple optical and near-infrared bands, and a first estimation of this parameter in the B band for HAT-P-3b which is coherent with our values provided by using other filters.

We find that observing filters do not significantly influence the determination of the relative radius of HAT-P-3b and TrES-3b. This result confirms the relative radius of HAT-P-3b estimated by near-infrared band observations (de Mooij & Snellen 2009), and the relative radius of TrES-3b estimated by UV observations (Turner et al. 2013) in the literature.

Mid-times of TrES-3b fit a $P = 1.3061862 \pm 0.0000001$ days, finding no significant linear variations of the period over ≈ 9 years of photometric observations. Further observations are planned to discriminate eventual R_p/R_* variations with the observing filter and to extend T_{mid} information to estimate TTVs.

The authors acknowledge the following financial support: D.R. from the Spanish Ministry of Economy and Competitiveness (MINECO) under the 2011 Severo Ochoa Program MINECO SEV-2011-0187; L.F.M. and R.M. from the UNAM under grant PAPIIT IN 105115; D.R. and F.G.R.F. from the CONACYT scholarship for postgraduate studies in Mexico. Research was carried out thanks to the support of UNAM-DGAPA-PAPIIT project IN115413. S.N. thanks H. Navarro-Meza for assistance during OAN-SPM observations in 2016/06. D.R. thanks Claudia Molina and Katie Marley for language editing and the anonymous referee for suggestions and remarks. We also acknowledge the OAN staff for daily support. The 1.5 m Carlos Sánchez Telescope is operated on the island of Tenerife by the Instituto de Astrofísica de Canarias in the Spanish Observatorio del Teide.

Facilities: OAN-SPM 84 cm (MEXMAN), UDEM 80 cm, TCS 152 cm (WIDE-FASTCAM), OARPAF 80 cm.

References

- Alonso, R., Brown, T. M., Charbonneau, D., et al. 2007, in ASP Conf. Ser., 366, *Transiting Extrapolar Planets Workshop*, ed. C. Afonso, D. Wel Drake, & T. Henning (San Francisco, CA: ASP), 13
- Bakos, G. 2011, *BAAS*, 43, 103.04
- Bakos, G., Noyes, R. W., Kovács, G., et al. 2004, *PASP*, 116, 266
- Baranne, A., Queloz, D., Mayor, M., et al. 1996, *A&AS*, 119, 373
- Borucki, W. J., Koch, D., Basri, G., et al. 2010, *Sci*, 327, 977
- Chan, T., Ingemir, M., Winn, J. N., et al. 2011, *AJ*, 141, 179
- Chan, T., Ingemir, M., Winn, J. N., et al. 2012, *AJ*, 144, 90
- Charbonneau, D., Brown, T. M., Latham, D. W., & Mayor, M. 2000, *ApJL*, 529, L45
- Claret, A. 2000, *A&A*, 363, 1081
- Claret, A., & Bloemen, S. 2011, *A&A*, 529, A75
- de Mooij, E., & Snellen, I. 2011, in ASP Conf. Ser., 450, *Molecules in the Atmospheres of Extrasolar Planets*, ed. J. P. Beaulieu, S. Dieters, & G. Tinetti (San Francisco, CA: ASP), 59
- de Mooij, E. J. W., & Snellen, I. A. G. 2009, *A&A*, 493, L35
- Eastman, J., Gaudi, B. S., & Agol, E. 2012, EXOFAST: Fast transit and/or RV fitter for single exoplanet, Astrophysics Source Code Library, ascl:1207.001
- Eastman, J., Gaudi, B. S., & Agol, E. 2013, *PASP*, 125, 83
- Eastman, J., Siverd, R., & Gaudi, B. S. 2010, *PASP*, 122, 935
- Federici, A., Arduino, P., Riva, A., & Zerbi, F. M. 2012, in *Astronomical Society of India Conf. Ser.* 7, 7
- Fortier, A., Beck, T., Benz, W., et al. 2014, *Proc. SPIE*, 9143, 2
- Gazak, J. Z., Johnson, J. A., Tonry, J., et al. 2011, *Transit Analysis Package (TAP and autoKep): IDL Graphical User Interfaces for Extrasolar Planet Transit Photometry*, Astrophysics Source Code Library, ascl:1106.014
- Gibson, N. P., Pollacco, D. L., Barros, S., et al. 2010, *MNRAS*, 401, 1917
- Henry, G. W., Marcy, G. W., Butler, R. P., & Vogt, S. S. 2000, *ApJL*, 529, L41
- Jones, M. L., Adams, E. R., & Carter, J. A. 2012, in *American Astronomical Society Meeting Abstracts* 219, 339.01
- Kundurthy, P., Becker, A. C., Agol, E., Barnes, R., & Williams, B. 2013, *ApJ*, 764, 8
- Maciejewski, G., Puchalski, D., Saral, G., et al. 2013, *IBVS*, 6082, 1
- Mandel, K., & Agol, E. 2002, *ApJL*, 580, L171
- McCullough, P. R., Stys, J. E., Valenti, J. A., et al. 2005, *PASP*, 117, 783
- Murga, G., Oscoz, A., López, R., et al. 2014, *Proc. SPIE*, 9147, 6
- Murga, G., Sanquircce, R., Campo, R., et al. 2010, *Proc. SPIE*, 7735, 3
- Nascimbeni, V., Piotto, G., Bedin, L. R., & Damasso, M. 2011, *A&A*, 527, A85
- Nascimbeni, V., Piotto, G., Bedin, L. R., & Damasso, M. 2012, *MSAIS*, 19, 105
- O'Donovan, F. T., Charbonneau, D., Bakos, G. Á, et al. 2007, *ApJL*, 663, L37
- Oscoz, A., Rebolo, R., López, R., et al. 2008, *Proc. SPIE*, 7014, 47
- Penev, K., Csabry, Z., & Bakos, G. 2011, *BAAS*, 43, 253.01
- Pepper, J., Pogge, R. W., DePoy, D. L., et al. 2007, *PASP*, 119, 923
- Poddany, S., Brát, L., & Pejcha, O. 2010, *NewA*, 15, 297
- Pollacco, D. L., Skillen, I., Collier Cameron, A., et al. 2006, *PASP*, 118, 1407
- Ramón-Fox, F. G., & Sada, P. V. 2013, *RMxAA*, 49, 71
- Rauer, H., Catala, C., Aerts, C., et al. 2014, *ExA*, 38, 249
- Ricci, D., Ramón Fox, G., Ayala, C., et al. 2014, in *AAS/Division for Planetary Sciences Meeting Abstracts* 46, 210.04
- Ricci, D., Ramón-Fox, F. G., Ayala-Loera, C., et al. 2015, *PASP*, 127, 143
- Ricker, G. R., Latham, D. W., Vanderspek, R. K., et al. 2010, *BAAS*, 42, 450.06
- Righi, C. 2016, *NCimC*, 39, 284
- Sada, P. V., Deming, D., Jennings, D. E., et al. 2012, *PASP*, 124, 212
- Sada, P. V., & Ramón-Fox, F. G. 2016, *PASP*, 128, 024402
- Schneider, J., Dedieu, C., Le Sidaner, P., Savalle, R., & Zolotukhin, I. 2011, *A&A*, 532, A79
- Simon, A. E., Szabó, G. M., Kiss, L. L., Fortier, A., & Benz, W. 2015, arXiv:1508.00321
- Smith, C.-T. W., Smart, B., Turner, J. D., et al. 2012, in *American Astronomical Society Meeting Abstracts* 220, 129.04
- Southworth, J. 2011, *MNRAS*, 417, 2166
- Southworth, J. 2012, *MNRAS*, 426, 1291
- Southworth, J., Hinse, T. C., Burgdorf, M., et al. 2014, *MNRAS*, 444, 776
- Southworth, J., Mancini, L., Novati, S. C., et al. 2010, *MNRAS*, 408, 1680
- Sozzetti, A., Torres, G., Charbonneau, D., et al. 2009, *ApJ*, 691, 1145
- Thakur, P., Jiang, I.-G., Yeh, L.-C., et al. 2013, in *Astronomical Society of India Conf. Ser.* 9, 78
- Todorov, K. O., Deming, D., Knutson, H. A., et al. 2013, *ApJ*, 770, 102
- Torres, G., Bakos, G. Á, Kovács, G., et al. 2007, *ApJL*, 666, L121
- Torres, G., Fischer, D. A., Sozzetti, A., et al. 2012, *ApJ*, 757, 161
- Turner, J., Hardegree-Ullman, K., Smart, B., et al. 2011, in *American Astronomical Society Meeting Abstracts* 128, 128.11
- Turner, J. D., Smart, B. M., Hardegree-Ullman, K. K., et al. 2013, *MNRAS*, 428, 678
- Vaňko, M., Jakubík, M., Krejčová, T., et al. 2012, in *IAU Symp.* 282, ed. M. T. Richards & I. Hubeny, 135
- Velasco, S., Etxegarai, U., Oscoz, A., et al. 2016, *Proc. SPIE*, 990820
- Velasco, S., Oscoz, A., López, R. L., et al. 2017, in *Highlights on Spanish Astrophysics IX, Proc. XII Scientific Meeting of the Spanish Astronomical Society*, ed. S. Arribas et al., 707
- Vidotto, A. A., Jardine, M., & Helling, C. 2011, *MNRAS*, 414, 1573
- Vogt, S. S., Allen, S. L., Bigelow, B. C., et al. 1994, *Proc. SPIE*, 2198, 362
- Walker-LaFollette, A., Turner, J. D., Hardegree-Ullman, K. K., et al. 2012, in *American Astronomical Society Meeting Abstracts* 219, 339.09
- Wheatley, P. J., Pollacco, D. L., Queloz, D., et al. 2013, *European Physical Journal Web of Conferences*, 47, 13002

B. CMFA

La Campaña Mexicana de Fotometría de Asteroides (CMFA) unió diferentes instituciones y observatorios para observar coordinadamente asteroides específicos. Cabe mencionar que el estudio de cuerpos menores del sistema solar es una rama joven en México, siendo que es uno de los principales temas de investigación actual en la astronomía internacional. Este proyecto ayudó a fomentar el interés en esta rama. En su primera etapa, la CMFA se enfocó en calcular los periodos de rotación utilizando mediciones en diferentes filtros. En algunos casos se reporta la primera estimación del periodo, se confirman mediciones previas o se aclaran discrepancias entre distintos reportes. También se observó variabilidad en la curva de luz durante nuestras observaciones para un objeto.

Realicé las observaciones del OAN-SPM incluidas en el primer reporte y algunas del segundo; instruí a uno de los observadores y participé en las discusiones desde la planeación de la campaña.

- Harris, A.W., Young, J.W., Bowell, E., Martin, L.J., Millis, R.L., Poutanen, M., Scaltriti, F., Zappala, V., Schober, H.J., Debehogne, H., Zeigler, K.W. (1989). "Photoelectric Observations of Asteroids 3, 24, 60, 261, and 863." *Icarus* **77**, 171-186.
- Harris, A.W., Pravec, P., Galad, A., Skiff, B.A., Warner, B.D., Vilagi, J., Gajdos, S., Carbognani, A., Hornoch, K., Kusnirak, P., Cooney, W.R., Gross, J., Terrell, D., Higgins, D., Bowell, E., Koehn, B.W. (2014). "On the maximum amplitude of harmonics on an asteroid lightcurve." *Icarus* **235**, 55-59.
- Higgins, D., Pravec, P., Kusnirak, P., Hornoch, K., Brinsfield, J.W., Allen, B., Warner, B.D. (2008). "Asteroid Lightcurve Analysis at Hunters Hill Observatory and Collaborating Stations: November 2007 - March 2008." *Minor Planet Bull.* **35**, 123-126.
- Hudson, R.S., Ostro, S.J. (1999). "Physical Model of Asteroid 1620 Geographos from Radar and Optical Data." *Icarus* **140**, 369-378.
- Koehn, B.W., Bowell, E.L.G., Skiff, B.A., Sanborn, J.J., et al. (2014). "Lowell Observatory Near-Earth Asteroid Photometric Survey (NEAPS) - 2009 January through 2009 June." *Minor Planet Bull.* **41**, 286-300.
- Polishook, D. (2009). "Lightcurves and Spin Periods from the Wise Observatory: 2008 August - 2009 March." *Minor Planet Bull.* **36**, 104-107.
- Pravec, P., Hergenrother, C., Whiteley, R., Sarounova, L., Kusnirak, P. (2000). "Fast Rotating Asteroids 1999 TY2, 1999 SF10, and 1998 WB2." *Icarus* **147**, 477-486.
- Pravec, P., Harris, A.W., Scheirich, P., Kušnirák, P., Šarounová, L., Hergenrother, C.W., Mottola, S., Hicks, M.D., Masi, G., Krugly, Yu.N., Shevchenko, V.G., Nolan, M.C., Howell, E.S., Kaasalainen, M., Galád, A., Brown, P., Degraff, D.R., Lambert, J.V., Cooney, W.R., Foglia, S. (2005a). "Tumbling asteroids." *Icarus* **173**, 108-131.
- Pravec, P., Scheirich, P., Durech, J., Pollock, J., Kusnirak, P., Hornoch, K., Galad, A., Vokrouhlicky, D., Harris, A.W., Jehin, E., Manfroid, J., Opitom, C., Gillon, M., Colas, F., Oey, J., Vrstil, J., Reichart, D., Ivarsen, K., Haislip, J., LaCluyze, A. (2014). "The tumbling state of (99942) Apophis." *Icarus* **233**, 48-60.
- Pravec, P., Wolf, M., Sarounova, L. (1999web, 2001web, 2005web, 2011web). <http://www.asu.cas.cz/~ppravec/neo.htm>
- Skiff, B.A., Bowell, E., Koehn, B.W., Sanborn, J.J., McLelland, K.P., Warner, B.D. (2012a). "Lowell Observatory Near-Earth Asteroid Photometric Survey (NEAPS) - 2008 May through 2008 December." *Minor Planet Bull.* **39**, 111-130.
- Thomas, C.A., Emery, J.P., Trilling, D.E., Delbo, M., Hora, J.L., Mueller, M. (2014). "Physical characterization of Warm Spitzer-observed near-Earth objects." *Icarus* **228**, 217-246.
- Warner, B.D. (2007). "Initial Results of a Dedicated H-G Program." *Minor Planet Bull.* **34**, 113-119.
- Warner, B.D., Harris, A.W., Pravec, P. (2009). "The Asteroid Lightcurve Database." *Icarus* **202**, 134-146. Last update: 2015 Dec. <http://www.minorplanet.info/lightcurvedatabase.html>
- Warner, B.D. (2013). "Seeing Double Old and New: Observations and Lightcurve Analysis at the Palmer Divide Observatory of Six Binary Asteroids." *Minor Planet Bull.* **40**, 94-98.
- Warner, B.D. (2014). "Near-Earth Asteroid Lightcurve Analysis at CS3-Palmer Divide Station: 2014 January-March." *Minor Planet Bull.* **41**, 157-168.
- Warner, B.D. (2015). "Near-Earth Asteroid Lightcurve Analysis at CS3-Palmer Divide Station: 2015 March-June." *Minor Planet Bull.* **42**, 256-266.
- Warner, B.D. (2016). "Near-Earth Asteroid Lightcurve Analysis at CS3-Palmer Divide Station: 2015 June-September." *Minor Planet Bull.* **43**, 66-79.
- Zappala, V., Cellini, A., Barucci, A.M., Fulchignoni, M., Lupishko, D.E. (1990). "An analysis of the amplitude-phase relationship among asteroids." *Astron. Astrophys.* **231**, 548-560.

RESULTS OF THE 2015 MEXICAN ASTEROID PHOTOMETRY CAMPAIGN

Pedro V. Sada
Departamento de Física y Matemáticas
Universidad de Monterrey
Av. I. Morones Prieto 4500 Pte.
Garza García, N.L., 66238
MÉXICO
pedro.valdes@udem.edu

Samuel Navarro-Meza & Mauricio Reyes-Ruiz
Instituto de Astronomía
Universidad Nacional Autónoma de México
Ensenada, Baja California, MÉXICO

Lorenzo L. Olguín, Julio C. Saucedo & Pablo Loera-González
Depto. de Investigación en Física
Universidad de Sonora
Hermosillo, MÉXICO

(Received: 2016 January 9)

The 2015 Mexican Asteroid Photometry Campaign was organized at the 2nd National Planetary Astrophysics Workshop held in 2015 March at the Universidad Autónoma de Nuevo León in Monterrey, México. Three asteroids were selected for coordinated observations from several Mexican observatories. We report full lightcurves for the main-belt asteroid 1084 Tamariwa ($P = 6.195 \pm 0.001$ h) and near-Earth asteroid (NEA) 4055 Magellan ($P = 7.479 \pm 0.001$ h). Asteroid 1466 Mundleria was also observed on eight nights but no lightcurve was obtained because of its faintness, a crowded field-of-view, and low amplitude (<0.03 mag).

Planetary astronomy in general is becoming a more popular field of scientific study in Mexico, in part due to the recent establishment of the Mexican Space Agency (<http://www.aem.gob.mx/>). As a consequence, the Universidad Autónoma de Nuevo León, in the city of Monterrey, organized a series of National Planetary Astrophysics Workshops. The first was in 2013 and the second in 2015 (<http://tasp.fcfm.uanl.mx/>).

Astronomers from all over México were invited to present their research and encouraged to cooperate and plan projects related to the study of Solar System objects or extrasolar planets.

One of the results from the latest meeting was the organization of the 2015 Mexican Asteroid Photometry Campaign (<http://www.astro.uson.mx/~lorenzo/CMFA2015/CMFA2015>). The objective of this first campaign was to organize, coordinate, and share photometric observations of asteroids between interested parties at various national observatories and university research centers. Because asteroid photometry is not a common activity amongst Mexican astronomers, it was decided as a first effort to form individual observing groups that would start to develop their own expertise in the matter by observing relatively simple targets.

Three asteroids were chosen: the C-class main-belt asteroid 1084 Tamariwa has a well-defined period, large amplitude, and is relatively bright. 1466 Mundleria, another C-class inner-belt asteroid, is a smaller and dimmer target with an unknown rotation period. 4055 Magellan was also selected since the V-type Amor asteroid would have a favorable opposition during 2015.

We present the results of this first Mexican Asteroid Photometry Campaign. In all we collected 18 nights of observations from three different observatories and managed to reconstruct full lightcurves for 1084 Tamariwa and 4055 Magellan. 1466 Mundleria turned out to be a more difficult target to observe and analyze since it was dim, in a crowded field of stars, and apparently exhibits a very small brightness amplitude variation.

At the Universidad de Monterrey (UdeM) Observatory (MPC 720) we observed all three asteroids on 10 different nights using a Meade 0.36-m $f/8$ LX-600GPS telescope and an SBIG STL-1301E CCD. The camera contains a 1280×1024 - $16\mu\text{m}$ KAF-1301E/LE chip which covers a $\sim 26.3 \times 21.1$ arcminute field-of-view (FOV) with an image scale of about 1.25 arcseconds/pixel. All asteroids were observed unfiltered and exposures were set for each target as follows: 40 seconds for fast-moving 4055 Magellan, 60 seconds for 1084 Tamariwa, and 120 seconds for dim 1466 Mundleria. The CCD images were read in 2×2 binned format for faster download time and improved observing efficiency. The FOV was maintained fixed in the chip by using a guide star at all times.

Two observing runs were scheduled with the 0.84-m $f/15$ Ritchey-Chretien telescope at the Observatorio Nacional de San Pedro Mártir (SPM; MPC 679) in Baja California for this program. This telescope uses a $2048 \times 2048 \times 13.5\mu\text{m}$ Spectral Instruments CCD for regular imaging. This combination yields a FOV of $\sim 6.3 \times 6.3$ arcminutes with an approximate image scale of 0.185 arcsecond/pixel. 1084 Tamariwa was observed for only one night on the first observing run in May, while 4055 Magellan was observed for three nights and 1466 Mundleria for two nights on the second observing run in August. All images were obtained using an off-axis guide star for stability (although the field drifted a bit during the observing sessions) and were also unfiltered and binned 2×2 for efficiency. Exposure times varied for each target: 30 and 45 seconds for 4055 Magellan, 90 and 120 seconds for 1466 Mundleria, and 60 seconds for 1084 Tamariwa.

One observing night for 1084 Tamariwa and two for 1466 Mundleria were recorded at the Carl Sagan Observatory belonging to the Universidad de Sonora in Hermosillo. The observatory operates a Meade LX-200 0.41-m $f/10$ telescope equipped with a $2499 \times 2499 \times 12\mu\text{m}$ Apogee Alta F9000 CCD for imaging. This yields a 25.4×25.4 arcminute FOV with an image scale of ~ 0.61 arcsecond/pixel. The images at this site were obtained unguided,

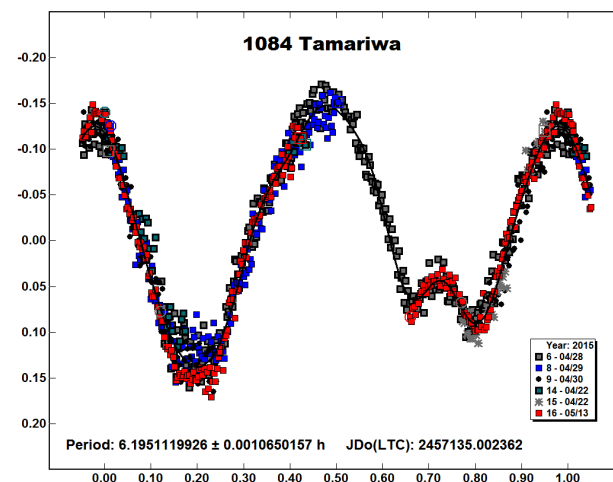
unfiltered and – in this case – unbinned. Exposure times were 20 seconds for 1084 Tamariwa and 50 seconds for 1466 Mundleria.

All the data were concentrated at the Universidad de Monterrey Observatory where the photometric analysis was performed using *MPO Canopus* (version 9.5.0.14). Images were also processed in the standard manner using nightly dark current and flat-field files from each site.

1084 Tamariwa. This asteroid was observed at the Carl Sagan Observatory (2015 April 22), Universidad de Monterrey Observatory (2015 April 28-30), and San Pedro Mártir Observatory (2015 May 13). During analysis, the April 22 observations from Carl Sagan Observatory were treated as two separate sessions due to re-centering the FOV during the night.

The asteroid was previously observed and reported by Behrend *et al.* (2007), Stecher *et al.* (2008), and Sada (2008). Our observations confirm the period of 6.195 ± 0.001 h, amplitude ~ 0.30 magnitudes, and general lightcurve shape presented in Sada (2008).

The similarity of both lightcurves obtained at different opposition dates (2007 August 19 and 2015 April 21) would suggest a rotational axis alignment perpendicular to the ecliptic, although too few complete lightcurves are available for a full polar orientation and shape analysis. We note in particular that the main minimum (without the “hump”) exhibits a large scatter in both the 2007 and 2015 lightcurves. We are uncertain as to its origin but it might be associated with topographical features sensitive to slight variations in phase angle illumination.



As an aside, initial analysis of the April 28 observations at the Universidad de Monterrey Observatory found the intended comparison star, GSC 5553-0670 (magnitude ~ 13.4), to be variable. It was discarded for the asteroid measurements but follow-up analysis found a sinusoidal lightcurve of short period. We plan to obtain more data and report the results to the AAVSO. This serves both as a warning to make sure comparison stars are not variable and a reminder that asteroid images can be data mined for other objects.

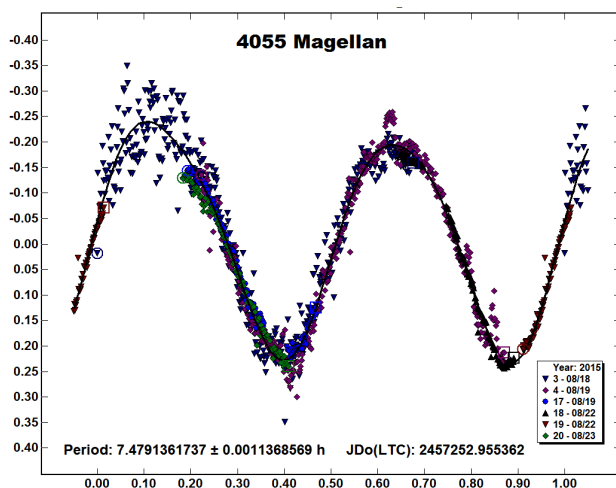
1466 Mundleria. This asteroid was observed for four nights at the Universidad de Monterrey Observatory (2015 July 25 and 27 and August 6-7), two nights at the San Pedro Mártir Observatory (2015 August 20-21), and two nights at the Carl Sagan Observatory (2015 June 15-16). Despite being the most observed asteroid in the

set, no conclusive brightness variations larger than 0.03 magnitudes could be detected over a single observing session. Therefore, no rotational period could be derived. This small (~22 km.) asteroid was the faintest in our set and, at the time, was also crossing a dense star field in Ophiuchus. These circumstances combined to make the data reduction difficult, even with the star eliminating option in *MPO Canopus*, and yielded relatively large scatter for the smaller UdeM and Carl Sagan Observatory telescopes. The SPM data were of much better quality but sparser. Nevertheless, it was useful to set our magnitude variation upper limit. No other reports for this asteroid were found. A larger aperture instrument and more patience are required to derive a lightcurve for this asteroid.

4055 Magellan. This NEA was observed for three nights at the Universidad de Monterrey Observatory (2015 August 14, 18-19) and three more nights at the San Pedro Mártir Observatory (2015 August 19, 22-23). The derived lightcurve exhibits similar maxima and minima with a period of 7.479 ± 0.001 hours and a relatively large amplitude of ~0.45 magnitudes. The August 19 data were acquired independently at both the UdeM and SPM observatories. The August 22 SPM data were analyzed as two separate sessions because of recentering of the FOV due to the asteroid's fast sky motion.

Our August 18 UdeM data show large scatter due to weather but assure full lightcurve phase coverage. The August 14 UdeM data exhibited even larger scatter and were omitted from the period and lightcurve shape calculations even though its general outline does corroborate our derived final lightcurve.

This asteroid has been observed several times. Warner (2014) suggests a period of ~6.384 hours from sparse 2004 data over a 7.475-hour period initially proposed by Pravec *et al.* (2000). However, older observations reported in Waszczak *et al.* (2015) and observations from the current 2015 opposition by Warner (2015) and Behrend *et al.* (2015) favor the later ~7.5-hour period. Our results are consistent with this period estimate, amplitude and general lightcurve shape.



Future Mexican Asteroid Photometry Campaigns are being planned with an increasing number of proposed targets (main-belt asteroids and NEAs) and participation from other Mexican observatories. We are also working on standardizing the observing sequences and data reduction and analysis techniques to make the data easier to share and publish.

Acknowledgments

The results presented in this report were partially based on observations acquired at the Observatorio Astronómico Nacional in the Sierra San Pedro Mártir (OAN-SPM), Baja California, México. We also would like to thank Ricardo López-Valdivia for his aid during the OAN-SPM August observations.

References

- Behrend, R. (2007, 2015). "Asteroids and Comets Rotation Curves, CdR." http://obswww.unige.ch/~behrend/page_cou.html
- Pravec, P., Wolf, M. Sarounova, L. (2000). "Ondrejov Asteroid Photometry Project." <http://www.asu.cas.cz/~ppravec/neo.htm>
- Sada, P.V. (2008). "Lightcurve Analysis of 1084 Tamariwa." *Minor Planet Bulletin* **35**, 50.
- Stecher, G., Ford, L., Lorenzen, K., Ulrich, S. (2008). "Photometric Measurements of 1084 Tamariwa at Hobbs Observatory." *Minor Planet Bulletin* **35**, 76-77.
- Warner, B.D. (2014). "Near-Earth Asteroid Lightcurve Analysis at CS3-Palmer Divide Station: 2014 January-March." *Minor Planet Bulletin* **41**, 157-168.
- Warner, B.D. (2015). "Near-Earth Asteroid Lightcurve Analysis at CS3-Palmer Divide Station: 2015 March-June." *Minor Planet Bulletin* **42**, 256-266.
- Waszczak, A., Chang, C.-K., Ofek, E.O., Laher, R., Masci, F., Levitan, D., Surace, J., Cheng, Y.-C., Ip, W.-H., Kinoshita, D., Helou, G., Prince, T.A., Kulkarni, S. (2015). "Asteroid Lightcurves from the Palomar Transient Factory Survey: Rotation Periods and Phase Functions from Sparse Photometry." *Astron. J.* **150**, id. 75.

PHOTOMETRY OF ASTEROIDS 2014 EK14 AND 2015 FS332 AT THE TERSKOL OBSERVATORY

Vira Godunova, Volodymyr Reshetnyk, Maxim Andreev
ICAMER Observatory of NASU (MPC B18)
27 Acad Zabolotnoho Str.
Kyiv 03680 UKRAINE
V_Godunova@bigmir.net

Andrii Simon, Volodymyr Vasylenko
Taras Shevchenko National University of Kyiv
Kyiv, UKRAINE

(Received: 2016 January 15)

We report photometric observations of two near-Earth asteroids that were obtained with the Zeiss-600 telescope at the Terskol Observatory in 2015. Based on our data, we were able to estimate the rotation properties of these asteroids.

Starting in 2003, the facilities of the Terskol Observatory in the Northern Caucasus (43°16'29" N, 42°30'03" E, 3120 m ASL) have

RESULTS OF THE 2016 MEXICAN ASTEROID PHOTOMETRY CAMPAIGN

Pedro V. Sada

Departamento de Física y Matemáticas
 Universidad de Monterrey
 Av. I. Morones Prieto 4500 Pte.
 San Pedro Garza García, N.L. 66238
 MÉXICO
pedro.valdes@udem.edu

Lorenzo Olguín, Julio C. Saucedo & Pablo Loera-González
 Departamento de Investigación en Física
 Universidad de Sonora
 Hermosillo, Sonora, MÉXICO

Laura Cantú-Sánchez, Jaime R. Garza, Sandra A. Ayala-Gómez
 Andrés Avilés & Eduardo Pérez-Tijerina
 Facultad de Ciencias Físico-Matemáticas
 Facultad de Ingeniería Mecánica y Eléctrica
 Universidad Autónoma de Nuevo León
 Monterrey, Nuevo León, MÉXICO

Samuel Navarro-Meza, J. S. Silva & Mauricio Reyes-Ruiz
 Instituto de Astronomía
 Universidad Nacional Autónoma de México
 Ensenada, Baja California, MÉXICO

Juan Segura-Sosa
 Facultad de Ciencias Físico-Matemáticas
 Universidad Autónoma de Coahuila
 Saltillo, Coahuila, MÉXICO

Ricardo López-Valdivia
 Área de Astrofísica
 Instituto Nacional de Astrofísica, Óptica y Electrónica
 Tonantzintla, Puebla, MÉXICO

F. Álvarez-Santana
 Área de Astrofísica
 Universidad Autónoma de Baja California
 Ensenada, Baja California, MÉXICO

(Received: Revised:)

We report the results of the 2016 Mexican Asteroid Photometry Campaign. This year observers from seven different research institutions carried out 34 nights of observations at three Mexican observatories. An uncertain, but long, period of $\sim 115.108 \pm 0.014$ h was estimated for 703 Noëmi from sparse data. A nearly-complete lightcurve was obtained for 1305 Pongola ($P = 8.0585 \pm 0.0003$ h). Asteroid 2535 Hämeenlinna turned out to be a binary system where the primary exhibits a rotation period of 3.2311 ± 0.0001 h and the secondary shows an orbital period of 21.20 ± 0.004 h. Asteroid 4775 Hansen ($P = 3.1186 \pm 0.0001$ h) was well observed and showed variations of its lightcurve between two sets of observations separated by about 6 weeks.

After the successful start of the Mexican Asteroid Photometry Campaign in 2015 with the coordinated observation of three asteroids from three different Mexican observatories (Sada et al. 2016), it was decided to continue and seek to increase the collaboration during 2016. The eventual goal of this effort is to develop teams of coordinated observers in México capable of

characterizing not only main belt asteroids, but NEOs as well. We report here the results of the 2016 Mexican Asteroid Photometry Campaign.

On this occasion, we collected 34 nights of observations from three different observatories by researchers from seven different institutions. On three of those nights the observing session was carried out simultaneously from two separate observatories, providing a basis for photometric comparison between them and prolonging the observing period for the target since the observatories were separated by more than 10° in longitude.

At the Universidad de Monterrey (UdeM) Observatory (MPC 720) we observed four asteroids on 17 different nights using a Meade 0.36-m f/8 LX-600GPS telescope and an SBIG STL-1301E CCD. The camera uses a 1280×1024 - $16\mu\text{m}$ KAF-1301E/LE chip which covers a $\sim 26.3 \times 21.1$ arcmin field-of-view (FOV) with an image scale of about 1.24 arcsec/pix. All asteroids were observed unfiltered for maximum throughput, and the CCD images were read in 2×2 binned format for faster download time and improved observing efficiency. The FOV was maintained fixed on the chip by using an on-axis guide star at all times. Exposure times varied between 60s and 210s for each night depending on the target's brightness, and sometimes a slight defocus was applied to the telescope to spread the images over a few binned pixels allowing for slightly longer exposure times.

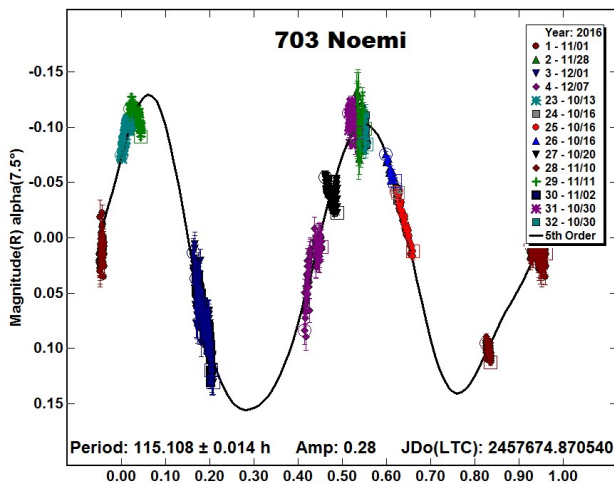
Three one-week observing runs were scheduled throughout the year with the 0.84-m f/15 Ritchey-Chretien telescope at the Observatorio Astronómico Nacional on the Sierra de San Pedro Mártir (OAN-SPM; MPC 679) in Baja California for this program. On top of that, a few additional partial nights of observations were attained on an availability basis from other observing runs. This telescope uses a 2048×2048 - $13.4\mu\text{m}$ Spectral Instruments CCD for regular imaging. This combination yields a FOV of $\sim 6.3 \times 6.3$ arcmin with an approximate image scale of 0.185 arcsec/pix. All images were obtained using an off-axis guide star for stability (although the field drifted a little during the observing sessions due to telescope sag), were obtained unfiltered, and were also binned 2×2 for efficiency. Exposure times also varied for each asteroid, between 20s and 480s, depending on the target brightness.

Five observing nights were also recorded at the Carl Sagan Observatory belonging to the Universidad de Sonora (UNISON) in Hermosillo. This observatory operates a Meade LX-200GPS 0.41-m f/10 telescope equipped with a $3056 \times 3056 \times 12\mu\text{m}$ Apogee Alta F9000 CCD for imaging. The image frame was trimmed to a subframe of 2000×2000 pixels and then binned 2×2 yielding an effective $\sim 20 \times 20$ arcmin FOV with an image scale of about 1.2 arcsec/pix. The images at this site were obtained unguided and unfiltered. Exposure times varied between 70s and 240s.

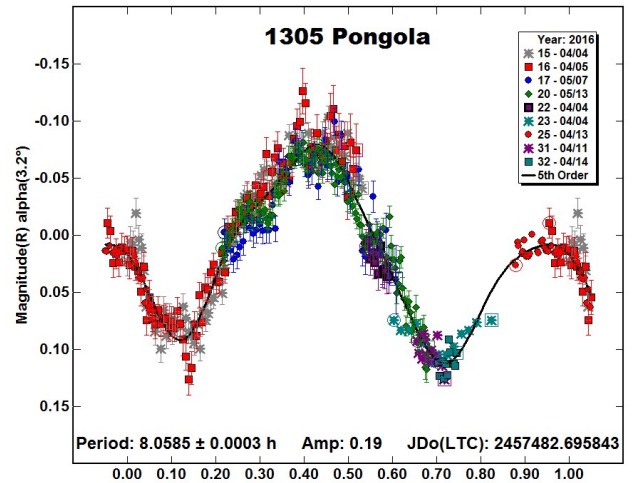
Images from these observatories were processed in the standard manner using nightly dark current and flat-field files. Photometric measurements and lightcurve analysis were performed using MPO Canopus (version 10.7.3.0). Although all observations were unfiltered, differential magnitudes were calculated based on R-band stellar magnitudes.

703 Noëmi. Was discovered by Johann Palisa on 1910 October 3 and named for Baroness Valentine Noëmi von Rothschild (Schmadel, 2003). This S-class asteroid from the Flora Family was observed on five nights from the OAN-SPM Observatory (2016 Oct 13, 16, 20 & Nov 10, 11), four nights from the UDEM Observatory (2016 Nov 1, 28 & Dec 1, 7) and two nights at the UNISON Observatory (2016 Oct 30 & Nov 2). The 2016 Oct 16 observations were treated as three separate sessions because of differences in exposure times. The 2016 Oct 30 observations were treated as two

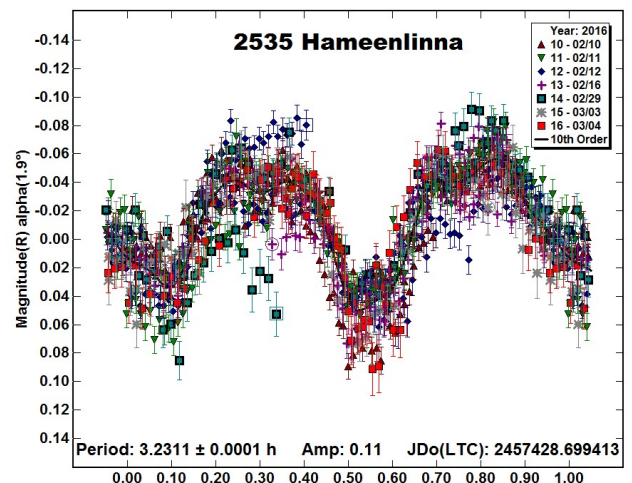
separate sessions because the FOV was slightly rotated partway through the night. Initial results showed that the asteroid brightness varied a small amount during each night, suggesting either a long rotation period and/or low amplitude. We derived a tentative long rotation period of 115.108 ± 0.014 h by matching the observations from 2016 Nov 2 and Dec 1 in the phased lightcurve, because they exhibited almost identical behavior, and then looking for other possible matches using whole fractions of that time-span and assuming a simple two-maxima and two minima lightcurve. The fact that differential photometry was performed on the unfiltered images, which meant that we could also shift the nightly observations in the brightness axis, added too many degrees of freedom in the search of a solution. Thus, we can only state that the rotation period for this asteroid is long, in the realm of tens of hours, and that our derived tentative value is only one possible solution. Our sparse observations are insufficient to cover an entire lightcurve. No other reports of the rotation period were found in the literature for this asteroid. However, A. Noschese reports in the Collaborative Asteroid Lightcurve Link (CALL) website (<http://www.minorplanet.info/call.html>) a larger set of observations from his group that indicates a longer period of $\sim 201.9 \pm 0.8$ h, also with larger amplitude. Most of our observations predate his earliest observing date and there is little overlap, so this would be a good opportunity to join both data sets in an effort to obtain a more reliable solution to the rotation period of 703 Noëmi.



1305 Pongola. Was discovered on 1928 July 19 by H. E. Wood at Johannesburg and named for a river in South Africa (Schmadel, 2003). This C-class outer main-belt asteroid was observed at the UdeM Observatory on three nights (2016 Apr 4, 5 & May 7) and at OAN-SPM Observatory on five (2016 April 4, 11, 13, 14 & May 13). During analysis, the 2016 April 4 observations were treated as three separate sessions because of differences in exposure times of the image sets and because they were obtained at two separate observatories. The April 11, 13 and 14 observing sessions were short, obtained during time gaps of other assigned projects, but still provided useful data to complement the lightcurve. A total of 457 data points was used to find a period of 8.0585 ± 0.0003 h with an amplitude of ~ 0.19 mag. Initial rotation period determinations were made by Binzel (1987), 8.03 ± 0.10 h; and Ditteon *et al.* (2012), 8.06 ± 0.02 h. More recently, Waszczak *et al.* (2015) reported a rotation period of 8.0586 ± 0.0015 h with an amplitude of 0.17mag, while Mansego *et al.* (2016) reported a period of 8.335 ± 0.002 h with an amplitude of 0.16mag. Our resulting period and amplitude are in better agreement with those obtained by Waszczak *et al.* (2015).

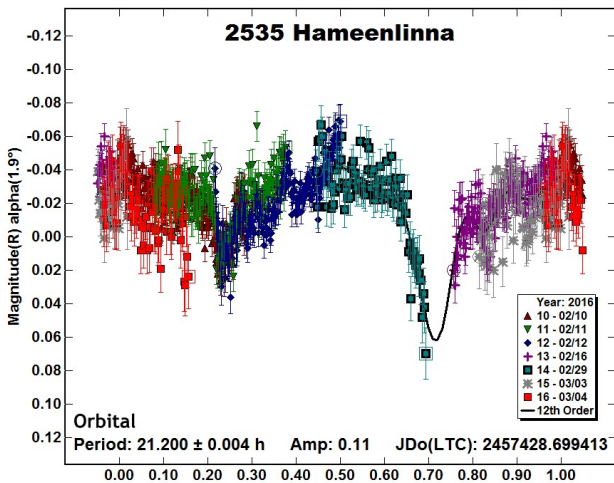
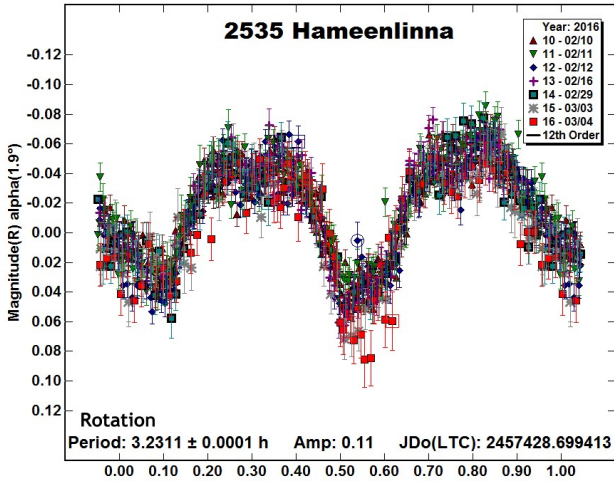


2535 Hämeenlinna. Was discovered in 1939 February 17 by Y. Väisälä at Turku and named for an old town in the province of Häme (Schmadel, 2003). This S-class asteroid from the Flora Family was observed at the UdeM Observatory on eight nights (2016 Feb 10, 11, 12, 16, 29 & Mar 3, 4, 13). On two of these nights (2016 Feb 11 & Mar 3) the asteroid was also observed from the UNISON Observatory, extending the nightly observing period because of its location further west. For the final analysis, the night of 2016 Mar 13 was not included as it was much noisier than the rest. From the onset, this asteroid exhibited a clear ~ 3.23 h period. However, each night the asteroid also exhibited a different overall trend in the data with each successive period not quite matching the previous ones. This was particularly evident in the two extended observing sessions from both observatories. The asteroid was thus suspected as having two periods and further observations were programmed until it was too faint to follow. The following figure below shows the best-fit single period obtained for the data. It confirms a 3.2311 ± 0.0001 h rotation period, but also exhibits larger than usual scatter.

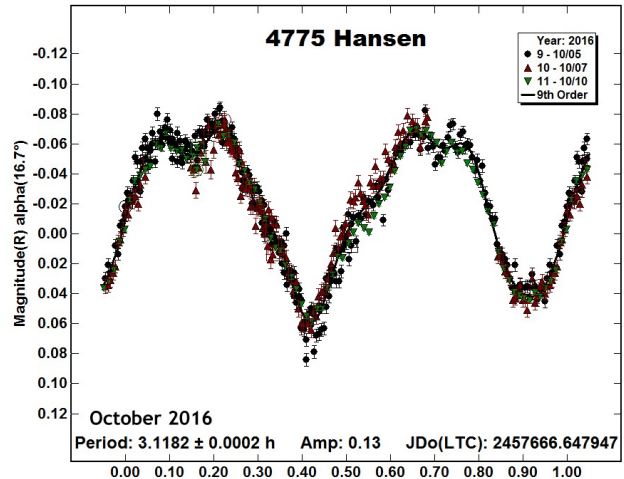
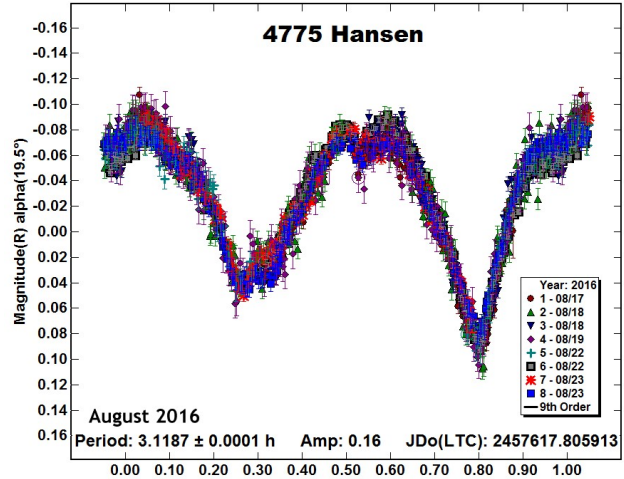


It was decided to use the dual period option included in MPO Canopus to attempt and disentangle the possibility of the existence of two periods. The results are shown in the following two figures. Our initial short rotation period of 3.2311 ± 0.0001 h with an amplitude of 0.11mag was maintained and the scatter was considerably reduced. An additional period of 21.20 ± 0.004 h with an amplitude of 0.11mag is also extracted from the data. This

second lightcurve exhibits what appear to be primary and secondary dimmings due to the possible presence of a small companion orbiting the asteroid. The secondary dimming was well sampled by our data, but not the primary. This renders the derived possible orbital period of the companion as tentative since other nearby periods could also fit the data, which has an overall scatter similar to the derived amplitude. The only other report about 2535 Hameenlinna found in the literature is from Benishek *et al.* (2016) in which they report that this asteroid is a binary system where the primary exhibits a rotation period of 3.23106 ± 0.00006 h, the secondary shows a synchronous orbital period of 21.23 ± 0.01 h, and the reported lightcurve amplitude is 0.10mag. They also register eclipse/occultation events with depths of 0.05-0.10mag. Our data independently confirms this preliminary report from Benishek *et al.* (2016).



of 0.12mag obtained by Warner (2017). We note that the lightcurve did show some variation in shape and amplitude between the observations performed the third week of August vs those performed the first week of October. The October data exhibits a noticeable decrease in amplitude, from 0.16mag to 0.13mag, suggesting a more pole-on view, as outlined by Warner (2017) from his 2016 November observations.



Acknowledgements

The results presented in this report were partially based on observations acquired at the Observatorio Astronómico Nacional on the Sierra de San Pedro Mártir, Baja California, México. Laura Cantú-Sanchez is working on her Master's Degree at the Planetary Astrophysics Program of the Universidad Autónoma de Nuevo León.

References

Benishek, V., Pray, D., Pravec, P., Kusnirak, P., Hornoch, K., Kucakova, H., Vrástil, J., Pollock, J., Groom, R., Stranger, K., Carbognani, A., Montaigut, R., Leroy, A., Reichart, D., Haislip, J. (2016). CBET 4262.
 Binzel, R.P. (1987). "A Photoelectric Survey of 130 Asteroids." *Icarus* 72, 135-208.

4775 Hansen. Was discovered in 1927 Oct 3 by Maximilian Franz Wolf at Heidelberg and named after the German astronomer Peter Andreas Hansen (Schmadel, 2003). This is a C-class asteroid that crosses the orbit of Mars. It was observed on six nights at the OAN-SPM Observatory (2016 Aug 17, 18, 19, 22, 23 & Oct 10) and two nights at the UDEM Observatory (2016 Oct 5, 7). During analysis, the 2016 Aug 22 and 23 observations were treated as two separate sessions. From all this data combined, we derive a period of 3.1186 ± 0.0001 h with an amplitude of 0.15mag. This is in general agreement with the results of $P = 3.1185 \pm 0.0001$ h and amplitude of 0.18mag obtained by Pravec et al. (2016web), but in slight disagreement with the results of $P = 3.124 \pm 0.001$ h and amplitude

Ditteon, R., Horn, L., Kamperman, A., Vorjohan, B., Kirkpatrick, E. (2012). "Asteroid Lightcurve Analysis at the Oakley Souther Sky Observatory: 2011 April-May." *Minor Planet Bulletin* **39**, 26-28.

Harris, A.W., Young, J.W., Scaltriti, F., Zappala, V. (1984). "Lightcurves and phase relations of the asteroids 82 Alkmene and 444 Gyptis." *Icarus* **57**, 251-258.

Mansego, E.A., Rodriguez, P.B., de Haro, J.L., Chiner, O.R., Silva, A.F., Porta, D.H., Martinez, V.M., Silva, G.F., Garcerán, A.C. (2016). "Eighteen Asteroids Lightcurves at Asteroides Observers (OBAS) – MPPD: 2016 March-May." *Minor Planet Bulletin* **43**, 332-336.

Pravec, P., Wolf, M., Sarounova, L. (2016). "Photometric Survey for Asynchronous Binary Asteroids." <http://www.asu.cas.cz/~asteroid/binastphotosurvey.htm>.

Sada, P.V., Navarro-Meza, S., Reyes-Ruiz, M., Olguín, L.L., Saucedo, J.C., Loera-González, P. (2016). "Results of the 2015 Mexican Asteroid Photometry Campaign." *Minor Planet Bulletin* **43**, 154-156.

Schmadel, L.D. (2003). *Dictionary of Minor Planet Names*, pp. 107, 171, 260, 328, 628. Springer, New York.

Warner, B.D., Harris, A.W., Pravec, P. (2009). "The Asteroid Lightcurve Database." *Icarus* **202**, 134-146. Updated 2016 Sep. <http://www.minorplanet.info/lightcurvedatabase.html>.

Warner, B.D. (2017). "Asteroid Lightcurve Analysis at CS3-Palmer Divide Station: 2016 October-December." *Minor Planet Bulletin* **44**, 116-120.

Waszczak, A., Chang, C.-K., Ofeck, E.O., Laher, R., Masci, F., Levitan, D., Surace, J., Cheng, Y.-C., Ip, W.-H., Kinoshita, D., Helou, G., Prince, T.A., Kulkarni, S. (2016). "Asteroid Light Curves from the Palomar Transient Factory Survey: Rotation Periods and Phase Functions from Sparse Photometry." *A. J.* **150**, A75.

Number	Name	2016 mm/dd	Pts	Phase	L _{PAB}	B _{PAB}	Period(h)	P.E.	Amp	A.E.	Grp
703	Noemi	10/13-12/07	1104	18.4,15.0	50	-1	115.108	0.014	0.28	0.05	FLO
1305	Pongola	04/04-05/13	457	3.2,12.4	202	2	8.0585	0.0003	0.19	0.02	MBO
2535	Hämeenlinna	02/10-03/04	940	1.9,12.3	143	-2	2.2311	0.0001	0.11	0.02	FLO
4775	Hansen	08/17-08/23	1511	19.5,16.4	342	-1	3.1187	0.0001	0.16	0.02	MC
4775	Hansen	10/05-10/10	507	16.7,18.8	5	12	3.1182	0.0002	0.13	0.02	MC

Table I. Observing circumstances and results. Pts is the number of data points. The phase angle is given for the first and last date. L_{PAB} and B_{PAB} are the approximate phase angle bisector longitude and latitude at mid-date range (see Harris *et al.*, 1984). Grp is the asteroid family/group (Warner *et al.*, 2009).

The Mexican Asteroid Photometry Campaigns: Aiming for Asteroids' Rotation Periods

W. J. Schuster¹, S. A. Ayala-Gómez², A. Avilés², M. E. Contreras³,
S. A. R. Haro-Corzo⁴, P. A. Loera-Gonzalez³, S. Navarro-Meza¹, L.
Olguín³, E. Pérez-Tijerina², M. Reyes¹, J.C. Saucedo³, J.
Segura-Sosa⁵, P. A. Valdés-Sada⁶, I. L. Fuentes-Carrera⁷, C.
Chávez-Pech², M. Rodríguez-Martínez⁴, & R. Vázquez¹

¹ IAEnsenada, Universidad Nacional Autónoma de México,
Km 107 Carretera Tijuana-Ensenada, Ensenada, B.C., Mexico
email: schuster@astro.unam.mx

²FCFM–Universidad Autónoma de Nuevo León, ³DIF–Universidad de Sonora,

⁴ENES–Universidad Nacional Autónoma de México, ⁵FCFM–Universidad Autónoma de Coahuila, ⁶DFM–Universidad de Monterrey, ⁷ESFM–Instituto Politécnico Nacional.

Abstract. Thousands of new asteroids are discovered every year and the rate of discovery is by far larger than the determination rate of their physical properties. In 2015 a group of researchers and students of several Mexican institutions, have established an observational program to study asteroids photometrically. The program, named Mexican Asteroid Photometry Campaign, is aiming to derive rotation periods of asteroids based on optical photometric observations. Since then four campaigns have been carried out. The results obtained throughout these campaigns, as well as future work, are presented.

Keywords. Solar system: general, minor planets, asteroids, techniques: photometry

1. Overview

Currently, more than 760,000 asteroids are known and every year thousands of new ones are discovered. Nevertheless, most of their physical parameters: size, shape, albedo, rotation, taxonomical classification, etc. are unknown. Thus, we need to make a greater effort to increase our knowledge about these objects. Some asteroid properties, such as their rotation period, can be derived from their lightcurve. However, according to the Asteroid Lightcurve Photometry Database (ALCDEF), only a few thousand (~6000) asteroids have reliable rotation periods. These periods are important because they are related to the cohesion strength of the material from which an asteroid has been made. Figure 1 shows the relation between the asteroid rotation frequency and its size. We can see that fast rotators have sizes smaller than ~300 m. In addition, 3D asteroid shapes can be inferred from lightcurves obtained at different epochs, since objects are observed from different viewing angles.

In order to contribute to asteroid characterization, in 2015 a group of researchers and students of several Mexican institutions, have established an observational program to study asteroids photometrically. The program, named Mexican Asteroid Photometry Campaign (CMFA, from the Spanish), is aiming to derive rotation periods of asteroids based on optical photometric observations. This program has been established at an introductory stage to generate the abilities and basic knowledge related to asteroids,

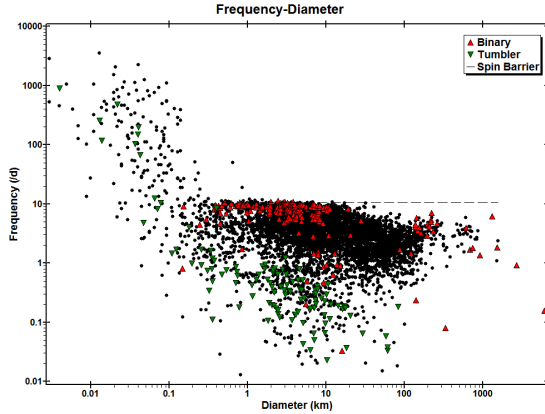


Figure 1. Relation between the asteroid rotation frequency and its size. Figure taken from the ALCDEF web site.

allowing us to carry out broader and deeper studies in the near future. The first campaign started during the second half of 2015. Since then, three campaigns have been completed and the fourth is ongoing.

2. Observations, data reduction, analysis and results

The observatories and telescopes involved in the campaigns are the following: i) 0.84-m telescope at the Observatorio Astronómico Nacional at Sierra San Pedro Mártir (OAN-SPM), operated by Universidad Nacional Autónoma de México, at Baja California, ii) 0.40-m telescope at Observatorio Astronómico Carl Sagan (OACS), Universidad de Sonora, Hermosillo, Sonora, and iii) 0.36-m telescope of the Universidad de Monterrey Astronomical Observatory, Monterrey, Nuevo León.

Typically, to obtain complete lightcurves, five to ten nights of observation are dedicated to each asteroid. Exposure times for individual images are in the range of 30 to 240 seconds, depending on asteroid’s visual magnitude. Generally, a few hundred images per object are taken during each observing night.

Basic steps in data reduction are performed using IRAF or MaximDL software. For lightcurve extractions and period determinations, MPO Canopus software is used. For crowded stellar fields, first DAOPHOT (Stetson 1987) is used to obtain the photometry and then MPO Canopus is used for deriving the lightcurve and rotation period. Figure 2 shows examples of lightcurves derived using these procedures.

The asteroid sample has been obtained from the Collaborative Asteroids Lightcurve Link (CALL). In general, asteroids with poorly, or unknown, rotation periods were chosen. Only those with declinations $> -30^\circ$ were observed. In three years more than fifty objects have been observed in four campaigns from which a dozen lightcurves and rotation periods have been published (Sada *et al.* 2016; Sada *et al.* 2017; Sada *et al.* 2018; Haro-Corzo *et al.* 2018). Some data are still under analyses. A sample of derived rotation periods and relevant information are presented in Table 1. Near Earth Asteroids’ (NEAs’) information is not included because it has been presented in a separate contribution by J.C. Saucedo et al. at this same IAU Focus Meeting.

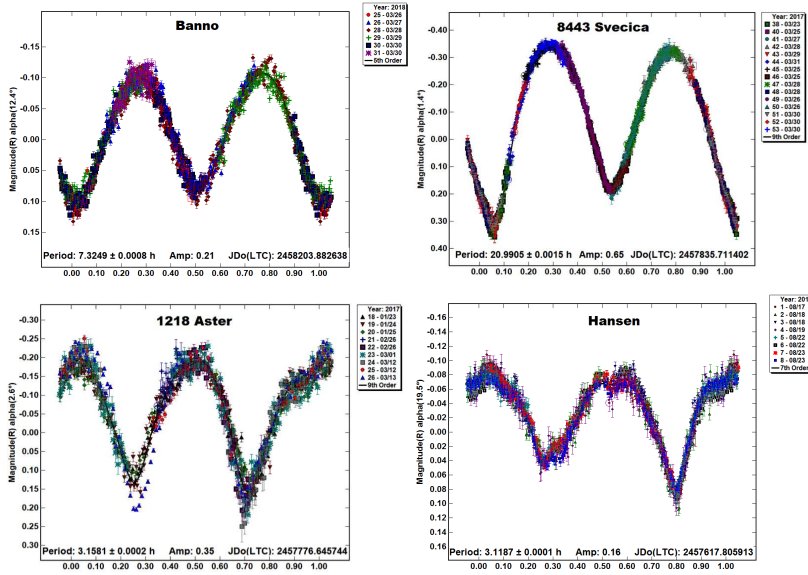


Figure 2. Examples of asteroids' phased lightcurves.

Table 1. Asteroids with reliable period determinations.

Name	Period (h)	Error (h)	Amplitude (mag)	Nights	Group
703 Noemi	11.108	0.014	0.28	11	Flora
1084 Tamariwa	6.195	0.001	0.30	5	Outer Main Belt
1218 Aster	3.1581	0.0002	0.35	7	Flora
1305 Pongola	4.349	0.0003	0.19	8	Outer Main Belt
1491 Balduinus	15.3044	0.0057	0.45	4	Outer Main Belt
1856 Ruzena	5.957	0.001	0.68	11	Main Belt
2022 West	14.1385	0.0031	0.54	7	Outer Main Belt
2535 Hameenlinna	3.2311	0.0001	0.11	10	Flora
2733 Hamina	93.23	0.02	0.36	13	Inner Main Belt
3394 Banno	7.3249	0.0008	0.21	5	Main Belt
3887 Braes	5.81	0.01	0.60	6	Main Belt
4775 Hansen	3.1186	0.0001	0.15		Mars Crossing
8433 Svecica	20.9905	0.0015	0.65	10	Outer Main Belt
18301 Konyukhov	2.6667	0.0003	0.15	6	Outer Main Belt

3. Concluding remarks and future work

After three years we have refined observational and analysis methods to derive reliable asteroids' lightcurves. The pace at which we are obtaining and processing photometric data is increasing. However, due to the shortage of trained people, we are reaching our maximum rate of studied objects to about 12 objects per year. Therefore, we are planning to coach a new generation of students and researchers in the observation and analysis techniques. Besides, we plan to improve and increase our observation facilities. In the meantime, we will fulfill the following tasks: i) carry out infrared observations to estimate precise asteroid sizes and albedos, ii) start taxonomical classification of bright objects ($V < 15$), and iii) undertake theoretical studies of asteroids' dynamical behavior.

4. Acknowledgments

WJS gratefully acknowledges financial support from the Universidad Nacional Autónoma de México, grant DGAPA-PAPIIT, project IN100918. M.E.C. acknowledges financial support from CONACyT (México). IRAF is distributed by the National Optical Astronomy Observatory, which is operated by the Association of Universities for Research in Astronomy (AURA) under a cooperative agreement with the National Science Foundation. Collaborative Asteroids Lightcurve Link (CALL) can be accessed at www.minorplanet.info/call.html. Asteroid Lightcurve Photometry Database (ALCDEF) can be accessed at alcddef.org.

References

- Haro-Corzo, S. A. R., Villegas, L. A., Olguín, L., Saucedo, J. C., Contreras, M. E., Sada, P. V., Ayala, S. A., Garza, J. R., Segura-Sosa, J., & Benítez-Benítez, C. P. 2018, *MPBu*, 45, 233
- Sada, P. V., Navarro-Meza, S., Reyes-Ruiz, M., Olguín, L., Saucedo, J. C., & Loera-González, P. 2016, *MPBu*, 43, 154
- Sada, P. V., Olguín, L., Saucedo, J. C., Loera-González, P., Cantú-Sánchez, L., Garza, J. R., Ayala-Gómez, S. A., Avilés, A., Pérez-Tijerina, E., Navarro-Meza, S., Silva, J.S., Reyes-Ruiz, M., Segura-Sosa, J., López-Valdivia, R., & Álvarez-Santana, F. 2017, *MPBu*, 44, 239
- Sada, P., Loera-González, P., Olguín, L., Saucedo-Morales, J. C., Ayala, S. A., & Garza, J. R. 2018, *MPBu*, 45, 122
- Stetson, P. 1987, *PASP*, 99, 191

C. El primer objeto interestelar observado y sus implicaciones en la formación planetaria

'Oumuamua es el primer objeto interestelar observado. Utilizando una aproximación geométrica simple, este artículo calcula la probabilidad de que un observador en la Tierra detecte objetos como este. Se concluye que es posible detectarlos si las estrellas vecinas eyectan una masa de su disco protoplanetario comparable a la que se calcula que se eyectó durante la formación del nuestro.

Me integré al trabajo cuando el modelo ya estaba bosquejado. Participé en la discusión de qué suposiciones era razonable considerar en el modelo y en la discusión de los resultados.



Implications for Planetary System Formation from Interstellar Object 1I/2017 U1 (‘Oumuamua)

David E. Trilling¹, Tyler Robinson¹, Alissa Roegege¹, Colin Orion Chandler¹, Nathan Smith¹, Mark Loeffler¹, Chad Trujillo¹, Samuel Navarro-Meza^{1,2}, and Lori M. Glaspie¹

¹Department of Physics and Astronomy, Northern Arizona University, P.O. Box 6010, Flagstaff, AZ 86011, USA; david.trilling@nau.edu

²Instituto de Astronomía Universidad Nacional Autónoma de México, Ensenada B.C. 22860, México

Received 2017 November 3; revised 2017 November 8; accepted 2017 November 8; published 2017 November 30

Abstract

The recently discovered minor body 1I/2017 U1 (‘Oumuamua) is the first known object in our solar system that is not bound by the Sun’s gravity. Its hyperbolic orbit (eccentricity greater than unity) strongly suggests that it originated outside our solar system; its red color is consistent with substantial space weathering experienced over a long interstellar journey. We carry out a simple calculation of the probability of detecting such an object. We find that the observed detection rate of 1I-like objects can be satisfied if the average mass of ejected material from nearby stars during the process of planetary formation is ~ 20 Earth masses, similar to the expected value for our solar system. The current detection rate of such interstellar interlopers is estimated to be 0.2 yr^{-1} , and the expected number of detections over the past few years is almost exactly one. When the Large Synoptic Survey Telescope begins its wide, fast, deep all-sky survey, the detection rate will increase to 1 yr^{-1} . Those expected detections will provide further constraints on nearby planetary system formation through a better estimate of the number and properties of interstellar objects.

Key words: comets: individual (1I/2017 U1 (‘Oumuamua)) – local interstellar matter – minor planets, asteroids: individual (1I/2017 U1 (‘Oumuamua)) – planetary systems – protoplanetary disks – solar neighborhood

1. Introduction

On 2017 October 18, the minor body C/2017-UT (PANSTARRS), which would become known as A/2017 U1 and later 1I/2017 U1 (‘Oumuamua)—hereafter, 1I—was discovered by the Panoramic Survey Telescope And Rapid Response System (Pan-STARRS) survey (Chambers et al. 2016). In a matter of days, it became clear that this object was on an unbound (hyperbolic) trajectory, with eccentricity $e \approx 1.2$ (Williams 2017). In addition to its high eccentricity, 1I’s orbit is inclined to the solar system plane at an angle $i \approx 123^\circ$, so it is very unlikely to have encountered any massive objects within our solar system (other than the Sun). With no gravitational perturbations to explain its anomalously high eccentricity, the most likely explanation is that this object originated outside of our solar system and happened to pass close to the Earth during its journey through interstellar space. This implies that 1I formed in another planetary system and was ejected, presumably through dynamical interactions in its natal planetary system. Consequently, we refer to 1I and similar bodies as “ejectoids.”

The theoretical existence of ejectoids has been long proposed (e.g., Sekanina 1976), with various authors using nondetections to place upper limits on the population (McGlynn & Chapman 1989; Sen & Rama 1993; Engelhardt et al. 2017). Jewitt (2003) and Francis (2005) suggested that PanSTARRS could detect an interstellar object, if the number density was great enough. In the two weeks since the discovery of 1I and its identification as an interstellar object, we have learned about its optical spectrum (Masiero 2017; Ye et al. 2017), its light curve (Knight et al. 2017), its orbit (de la Fuente Marcos & de la Fuente Marcos 2017), and its potential origin scenarios (Gaidos et al. 2017; Laughlin & Batygin 2017; Mamajek 2017).

Here we use a simple calculation to estimate the probability of detecting such an object and explore the implications for the

prevalence and properties of planetary systems that are implied by the existence and properties of 1I.

2. Ejectoid Encounters and Ejected Mass Constraints

Gravitational microlensing results have shown that, on average, every star in the Milky Way is accompanied by at least one bound planet (Cassan et al. 2012), which implies that planet formation is a near-universal process. We assume here that the formation of a typical planetary system results in a mass m of ejectoids with a typical size of r_e and mass density ρ_e . The number of ejectoids per star is therefore

$$\frac{m}{\frac{4}{3}\pi r_e^3 \rho_e}. \quad (1)$$

We can write the number density of stars (in, e.g., stars per cubic parsec) n_s in terms of a characteristic stellar spacing, R , as

$$n_s = \frac{1}{\frac{4}{3}\pi R^3}. \quad (2)$$

This enables us to express the number density of ejectoids (number/volume) as

$$n_e = \left(\frac{m}{\frac{4}{3}\pi r_e^3 \rho_e} \right) \left(\frac{1}{\frac{4}{3}\pi R^3} \right). \quad (3)$$

We next wish to determine the number of ejectoids that we expect to have encountered. We assume that telescopic searches for 1I-like objects have swept out a cylindrical volume of interstellar space given by

$$V_{\text{obs}} = \pi r_{\text{obs}}^2 \Delta v_{\odot} \Delta t, \quad (4)$$

where r_{obs} is the geocentric distance out to which we are sensitive to 1I-like objects, Δv_{\odot} is the Sun’s velocity through

the solar neighborhood (and the presumed cloud of ejectoids), and Δt is the time interval over which observational surveys have been capable of discovering II-like objects. Using this volume and the number density of ejectoids, we find that the number of detections of II-like objects is

$$N = n_e V_{\text{obs}} = \left(\frac{m}{\frac{4}{3}\pi r_e^3 \rho_e} \right) \left(\frac{1}{\frac{4}{3}\pi R^3} \right) (\pi r_{\text{obs}}^2 \Delta v_{\odot} \Delta t), \quad (5)$$

which simplifies to

$$N = \frac{9}{16\pi} \frac{m r_{\text{obs}}^2 \Delta v_{\odot} \Delta t}{\rho_e r_e^3 R^3}. \quad (6)$$

We can now use II to constrain the characteristic mass in ejectoids for a forming planetary system. With $N = 1$, we can rearrange Equation (6) to write that

$$m = \frac{16\pi}{9} \frac{\rho_e r_e^3 R^3}{r_{\text{obs}}^2 \Delta v_{\odot} \Delta t}. \quad (7)$$

The absolute magnitude of II is given in the Minor Planet Center catalog as 22.1 (as of 2017 November 2), which corresponds to a radius r_e of around 100 meters, assuming a moderate-to-dark albedo.

The range of densities for cometary and asteroidal material that may be relevant is around 500 to 3000 kg m⁻³ (Davidsson & Gutiérrez 2006; Davidsson et al. 2007; Richardson et al. 2007; Carry 2012). While II's highly eccentric orbit would typically be associated with a comet, and theoretical predictions suggest that most ejectoids should be more comet-like (Raymond et al. 2011), there are no signs of activity from II (Knight et al. 2017; Ye et al. 2017). Thus, here, we assume that II may be more asteroidal than cometary and adopt a density of 2000 kg m⁻³.

There are 357 stars within 10 parsecs of the Sun.³ This gives an average distance between adjacent stars R of 1.4 pc. The average discovery distance of near-Earth objects in the minor planet center r_{obs} is 0.3 au.

The velocity of the Sun relative to nearby stars is around 20 km s⁻¹ (Schönrich et al. 2010). II has been found⁴ to have an interstellar speed (velocity at infinity) of 26 km s⁻¹, while Mamajek (2017) reports that an object entering the solar system with median velocity of the local stellar population would have a speed of around 22.5 km s⁻¹. The fact that the Sun's relative velocity is comparable to the velocity of II confirms our assumption that the population of interstellar ejectoids has zero mean velocity (due to the fact that both the source planetary systems and ejection trajectories are assumed to be isotropic). Based on these three estimates, we set Δv_{\odot} to be 25 km s⁻¹.

In recent years, improvements on detector size and field of view at the Catalina Sky Survey and Pan-STARRS (the two major NEO surveys) have enhanced the ability to detect II-like objects, so we estimate Δt to be 5 years.

Our characteristic values, when inserted in Equation (7), yield a typical mass in ejected II-like objects of 10²⁶ kg, or 20 M_{\oplus} . This is in remarkably good agreement with values derived for mass loss during the formation of our solar system. For example, Weidenschilling (1977) and Bottke et al. (2005) derive 1–5 M_{\oplus} of material lost from the asteroid belt. Kuiper

(1951), Kenyon & Luu (1999), and Morbidelli (2005) find 12–30 M_{\oplus} lost from the Kuiper Belt. Together, these imply a total mass lost from our solar system of close to 20 M_{\oplus} .

Identifying the characteristic size and density of ejectoids as being the most uncertain terms in our analysis, and inserting the parameter values adopted above, we can write

$$m = 20 M_{\oplus} \left(\frac{\rho_e}{2000 \text{ kg m}^{-3}} \right) \left(\frac{r_e}{100 \text{ m}} \right)^3. \quad (8)$$

This relationship is shown in Figure 1. The plausible range of ejection masses is roughly 1–100 M_{\oplus} . We note that in principle the radius of II, which we take to be characteristic of ejectoids, will be determined through our forthcoming thermal infrared observations of II with the *Spitzer Space Telescope* (observations scheduled for late 2017 November). There is no direct way to constrain the density of II, though indirect constraints may be possible from the rotation period.

Alternatively, if we adopt the $\sim 20 M_{\oplus}$ in ejectoids lost during the formation of the solar system as a characteristic number, we can use Equation (6) to derive the number of II-like objects expected over five years. We find that N is very close to unity—exactly matching the observations. The detection rate ($N/\Delta t$) is therefore 0.2 II-like objects per year, or one II-like object every five years. The number density of ejectoids is, from Equation (3), around 0.1/au³, which is around 10¹⁵/pc³.

3. Caveats and Uncertainties

We do not claim that this is the only mechanism for producing II-like objects or delivering such objects to the detectable space near the Earth, as the above calculation admittedly contains a number of assumptions. However, this does give a plausible explanation for II that in turn has several interesting implications that are discussed below.

The radius and density of II are unknown, though the values above are unlikely to be in error by more than a factor of two. Similarly, the geometry arguments (average stellar distance, solar velocity, and observational distance) are likely within a factor of two, while the time interval is approximately correct. We ignore gravitational focusing here. The largest overall uncertainty is simply the unknown statistical likelihood of detecting this ejectoid and our extrapolation from a single object. II may be part of a constant stream of interstellar objects moving through our solar system (as implied here), or a very unlikely occurrence, in which case the arguments made here are less applicable.

In addition, the true population of ejected extrasolar material must follow some size distribution, and will not consist of only 100 m II-like objects. Small objects are presumably more numerous in any planet formation scenario, but larger objects will be preferentially detected by our surveys. We must simply take II to be representative.

In the above calculation, we have assumed that a steady-state population of II-like objects is ejected from all planetary systems. However, we might instead assume that the majority of ejectoids are produced during the earliest phases of planetary system formation, in a single pulse of material. The nearest star formation regions are some 100 parsec away, with typical ages of 1–10 Myr (Andrews et al. 2009; Currie & Sicilia-Aguilar 2011; Esplin & Luhman 2017). If we take the escape velocity from those systems to be on the order of 10 km s⁻¹ then material from one of these nearby star formation regions

³ <http://www.recons.org>

⁴ <https://projectpluto.com/temp/2017u1.htm>

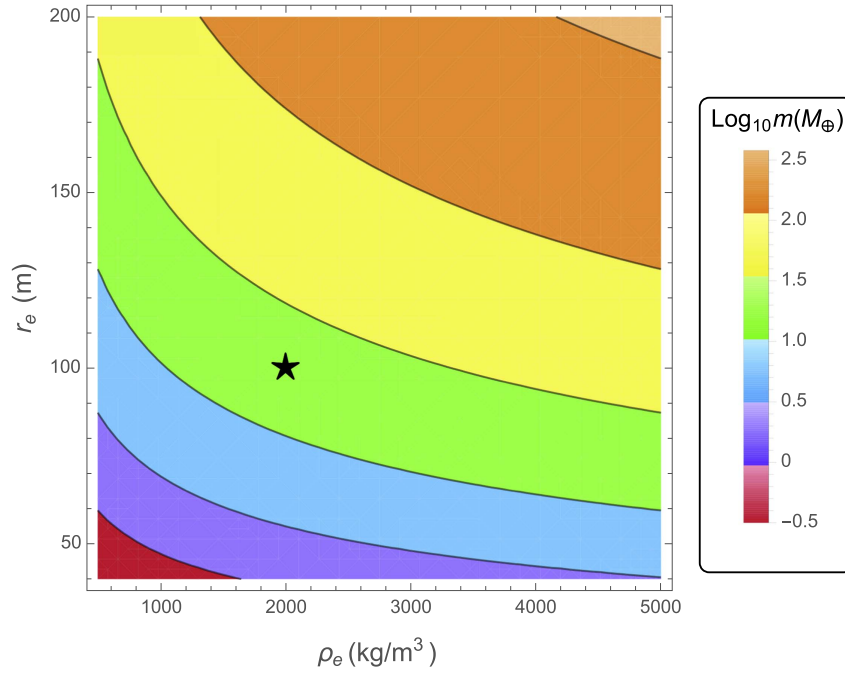


Figure 1. Characteristic ejection mass (colors and contours, in Earth masses) required to produce the observed rate of II-like objects as a function of the primary unknown parameters in our analysis: II’s density (ρ_e) and radius (r_e). For nominal values of 2000 kg m^{-3} and 100 m , respectively, the required average ejection mass per star in the solar neighborhood is $20 M_{\oplus}$ (black star), remarkably close to various calculations of the mass lost from our solar system during the era of planet formation. Our upcoming observations of II with the *Spitzer Space Telescope* in late 2017 November should place a constraint on II’s radius.

would reach the Earth in a few million years, and we would therefore be moving through a cloud of ejected II-like objects. However, the rest of the assumptions still apply, and the expected value does not change significantly. A more complicated model (perhaps not warranted, given this single detection) could account for the total number of stars contained in the Milky Way, integrated over its history, as even stars that no longer exist could have contributed ejectoids to an interstellar stream of material.

Finally, we note that the above calculation implies a typical ejected mass of $20 M_{\oplus}$, but that need not imply that every stellar or planetary system ejects mass, or that amount of material. For example, while planet–planet scattering among gas giant planets is likely to produce a pulse of ejected planetesimals (Raymond et al. 2011; Marzari 2014), and while systems with gas giants on stable orbits can eject planetesimals on longer timescales (Raymond et al. 2011; Barclay et al. 2017), systems without gas giants rarely eject planetesimals because in that case escape velocity cannot readily be achieved by planetesimals. Thus, if the fraction of nearby stars with gas giants is (for example) 50%, then the average mass ejected by those systems must be a factor of ~ 2 greater than our nominal value in order to produce the necessary interstellar density of ejectoids.

4. Implications

The 520–950 nm reflectance spectrum of II, albeit noisy, indicates no absorption features and a red spectral slope (Masiero 2017; Ye et al. 2017), making compositional characterization difficult. However, we note that a red spectral slope over this range is not unexpected and is characteristic of many primitive objects in our solar system (Cruikshank et al. 1998; Jewitt & Luu 1998; Bus & Binzel 2002; Sheppard 2010; Carry et al. 2016). Whether this slope is

something intrinsic to the bulk properties of II or a consequence of its surface being altered via energetic processing is unclear. Given the presence of cosmic rays in the interstellar medium and other forms of ionizing radiation that would have been present in II’s natal stellar environment, II’s red spectral slope is entirely consistent with formation elsewhere and a long journey to our solar system. This implies that the surface of II may have different properties than its bulk material.

II’s trajectory makes it very unlikely that it experienced a gravitational encounter with any of the proposed as-yet unknown planets in the outermost part of our solar system (Trujillo & Sheppard 2014; Brown & Batygin 2016; Volk & Malhotra 2017). Another possibility is that II was a member of our solar system’s Oort Cloud and was perturbed inbound onto an unbound orbit by a passing star. We do not comment on these scenarios; in this work, we have assumed that II is an interstellar interloper that originated in a different planetary system.

The Large Synoptic Survey Telescope (LSST; Ivezić et al. 2008) will commence its 10-year all-sky survey in 2022. One of the driving science cases for LSST is the detection of moving objects. Most moving objects detected by LSST will be “unremarkable” asteroids in the main belt, but this very large and deep survey ($20,000 \text{ deg}^2$ surveyed to r magnitude 24.5 repeatedly over 10 years) naturally has the possibility to discover unusual objects in all areas of astrophysics. Several authors have studied the detectability of interstellar interlopers in LSST data (Moro-Martín et al. 2009; Cook et al. 2016; Engelhardt et al. 2017).




LSST will help constrain nearby planetary system formation by measuring the number of II-like objects. LSST will be sensitive to fainter and therefore smaller and/or more distant objects, and is therefore likely to have a greater detection rate than the current rate. The possibility of LSST detecting interstellar comets increases by an order(s) of magnitude when

considering cometary outbursting (Cook et al. 2016), which makes objects brighter, although II has shown no signs of activity so far in its observational record.

As described above, with our current detection sensitivities, the detection rate for II-like objects is 0.2 yr^{-1} . The LSST detection limit will be around three magnitudes deeper than Pan-STARRS' typical limiting magnitude of $V \sim 21.5$; this translates to a factor of three smaller in size. The only measured size distribution in this size range in our solar system is for the near-Earth object population; a factor of three in size corresponds roughly to a factor of five in number of objects (Trilling et al. 2017). Thus, the expected detection rate of interstellar objects for LSST is around 1 yr^{-1} . The LSST discovery rate of ejectoids will help us constrain the frequency and properties of planetary system formation in our nearby galaxy.

We thank an anonymous referee for a very prompt and thoughtful review that has improved this paper. This research has made use of data and services provided by the International Astronomical Union's Minor Planet Center. We have used information from the RECONS program, retrieved from <http://www.recons.org>. The discussions that led to this paper began at an NAU Astrocookies gathering.

ORCID iDs

David E. Trilling  <https://orcid.org/0000-0003-4580-3790>
 Tyler Robinson  <https://orcid.org/0000-0002-3196-414X>
 Colin Orion Chandler  <https://orcid.org/0000-0001-7335-1715>

References

- Andrews, S. M., Wilner, D. J., Hughes, A. M., Qi, C., & Dullemond, C. P. 2009, *ApJ*, **700**, 1502
- Barclay, T., Quintana, E. V., Raymond, S. N., & Penny, M. T. 2017, *ApJ*, **841**, 86
- Botke, W. F., Durda, D. D., Nesvorný, D., et al. 2005, *Icar*, **175**, 111
- Brown, M. E., & Batygin, K. 2016, *ApJL*, **824**, L23
- Bus, S. J., & Binzel, R. P. 2002, *Icar*, **158**, 146
- Carry, B. 2012, *P&SS*, **73**, 98
- Carry, B., Solano, E., Eggl, S., & DeMeo, F. E. 2016, *Icar*, **268**, 340
- Cassan, A., Kubas, D., Beaulieu, J. P., et al. 2012, *Natur*, **481**, 167
- Chambers, K. C., Magnier, E. A., Metcalfe, N., et al. 2016, arXiv:1612.05560
- Cook, N. V., Ragozzine, D., Granvik, M., & Stephens, D. C. 2016, *ApJ*, **825**, 51
- Cruikshank, D. P., Roush, T. L., Bartholomew, M. J., et al. 1998, *Icar*, **135**, 389
- Currie, T., & Sicilia-Aguilar, A. 2011, *ApJ*, **732**, 24
- Davidsson, B. J. R., & Gutiérrez, P. J. 2006, *Icar*, **180**, 224
- Davidsson, B. J. R., Gutiérrez, P. J., & Rickman, H. 2007, *Icar*, **187**, 306
- de la Fuente Marcos, C., & de la Fuente Marcos, R. 2017, *RNAAS*, **1**, 9
- Engelhardt, T., Jedicke, R., Vereš, P., et al. 2017, *AJ*, **153**, 133
- Esplin, T. L., & Luhman, K. L. 2017, *AJ*, **154**, 134
- Francis, P. J. 2005, *ApJ*, **635**, 1348
- Gaidos, E., Williams, J. P., & Kraus, A. 2017, RNAAS, submitted (arXiv:1711.01300)
- Ivezić, Ž, Tyson, J. A., Abel, B., et al. 2008, arXiv:0805.2366v4
- Jewitt, D. 2003, *EM&P*, **92**, 465
- Jewitt, D., & Luu, J. 1998, *AJ*, **115**, 1667
- Kenyon, S. J., & Luu, J. X. 1999, *AJ*, **118**, 1101
- Knight, M. M., Protopapa, S., Kelly, M. S. P., et al. 2017, *ApJL*, submitted (arXiv:1711.01402)
- Kuiper, G. P. 1951, *PNAS*, **37**, 1
- Laughlin, G., & Batygin, K. 2017, RNAAS, submitted (arXiv:1711.02260)
- Mamajek, E. 2017, RNAAS, in press (arXiv:1710.11364)
- Marzari, F. 2014, *MNRAS*, **444**, 1419
- Masiero, J. 2017, arXiv:1710.09977
- McGlynn, T. A., & Chapman, R. D. 1989, *ApJL*, **346**, L105
- Morbidelli, A. 2005, arXiv:astro-ph/0512256
- Moro-Martín, A., Turner, E. L., & Loeb, A. 2009, *ApJ*, **704**, 733
- Raymond, S. N., Armitage, P. J., Moro-Martín, A., et al. 2011, *A&A*, **530**, 62
- Richardson, J. E., Melosh, H. J., Lisse, C. M., & Carcich, B. 2007, *Icar*, **190**, 357
- Schönrich, R., Binney, J., & Dehnen, W. 2010, *MNRAS*, **403**, 1829
- Sekanina, Z. 1976, *Icar*, **27**, 123
- Sen, A. K., & Rama, N. C. 1993, *A&A*, **275**, 298
- Sheppard, S. S. 2010, *AJ*, **139**, 1394
- Trilling, D. E., Valdes, F., Allen, L., et al. 2017, *AJ*, **154**, 170
- Trujillo, C. A., & Sheppard, S. S. 2014, *Natur*, **507**, 471
- Volk, K., & Malhotra, R. 2017, *AJ*, **154**, 62
- Weidenschilling, S. J. 1977, *Ap&SS*, **51**, 153
- Williams, G. V. 2017, MPEC 2017-U183: A/2017 U1, <https://www.minorplanetcenter.net/mpec/K17/K17U13>
- Ye, Q.-Z., Zhang, Q., Kelley, M. S. P., & Brown, P. G. 2017, *ApJL*, in press (arXiv:1711.02320)

D. Observaciones del efecto YORP

El efecto YORP es una interacción no dinámica que afecta el comportamiento de los asteroides, particularmente su efecto de rotación. La escala de tiempo para este efecto es del orden de mega años, sin embargo estudios recientes sugieren que el efecto puede observarse en una escala de tiempo medible para nosotros y que además altera los asteroides de otras maneras, como en su forma.

Sometí dos propuestas de observación para estudiar este efecto durante el 2018, las cuales fueron aceptadas por la CATT del OAN. Este trabajo lo estoy haciendo junto con el Dr. Sergio Silva y otros colaboradores. La generación de resultados está en curso por parte del Dr. Silva y sus estudiantes.

E. Convocatoria CONACYT Ciencia de Frontera 2019

Junto con mis asesores, los Dres Mauricio Reyes, Joel Castro y un equipo de colaboradores elaboramos una propuesta para dicha convocatoria orientada al estudio de NEOs. Proporcioné referencias para familiarizar a los miembros del equipo ajenos al área, participé activamente en la discusión de los objetivos del proyecto y contribuí a la escritura y edición de la propuesta. Estamos en espera de los resultados.

F. Divulgación

Contribuí con un artículo para la Gaceta Ensenada, 33a edición (p.10 y 11). El artículo se basa en un proyecto en curso titulado 'Para qué te sirve la astronomía?' que estoy realizando con la estudiante de doctorado Valeria Ramírez y la diseñadora Paulina Lazcano.

En agosto de 2018 participé en el Día de la juventud, dentro del marco de la Feria de la Nación Navajo en Window Rock, Arizona. Junto con otros voluntarios realizamos observaciones solares, hicimos brazaletes que brillan

tras iluminarse con la luz UV del Sol y explicamos un poco de mecánica rotacional por medio de un juego.

Referencias

Asteroid Mining Corporation. 2020.

Glosario del Centro de estudios de asteroides cercanos a la Tierra de la NASA. 2020.

The Space Resource. January 2020.

AURA Association of Universities for Research in Astronomy. Vera C. Rubin Observatory. 2020.

Allen David A. Infrared Diameter of Vesta // *Nature.* VII 1970. 227, 5254. 158–159.

Binzel R. P., DeMeo F. E., Turtelboom E. V., Bus S. J., Tokunaga A., Burbine T. H., Lantz C., Polishook D., Carry B., Morbidelli A., Birlan M., Vernazza P., Burt B. J., Moskovitz N., Slivan S. M., Thomas C. A., Rivkin A. S., Hicks M. D., Dunn T., Reddy V., Sanchez J. A., Granvik M., Kohout T. Compositional distributions and evolutionary processes for the near-Earth object population: Results from the MIT-Hawaii Near-Earth Object Spectroscopic Survey (MITHNEOS) // *Icarus.* V 2019. 324. 41–76.

Borisov G. MPEC 2019-R106. 2019.

Bottke William F., Morbidelli Alessandro, Jedicke Robert, Petit Jean-Marc, Levison Harold F., Michel Patrick, Metcalfe Travis S. Debaised Orbital and Absolute Magnitude Distribution of the Near-Earth Objects // *Icarus.* IV 2002. 156, 2. 399–433.

Brough Sarah, Collins Chris, Demarco Ricardo, Ferguson Henry C., Galaz Gaspar, Holwerda Benne, Martinez-Lombilla Cristina, Mihos Chris, Montes Mireia. The Vera Rubin Observatory Legacy Survey of Space

and Time and the Low Surface Brightness Universe // arXiv e-prints. I
2020. arXiv:2001.11067.

Brown P. G., Assink J. D., Astiz L., Blaauw R., Boslough M. B., Borovička J., Brachet N., Brown D., Campbell-Brown M., Ceranna L., Cooke W., de Groot-Hedlin C., Drob D. P., Edwards W., Evers L. G., Garcés M., Gill J., Hedlin M., Kingery A., Laske G., Le Pichon A., Mialle P., Moser D. E., Saffer A., Silber E., Smets P., Spalding R. E., Spurný P., Tagliaferri E., Uren D., Weryk R. J., Whitaker R., Krzeminski Z. A 500-kiloton airburst over Chelyabinsk and an enhanced hazard from small impactors // *Nature*. XI 2013. 503, 7475. 238–241.

Bus S. J. Compositional structure in the asteroid belt: Results of a spectroscopic survey. 1999.

Cellino A., Zappalà V., Doressoundiram A., Di Martino M., Bendjoya Ph., Dotto E., Migliorini F. The Puzzling Case of the Nysa-Polana Family // *Icarus*. VIII 2001. 152, 2. 225–237.

Chambers K. C., Magnier E. A., Metcalfe N., Flewelling H. A., Huber M. E., Waters C. Z., Denneau L., Draper P. W., Farrow D., Finkbeiner D. P., Holmberg C., Koppenhoefer J., Price P. A., Rest A., Saglia R. P., Schlafly E. F., Smartt S. J., Sweeney W., Wainscoat R. J., Burgett W. S., Chastel S., Grav T., Heasley J. N., Hodapp K. W., Jedicke R., Kaiser N., Kudritzki R. P., Luppino G. A., Lupton R. H., Monet D. G., Morgan J. S., Onaka P. M., Shiao B., Stubbs C. W., Tonry J. L., White R., Bañados E., Bell E. F., Bender R., Bernard E. J., Boegner M., Boffi F., Botticella M. T., Calamida A., Casertano S., Chen W. P., Chen X., Cole S., Deacon N., Frenk C., Fitzsimmons A., Gezari S., Gibbs V., Goessl C., Goggia T., Gourgue R., Goldman B., Grant P., Grebel E. K., Hambly N. C., Hasinger G., Heavens A. F., Heckman T. M., Henderson R., Henning T., Holman M., Hopp U., Ip W. H., Isani S., Jackson M., Keyes C. D., Koekemoer A. M., Kotak R., Le D., Liska D., Long K. S., Lucey J. R., Liu M., Martin N. F., Masci G., McLean B., Mindel E., Misra P., Morganson E., Murphy D. N. A., Obaika A., Narayan G.,

- Nieto-Santisteban M. A., Norberg P., Peacock J. A., Pier E. A., Postman M., Primak N., Rae C., Rai A., Riess A., Riffeser A., Rix H. W., Röser S., Russel R., Rutz L., Schilbach E., Schultz A. S. B., Scolnic D., Strolger L., Szalay A., Seitz S., Small E., Smith K. W., Soderblom D. R., Taylor P., Thomson R., Taylor A. N., Thakar A. R., Thiel J., Thilker D., Unger D., Urata Y., Valenti J., Wagner J., Walder T., Walter F., Watters S. P., Werner S., Wood-Vasey W. M., Wyse R.* The Pan-STARRS1 Surveys // arXiv e-prints. XII 2016. arXiv:1612.05560.
- DeMeo F. E., Alexander C. M. O'D., Walsh K. J., Chapman C. R., Binzel R. P.* The Compositional Structure of the Asteroid Belt // Asteroids IV. 2015. 13–41.
- DeMeo F. E., Binzel R. P., Slivan S. M., Bus S. J.* An extension of the Bus asteroid taxonomy into the near-infrared // ICARUS. VII 2009. 202. 160–180.
- Devogèle Maxime, Moskovitz Nicholas, Thirouin Audrey, Gustaffson Annika, Magnuson Mitchell, Thomas Cristina, Willman Mark, Christensen Eric, Person Michael, Binzel Richard, Polishook David, DeMeo Francesca, Hinkle Mary, Trilling David, Mommert Michael, Burt Brian, Skiff Brian.* Visible Spectroscopy from the Mission Accessible Near-Earth Object Survey (MANOS): Taxonomic Dependence on Asteroid Size // AJ. XI 2019. 158, 5. 196.
- Erasmus N., Mommert M., Trilling D. E., Sicking A. A., van Gend C., Hora J. L.* Characterization of Near-Earth Asteroids Using KMTNET-SAAO // AJ. X 2017a. 154, 4. 162.
- Erasmus N., Mommert M., Trilling D. E., Sicking A. A., van Gend C., Hora J. L.* Characterization of Near-Earth Asteroids Using KMTNET-SAAO // AJ. X 2017b. 154, 4. 162.
- Erasmus N., Navarro-Meza S., McNeill A., Trilling D. E., Sicking A. A., Denneau L., Flewelling H., Heinze A., Tonry J. L.* Investigating

- Taxonomic Diversity within Asteroid Families through ATLAS Dual-band Photometry // *The Astrophysical Journal Supplement Series*. III 2020. 247, 1. 13.
- Fornasier S., Lazzarin M., Barbieri C., Barucci M. A.* Spectroscopic comparison of aqueous altered asteroids with CM2 carbonaceous chondrite meteorites // *A&AS*. II 1999. 135. 65–73.
- Gardner Jonathan P., Mather John C., Clampin Mark, Doyon Rene, Greenhouse Matthew A., Hammel Heidi B., Hutchings John B., Jakobsen Peter, Lilly Simon J., Long Knox S., Lunine Jonathan I., McCaughrean Mark J., Mountain Matt, Nella John, Rieke George H., Rieke Marcia J., Rix Hans-Walter, Smith Eric P., Sonneborn George, Stiavelli Massimo, Stockman H. S., Windhorst Rogier A., Wright Gillian S.* Science with the James Webb space telescope // *Proc. SPIE*. 6265. VI 2006. 62650N. (Society of Photo-Optical Instrumentation Engineers (SPIE) Conference Series).
- Gradie J., Tedesco E.* Compositional Structure of the Asteroid Belt // *Science*. VI 1982. 216, 4553. 1405–1407.
- Granvik Mikael, Morbidelli Alessandro, Jedicke Robert, Bolin Bryce, Bottke William F., Beshore Edward, Vokrouhlický David, Nesvorný David, Michel Patrick.* Debaised orbit and absolute-magnitude distributions for near-Earth objects // *Icarus*. IX 2018. 312. 181–207.
- Graps Amara.* Ten Asteroid Mining Milestones in 2018-2019 // EPSC-DPS Joint Meeting 2019. 2019. IX 2019. EPSC–DPS2019–1724.
- Groeneveld I., Kuiper G. P.* Photometric Studies of Asteroids. I // *APJ*. IX 1954.
- Harris Alan.* What Spaceguard did // *Nature*. VI 2008. 453, 7199. 1178–1179.
- Hartmann W. K., Tholen D. J., Cruikshank D. P.* The relationship of active comets, “extinct” comets, and dark asteroids // *Icarus*. I 1987. 69, 1. 33–50.

- Hein Andreas M., Matheson Robert, Fries Dan.* A techno-economic analysis of asteroid mining // *Acta Astronautica*. III 2020. 168. 104–115.
- Heinze A. N., Tonry J. L., Denneau L., Flewelling H., Stalder B., Rest A., Smith K. W., Smartt S. J., Weiland H.* A First Catalog of Variable Stars Measured by the Asteroid Terrestrial-impact Last Alert System (ATLAS) // *AJ*. XI 2018. 156, 5. 241.
- Hewett P. C., Warren S. J., Leggett S. K., Hodgkin S. T.* The UKIRT Infrared Deep Sky Survey ZY JHK photometric system: passbands and synthetic colours // *MNRAS*. IV 2006. 367. 454–468.
- Hinkle M. L.* Master thesis. 2016.
- Hinkle M. L., Moskovitz N., Trilling D., Binzel R. P., Thomas C., Christensen E., DeMeo F., Person M. J., Polishook D., Willman M.* The Bias-Corrected Taxonomic Distribution of Mission-Accessible Small Near-Earth Objects // AAS/Division for Planetary Sciences Meeting Abstracts. 47. XI 2015. 301.04. (AAS/Division for Planetary Sciences Meeting Abstracts).
- Housen K. R., Holsapple K. A.* On the fragmentation of asteroids and planetary satellites // *Icarus*. III 1990. 84, 1. 226–253.
- IAU . MPEC 2017-U181.* 2017.
- Ivezić Željko, Suberlak Krzysztof, Boberg Owen M.* LSST: making movies of AGB stars // *IAU Symposium*. 343. XII 2019. 59–68. (IAU Symposium).
- Jedicke R., Granvik M., Micheli M., Ryan E., Spahr T., Yeomans D. K.* Surveys, Astrometric Follow-Up, and Population Statistics // *Asteroids IV*. 2015. 795–813.
- Jones Thomas D., Lebofsky Larry A., Lewis John S., Marley Mark S.* The composition and origin of the C, P, and D asteroids: Water as a tracer of thermal evolution in the outer belt // *Icarus*. XI 1990. 88, 1. 172–192.
- Kubat Miroslav.* An introduction to Machine Learning. 2017. 2nd.

- Larson S., Brownlee J., Hergenrother C., Spahr T.* The Catalina Sky Survey for NEOs // *Bulletin of the American Astronomical Society.* 30. IX 1998. 1037.
- Lomb N. R.* Least-Squares Frequency Analysis of Unequally Spaced Data // *Ap&SS.* II 1976. 39, 2. 447–462.
- Mainzer A., Grav T., Bauer J., Masiero J., McMillan R. S., Cutri R. M., Walker R., Wright E., Eisenhardt P., Tholen D. J., Spahr T., Jedicke R., Denneau L., DeBaun E., Elsbury D., Gautier T., Gomillion S., Hand E., Mo W., Watkins J., Wilkins A., Bryngelson G. L., Del Pino Molina A., Desai S., Gómez Camus M., Hidalgo S. L., Konstantopoulos I., Larsen J. A., Maleszewski C., Malkan M. A., Mauduit J. C., Mullan B. L., Olszewski E. W., Pforr J., Saro A., Scotti J. V., Wasserman L. H.* NEOWISE Observations of Near-Earth Objects: Preliminary Results // *The Astrophysical Journal.* XII 2011. 743, 2. 156.
- Mainzer A., Usui F., Trilling D. E.* Space-Based Thermal Infrared Studies of Asteroids // *Asteroids IV.* 2015. 89–106.
- Matson Dennis L.* Infrared Observations of Asteroids // *NASA Special Publication.* 267. 1971. 45–50.
- McFadden L. A., Gaffey M. J., McCord T. B.* Near-earth asteroids - Possible sources from reflectance spectroscopy // *Science.* VII 1985. 229. 160–163.
- Miyamoto Hideaki, Yano Hajime, Scheeres Daniel J., Abe Shinsuke, Barnouin-Jha Olivier, Cheng Andrew F., Demura Hirohide, Gaskell Robert W., Hirata Naru, Ishiguro Masateru, Michikami Tatsuhiro, Nakamura Akiko M., Nakamura Ryosuke, Saito Jun, Sasaki Sho.* Regolith Migration and Sorting on Asteroid Itokawa // *Science.* V 2007. 316, 5827. 1011.
- Mommert M., Harris A. W., Mueller M., Hora J. L., Trilling D. E., Bottke W. F., Thomas C. A., Delbo M., Emery J. P., Fazio G., Smith H. A.*

- ExploreNEOs. VIII. Dormant Short-period Comets in the Near-Earth Asteroid Population // *AJ*. X 2015. 150. 106.
- Mommert M., Trilling D. E., Borth D., Jedicke R., Butler N., Reyes-Ruiz M., Pichardo B., Petersen E., Axelrod T., Moskovitz N.* First Results from the Rapid-response Spectrophotometric Characterization of Near-Earth Objects using UKIRT // *AJ*. IV 2016. 151. 98.
- Morbidelli A., Gladman B.* Orbital and temporal distributions of meteorites originating in the asteroid belt // *Meteoritics and Planetary Science*. IX 1998. 33. 999–1016.
- Mothé-Diniz T., Roig F., Carvano J. M.* Reanalysis of asteroid families structure through visible spectroscopy // *Icarus*. III 2005. 174, 1. 54–80.
- NASA . Center for NEO studies, NASA. June 2020a.
- NASA . Solar System Dynamics, JPL. June 2020b.
- Nesvorný D.* Nesvorný HCM Asteroid Families V3.0 // NASA Planetary Data System. XII 2015. EAR-A-VARGBDET-5-NESVORNYFAM-V3.0.
- Nesvorný D., Brož M., Carruba V.* Identification and Dynamical Properties of Asteroid Families // *Asteroids IV*. 2015. 297–321.
- Opik E. J.* Collision probability with the planets and the distribution of planetary matter // *Proc. R. Irish Acad. Sect. A*. I 1951. 54. 165–199.
- Parker A., Ivezić Ž., Jurić M., Lupton R., Sekora M. D., Kowalski A.* The size distributions of asteroid families in the SDSS Moving Object Catalog 4 // *Icarus*. XI 2008. 198, 1. 138–155.
- Popova Olga P., Jenniskens Peter, Emel'yanenko Vacheslav, Kartashova Anna, Biryukov Eugeny, Khaibrakhmanov Sergey, Shuvalov Valery, Rybnov Yuriy, Dudorov Alexandr, Grokhovsky Victor I., Badyukov Dmitry D., Yin Qing-Zhu, Gural Peter S., Albers Jim, Granvik Mikael, Evers Láslo G., Kuiper Jacob, Kharlamov Vladimir, Solovyov*

Andrey, Rusakov Yuri S., Korotkiy Stanislav, Serdyuk Ilya, Korochantsev Alexander V., Larionov Michail Yu., Glazachev Dmitry, Mayer Alexander E., Gisler Galen, Gladkovsky Sergei V., Wimpenny Josh, Sanborn Matthew E., Yamakawa Akane, Verosub Kenneth L., Rowland Douglas J., Roeske Sarah, Botto Nicholas W., Friedrich Jon M., Zolensky Michael E., Le Loan, Ross Daniel, Ziegler Karen, Nakamura Tomoki, Ahn Insu, Lee Jong Ik, Zhou Qin, Li Xian-Hua, Li Qiu-Li, Liu Yu, Tang Guo-Qiang, Hiroi Takahiro, Sears Derek, Weinstein Ilya A., Vokhmintsev Alexander S., Ishchenko Alexei V., Schmitt-Kopplin Phillipe, Hertkorn Norbert, Nagao Keisuke, Haba Makiko K., Komatsu Mutsumi, Mikouchi Takashi, aff34 . Chelyabinsk Airburst, Damage Assessment, Meteorite Recovery, and Characterization // Science. XI 2013. 342, 6162. 1069–1073.

Pravdo Steven H., Rabinowitz David L., Helin Eleanor F., Lawrence Kenneth J., Bamberg Raymond J., Clark Christopher C., Groom Steven L., Levin Steven, Lorre Jean, Shaklan Stuart B., Kervin Paul, Africano John A., Sydney Paul, Soohoo Vicki. The Near-Earth Asteroid Tracking (NEAT) Program: an Automated System for Telescope Control, Wide-Field Imaging, and Object Detection // AJ. III 1999. 117, 3. 1616–1633.

Prentice S. J., Maguire K., Smartt S. J., Magee M. R., Schady P., Sim S., Chen T. W., Clark P., Colin C., Fulton M., McBrien O., O’Neill D., Smith K. W., Ashall C., Chambers K. C., Denneau L., Flewelling H. A., Heinze A., Holoien T. W. S., Huber M. E., Kochanek C. S., Mazzali P. A., Prieto J. L., Rest A., Shappee B. J., Stalder B., Stanek K. Z., Stritzinger M. D., Thompson T. A., Tonry J. L. The Cow: Discovery of a Luminous, Hot, and Rapidly Evolving Transient // The Astrophysical Journal Letters. IX 2018. 865, 1. L3.

Rivkin Andrew S., Thomas Cristina A., Hammel Heidi B., Milam Stefanie N. Good Things in Small Packages: Asteroid Observations with JWST // American Astronomical Society Meeting Abstracts #230. 230. VI 2017. 403.01. (American Astronomical Society Meeting Abstracts).

Roger Eckardt. Stan Ulam, John Von Neumann, and the Monte Carlo Method // Los Alamos Science. 1987. 15. 131–136.

Russell C. T., Raymond C. A., Coradini A., McSween H. Y., Zuber M. T., Nathues A., De Sanctis M. C., Jaumann R., Konopliv A. S., Preusker F., Asmar S. W., Park R. S., Gaskell R., Keller H. U., Mottola S., Roatsch T., Scully J. E. C., Smith D. E., Tricarico P., Toplis M. J., Christensen U. R., Feldman W. C., Lawrence D. J., McCoy T. J., Prettyman T. H., Reedy R. C., Sykes M. E., Titus T. N. Dawn at Vesta: Testing the Protoplanetary Paradigm // Science. V 2012. 336, 6082. 684.

Scargle J. D. Studies in astronomical time series analysis. II. Statistical aspects of spectral analysis of unevenly spaced data. // The Astrophysical Journal. XII 1982. 263. 835–853.

Stalder B., Tonry J., Smartt S. J., Coughlin M., Chambers K. C., Stubbs C. W., Chen T. W., Kankare E., Smith K. W., Denneau L., Sherstyuk A., Heinze A., Weiland H., Rest A., Young D. R., Huber M. E., Flewelling H., Lowe T., Magnier E. A., Schultz A. S. B., Waters C., Wainscoat R., Willman M., Wright D. E., Chu J., Sanders D., Inserra C., Maguire K., Kotak R. Observations of the GRB Afterglow ATLAS17aeu and Its Possible Association with GW 170104 // The Astrophysical Journal. XII 2017. 850, 2. 149.

Stokes G. H., Evans J. B., Larson S. M. Near-Earth Asteroid Search Programs // Asteroids III. 2002. 45–54.

Stokes Grant H., Evans Jenifer B., Vigh Herbert E. M., Shelly Frank C., Pearce Eric C. Lincoln Near-Earth Asteroid Program (LINEAR) // Icarus. XI 2000. 148, 1. 21–28.

Stuart Joseph Scott, Binzel Richard P. Bias-corrected population, size distribution, and impact hazard for the near-Earth objects // Icarus. VIII 2004. 170, 2. 295–311.

The White House USA. Executive Order on Encouraging International Support for the Recovery and use of Space Resources. April 2020.

- Thirouin A., Moskovitz N., Binzel R. P., Christensen E., DeMeo F. E., Person M. J., Polishook D., Thomas C. A., Trilling D., Willman M., Hinkle M., Burt B., Avner D., Aceituno F. J.* The Mission Accessible Near-Earth Objects Survey (MANOS): First Photometric Results // *AJ.* XII 2016. 152, 6. 163.
- Thomas C. A., Trilling D. E., Emery J. P., Mueller M., Hora J. L., Benner L. A. M., Bhattacharya B., Bottke W. F., Chesley S., Delbó M., Fazio G., Harris A. W., Mainzer A., Mommert M., Morbidelli A., Penprase B., Smith H. A., Spahr T. B., Stansberry J. A.* ExploreNEOs. V. Average Albedo by Taxonomic Complex in the Near-Earth Asteroid Population // *AJ.* IX 2011. 142, 3. 85.
- Tonry J. L., Denneau L., Heinze A. N., Stalder B., Smith K. W., Smartt S. J., Stubbs C. W., Weiland H. J., Rest A.* ATLAS: A High-cadence All-sky Survey System // *Publications of the Astronomical Society of the Pacific.* VI 2018. 130, 988. 064505.
- Trilling D. E., Mueller M., Hora J. L., Harris A. W., Bhattacharya B., Bottke W. F., Chesley S., Delbo M., Emery J. P., Fazio G., Mainzer A., Penprase B., Smith H. A., Spahr T. B., Stansberry J. A., Thomas C. A.* ExploreNEOs. I. Description and First Results from the Warm Spitzer Near-Earth Object Survey // *AJ.* IX 2010a. 140, 3. 770–784.
- Trilling D. E., Mueller M., Hora J. L., Harris A. W., Bhattacharya B., Bottke W. F., Chesley S., Delbo M., Emery J. P., Fazio G., Mainzer A., Penprase B., Smith H. A., Spahr T. B., Stansberry J. A., Thomas C. A.* ExploreNEOs. I. Description and First Results from the Warm Spitzer Near-Earth Object Survey // *AJ.* IX 2010b. 140, 3. 770–784.
- Trilling D. E., Valdes F., Allen L., James D., Fuentes C., Herrera D., Axelrod T., Rajagopal J.* The Size Distribution of Near-Earth Objects Larger Than 10 m // *AJ.* X 2017. 154, 4. 170.
- Vokrouhlický D., Bottke W. F., Chesley S. R., Scheeres D. J., Statler T. S.* The Yarkovsky and YORP Effects // *Asteroids IV.* 2015. 509–531.

- Vokrouhlický David, Bottke William F., Nesvorný David.* Forming the Flora Family: Implications for the Near-Earth Asteroid Population and Large Terrestrial Planet Impactors // *AJ.* IV 2017. 153, 4. 172.
- Warner Brian D., Harris Alan W., Pravec Petr.* The asteroid lightcurve database // *Icarus.* VII 2009. 202, 1. 134–146.
- Watson Alan M., Richer Michael G., Bloom Joshua S., Butler Nathaniel R., Ceseña Urania, Clark David, Colorado Enrique, Córdoba Antolín., Farah Alejandro, Fox-Machado Lester, Fox Ori D., García Benjamín., Georgiev Leonid N., González J. Jesús, Guisa Gerardo, Gutiérrez Leonel, Herrera Joel, Klein Christopher R., Kuttyrev Alexander S., Lazo Francisco, Lee William H., López Eduardo, Luna Esteban, Martínez Benjamín., Murillo Francisco, Murillo José Manuel, Núñez Juan Manuel, Prochaska J. Xavier, Ochoa José Luís., Quirós Fernando, Rapchun David A., Román-Zúñiga Carlos, Valyavin Gennady.* Automation of the OAN/SPM 1.5-meter Johnson telescope for operations with RATIR // *Proc. SPIE.* 8444. IX 2012. 84445L. (Society of Photo-Optical Instrumentation Engineers (SPIE) Conference Series).
- Wetherill G. W.* Where do the meteorites come from? A re-evaluation of the earth-crossing apollo objects as sources of chondritic meteorites // *Geochimica et Cosmochimica Acta.* XI 1976. 40, 11. 1297–1317.
- Wood X. H. J., Kuiper G. P.* Photometric Studies of Asteroids. // *APJ.* V 1963. 137. 1279.
- Zappala Vincenzo, Cellino Alberto, Farinella Paolo, Knezevic Zoran.* Asteroid Families. I. Identification by Hierarchical Clustering and Reliability Assessment // *AJ.* XII 1990. 100. 2030.